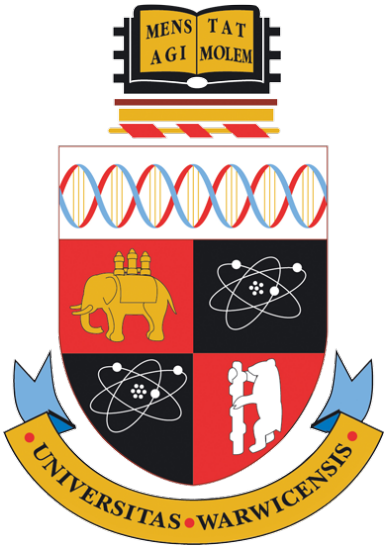

The application of proton computed tomography to reduce proton therapy range uncertainties

by

Samuel Paul Manger

Thesis

Submitted to the University of Warwick

for the degree of

Doctor of Philosophy

Department of Physics

August 2018

Contents

List of Tables

List of Figures

Acknowledgments

There are many people who I'd like to acknowledge for their support over the four years it took to complete my PhD. First and foremost, I'd like to thank my supervisors Dr Jon Duffy and Dr Spyros Manolopoulos for their help and guidance over an exciting and interesting project. I'd also like to thank The University of Warwick and University Hospitals Coventry and Warwickshire for funding my studies. Thanks should go to Pete Mulholland and Sarah Baker at UHCW, for assistance in manufacturing the film phantom, and supervision of my use of the x-ray CT scanner.

I'd like to thank the PRaVDA Collaboration for allowing me to be part of such a great project and sending me to South Africa to take part in the proton CT experiments. In particular, I'd like to thank Tony Price, Chris Waltham, Michela Esposito, Jon Taylor, Ben Phoenix and Gavin Poludniowski for your answers to my many questions, and Stuart Green, Phil Allport, Phil Evans, David Parker, Grainne Riley and Nigel Allinson for your added support and feedback. Our collaborators at iThemba LABS also provided great help and advice and were extremely welcoming, and I'd like to thank Jaime Nieto-Camero and Julyan Symons for hosting us and 96 Winery Road for providing the steaks.

Over my four years at Warwick, I've met some great people who were always willing to offer support. I'd like to thank Jane Rogers and Jenny Spiga for your help in medical physics, Olly Newell and Claire Thring for the lunchtime runs, and Mo Saghir, Marc Walker, Steph Glover, Dave Kersh, Chris Burrows and Jamie Bryant for the lunchtime chats.

Outside of work, I am hugely grateful to my parents for not changing the locks when I told them I was moving home, and my brother Alex. My friends from

Atherstone include Tom Millichamp, Katy Millichamp and Dan Francis who offered advice, a cup of tea or a beer whenever needed and supported both me and Rachel through the stressful times. I'd like to acknowledge Rachel's mum Anna Dixon, who always asked about my work and even when I couldn't visit would send some pasta over my way! I also need to thank my friends Tom Hodson, Kirsty Wayness, Rob Nichol, Georgia Kime and Alys Rudling for keeping me sane over the period of my PhD, and never letting me panic even as the deadline loomed. Over the course of 2017 and 2018, Tom and I cycled a lot and during the many hours of silence, I was able to do a lot of thinking that helped me get results!

I'd also like to thank both the England football team and Geraint Thomas for making 2018 a particularly great year for sport. It was much easier to stay at the computer writing this thesis knowing I could follow G's progress on the Tour de France, and that I could finish the day with a cold beer watching Gareth Southgate's team progress in Russia. Maybe next time, football will come home.

Finally, I'd like to thank my partner Rachel Dixon. Over the course of my PhD, she has been there for emotional, moral and financial support. At times when I thought I wasn't good enough to get this far, Rachel was always the one who convinced me I could do this. She made a lot of sacrifices for me to pursue this PhD and at no point asked for anything in return. She even read the whole thesis front to back with me after a marathon writing session, one of the most gruelling exercises of my life. I cannot thank her enough. This is for you.

Declarations

Some of the data presented in this thesis was obtained in an experiment carried out by the PRaVDA Collaboration at iThemba LABS, South Africa. I played a role in the prepration and execution of the experiment and the data analysis and intepretation included in this thesis is my own work.

Abstract

Proton therapy is a method of radiotherapy utilising protons to deliver a therapeutic dose of radiation to target cancer. Unlike x-rays, protons in the therapeutic energy range (< 250 MeV) have a finite range in the body. The physics of proton interactions mean that protons deposit most of their radiation dose at the end of their range. Hence, through careful selection of proton energy, protons have the potential to deliver dose to the target whilst sparing healthy surrounding tissue, as well as reducing the total dose given to the patient. This is particularly favourable for paediatric patients. However, the accuracy of proton therapy is currently limited by uncertainty in the delivered proton range. Because of this range uncertainty, a margin of typically 3.5 mm + 3% is added to the proton range. A major source of range uncertainty in proton therapy arises from the use of x-ray CT when imaging the patient for treatment planning. Here, an alternative imaging modality is tested in an effort to reduce range uncertainty.

A proposed solution to remove this source of uncertainty is the use of proton CT. In proton CT, the stopping power relative to water (RSP) of the patient is measured directly, potentially increasing the accuracy of imaging for proton therapy treatment planning. The PRaVDA prototype proton CT system is a proton-tracking CT system designed using fully solid-state technology to resolve the paths of individual protons entering and exiting a phantom, and then measure the residual range of the phantom. With this information, an image is constructed of proton stopping power.

In this thesis, the first results from the PRaVDA proton CT system are

shown. An image of a test phantom was acquired and the RSP accuracy of the image was shown to be better than 1.3% in materials replicating soft tissue and bone. The image contained artefacts arising from the raw data acquired and the source of these artefacts is investigated. Further study into the use of proton CT for proton range calculation was performed using a dosimetric phantom. The dosimetric phantom contains a section of EBT-3 radiochromic film capable of measuring a 2D dose distribution. The phantom was exposed to proton beams at two different energies, and images of the phantom were acquired using proton CT and x-ray CT. The proton CT and x-ray CT images were used to calculate the expected proton range using a validated Monte Carlo simulation, and the simulated results were compared against the experimental measurement.

Chapter 1

Introduction

Proton therapy uses protons to deliver a therapeutic dose of ionising radiation to damage cancer cells. First proposed by Robert Wilson in 1946 [1], protons in the therapeutic energy range (50-250 MeV) have a finite range in tissue and deposit dose as they lose energy. Protons, amongst other heavy ions, may be considered advantageous to x-rays in radiation therapy due to their highly selective dose deposition, as they deliver most of their radiation dose at the end of their range. Through careful selection and modulation of the beam energy, the proton range can be adjusted to target the cancer with a radiation dose whilst sparing surrounding healthy tissue and anything beyond the range of the beam. However, uncertainty in the range of the delivered proton beam leads to an uncertainty in the position of the delivered dose. Consequently, proton treatment plans are designed with large margins reducing the ability to use proton therapy to its full potential.

A major contributor to the proton range uncertainty arises from the use of x-ray CT imaging, used to plan proton therapy treatments. A 3D image of the subject is produced based on x-ray attenuation and is used to inform, amongst other things, the required range and therefore the energy of the therapeutic proton beam. To use the data for treatment planning, the images must be converted from x-ray attenuation to proton stopping powers. Whilst x-ray attenuation is mostly dependent on electron density, proton stopping powers are also dependent on the mean excitation energy, or I-value, which roughly scales with the atomic number, or Z-number, of the material. This causes a degeneracy in the conversion of x-ray attenuation to proton stopping powers. The degeneracy is accounted for by adding uncertainty to the converted stopping power values which in turn results in an uncertainty in the delivered proton range [2]. A proposed solution is to image the patient using protons, directly measuring the proton stopping power of the patient.

This is known as proton computed tomography (proton CT).

This thesis will cover work done to aid the calibration and evaluation of a novel prototype proton CT system constructed by the PRaVDA Collaboration.

1.1 Radiation Therapy

Radiation therapy, or radiotherapy, is a method of cancer treatment that uses ionising radiation to damage or kill tumour cells. Around 40% of patients with cancer receive radiotherapy as part of their treatment [3].

The most common method of radiotherapy uses x-rays typically with energies between 1-20 MeV, generated by accelerating electrons in a linear accelerator on a gantry and colliding them with a target. The treatment is prescribed in terms of a radiation dose to the target volume, measured in units of Gray (Gy), where 1 Gy is 1 Joule of energy absorbed by 1 kilogram of mass.

$$1 \text{ Gy} = \frac{1 \text{ J}}{1 \text{ kg}} \tag{1.1}$$

Typical radiotherapy treatments aim to deliver a dose of around 50 - 70 Gy to the target volume, fractionated such that the total dose is delivered daily over a period of several weeks [4]. Therefore, it is important to ensure that the dose delivery is both highly localised and adaptable to daily change, as well as ensuring that dose to critical organs in the body, that may result in significant impairment or even death, is kept to a minimum. In order to achieve this in x-ray radiotherapy, multiple x-ray fields are delivered to the patient using a gantry to deliver dose from different angles, such that the radiation dose superposes at the target site and the necessary entry and exit dose is spread around the body, minimising its effect.

An alternative method of radiotherapy is ion therapy. In ion therapy, charged particles such as protons, helium ions and carbon ions are accelerated to energies of up to 300 MeV/u in order to deliver a localised dose [5]. Unlike highly penetrating x-ray beams, these ions lose all of their energy in the patient and come to a stop meaning that there is no exit dose. Even more critically, the energy loss mechanisms of these ions mean that they lose the majority of their energy at the point at which they stop. Therefore, with careful energy selection, it would seem that ion therapy could be favourable for radiotherapy in terms of minimising the dose delivered to healthy tissue. For this reason, the NHS has recently invested in two high-energy proton therapy centres at The Christie Hospital in Manchester and University College London Hospital in order to provide a specialist service to treat patients who would see the most benefit from proton therapy. The first patient is expected to be

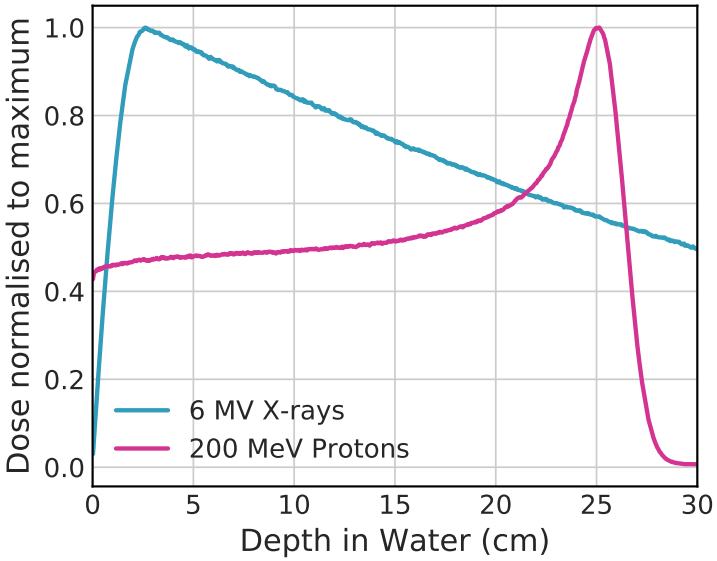

Figure 1.1: Depth-Dose curves for x-rays and protons

treated in 2018.

1.2 Depth-Dose curves

Depth-dose curves show how the radiation dose delivered by radiotherapy varies over the depth of the patient. Typically, depth-dose curves are shown in water as water is a useful proxy for tissue. Figure 1.1 compares depth-dose curves for x-rays and protons.

X-ray radiation absorption is described by linear attenuation meaning there is a high radiation dose at low depth that reduces exponentially. Therefore, a lot of healthy tissue may receive a radiation dose. The initial rise in dose over the first cm of the depth-dose curve is due to Compton scattering, where excited electrons are forward scattered in the direction of the beam and therefore deposit their dose further ahead.

For protons, the depth-dose curve is significantly different. A low entrance dose can be seen, with a sharp rise to a peak and a fall off to zero. This peak is the Bragg peak, and the aim of ion therapy is to use this peak to treat the tumour. Other ions (helium, carbon) have very similar depth-dose curves to protons and generally have narrower Bragg peaks, however due to their lower mass, protons are easier to accelerate and there is significantly more clinical use of proton therapy worldwide [6]. This thesis will focus on proton therapy and specifically proton CT

from this point forward. The dose absorbed in proton therapy is a function of the fluence of the beam, the stopping power of the absorbing material and the mass density of the material:

$$D = \Phi \frac{S}{\rho} = \Phi \frac{1}{\rho} \frac{dE}{dx} \tag{1.2}$$

where Φ is the fluence of the beam in terms of the number of protons, ρ is the mass density of the absorber and S is the stopping power of the material; a measure of the energy absorbed over a unit length [7].

1.3 Bragg Peak

As shown in the depth-dose curves, the Bragg peak is the main advantage in proton therapy. The Bragg peak arises due to the nature of proton interactions with matter. The position of the Bragg peak is dependent on the energy of the primary proton beam and the stopping power of the medium. The initial energy of the proton beam used in the clinic is often defined by the beam's range in water. The range of the beam is defined as the point at which the Bragg peak falls to 80% of its maximum dose on its distal edge, which can be referred to as R_{80}. This is chosen as it is approximately the point at which 50% of the protons in the primary beam will have stopped [7]. The range-energy relationship can then be defined by a power law

$$R_{80}[cm] = aE^b \tag{1.3}$$

where a is a material-dependent constant and b is a fitting parameter. A fit of the proton range in water for energies between 100 MeV and 200 MeV yields values of 0.00244 and 1.75 for a and b respectively [7], where the proton range in water was determined from a look-up table published in ICRU report 49 [8].

To demonstrate this, Bragg peaks from proton beams are shown in figure 1.2. The proton beam with the shortest range is a Monte Carlo simulation of the MC40 cyclotron at the University of Birmingham that provides a 31 MeV beam with an 11 mm range in water. This proton beam was used during the commissioning and testing of the proton CT system described in this thesis, however the range of the proton beam is insufficient for proton therapy treatments. The second beam shown is a 60 MeV proton beam corresponding to the maximum energy output of the Douglas cyclotron at the Clatterbridge Cancer Centre, Wirral, UK. Clatterbridge became the world's first hospital-based proton therapy centre in 1989. This proton beam has a 31 mm range in water and is used to treat ocular tumours. The final

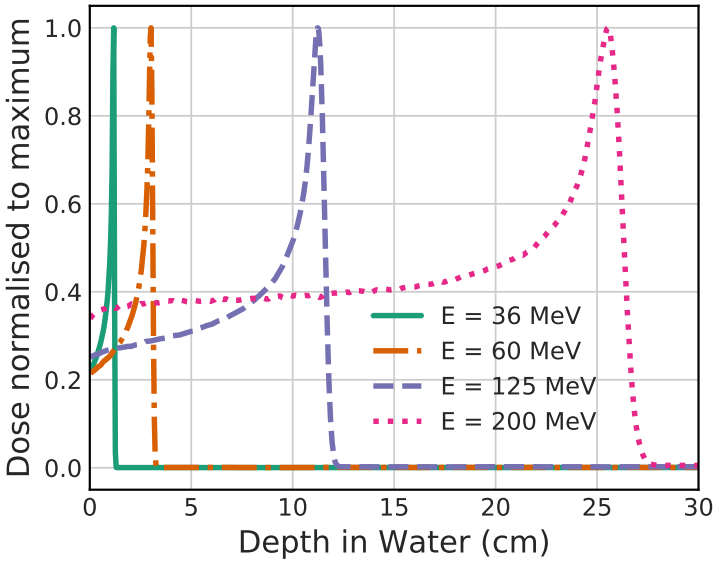

Figure 1.2: Depth-Dose curves of proton beams with different initial energies. The 36 MeV is representative of the range of the proton beam from the MC40 cyclotron at the University of Birmingham. The 60 MeV beam is representative of the beam from the Douglas Cyclotron at Clatterbridge Cancer Centre, Wirral, used to treat ocular tumours. The 125 MeV and 200 MeV proton beams are representative of a clinical proton beam with enough range to deliver a proton therapy treatment.

two Bragg peaks are simulations of a high energy beam suitable for proton therapy. The 125 MeV beam has a range of approximately 118 mm range in water, and the 200 MeV beam a range of approximately 26 cm range in water. The maximum energy output of proton accelerators designed for proton therapy is typically between 200 - 250 MeV, more than sufficient to provide adequate range for proton therapy treatments [9].

Using the Bragg peak in radiotherapy has a distinct advantage over x-ray radiotherapy in cases where the tumour is close to critical structures, or in young patients where the accumulation of dose to healthy tissue may cause growth defects, affect cognitive development or lead to secondary cancers later in life [10]. An example of how proton therapy may be advantageous to x-ray radiotherapy is shown in figure 1.3. The figure shows the dose distribution from two radiotherapy treatment plans, one using x-rays and one using protons. The proton therapy treatment plan spares the gastrointestinal system, chest and the heart from radiation dose. The figure highlights the potential of proton therapy.

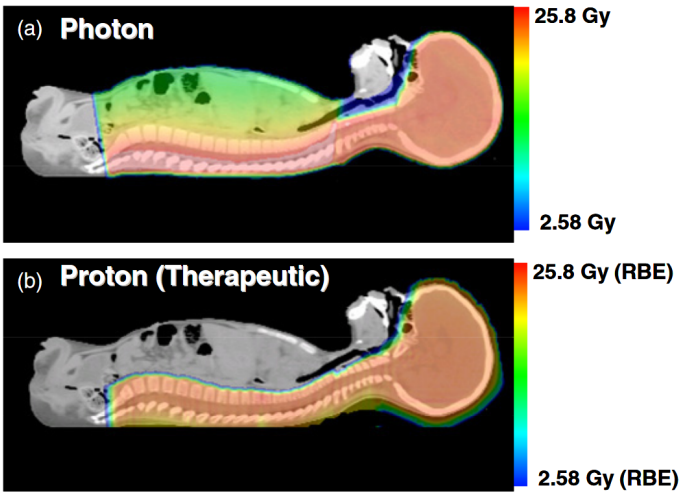

Figure 1.3: Treatment plans showing craniospinal irradiation of a paediatric patient to treat medulloblastoma. Image a) shows the distribution of dose from a non-optimized x-ray radiotherapy treatment. Image b) shows the dose distribution from a proton therapy treatment. Image reproduced with permission from [10].

1.4 Stopping Power

The stopping power S of a material describes the rate of energy loss by the incident particle over a unit length:

$$S(E) = -\frac{dE}{dx}. \tag{1.4}$$

The stopping power at any given point is dependent on the instantaneous energy of the incident particle as well as the atomic number and mean excitation energy, or I-value, of the material. The Bethe-Bloch equation [7, 8] defines the stopping power of a material for ions in the therapeutic energy range and is given as:

$$\frac{S}{\rho} = -\frac{1}{\rho}\frac{dE}{dx} = \frac{4\pi r_e^2 m_e c^2}{\beta^2}\frac{1}{u}\frac{Z}{A}z^2\left[\ln\left(\frac{2m_e c^2\beta^2}{1-\beta^2}\right) - \ln I_m - \beta^2\right] \tag{1.5}$$

where r_e^2 is the classical electron radius, m_e is the electron mass, u is the atomic mass unit, β is the velocity of the proton divided by the c, Z and A are the atomic number and relative atomic mass of the absorber material, z is the charge of the projectile and I_m is the mean excitation energy, or I-value, of the material, given in eV. The constants $4\pi r_e^2 mc^2/u$ have an approximate value of 0.307MeV cm^{2}g^{-2}.

Some publications include a more thorough version of the Bethe-Bloch equation including the shell correction and density corrections however these are not relevant for therapeutic proton therapy [8, 11]. The Bethe-Bloch formula aids in understanding the shape of the Bragg peak. As the proton loses velocity, the rate of energy loss increases, giving rise to the peak until the proton comes to a stop. Integrating the Bethe-Bloch formula provides the proton range.

In proton therapy, the Bethe-Bloch formula is used to calculate stopping powers for human tissues in order to define a conversion curve or look-up table to estimate stopping powers based on x-ray attenuation. For this purpose it is much simpler to consider the stopping power of the material relative to water, called the relative stopping power (RSP). The advantage of using the RSP term is that provided that the material has a Z-number close to water, the relative stopping power remains relatively constant with proton energy. Many of the constants in equation 1.5 also drop out of the equation and we are left with

$$RSP_m = \rho_{e,rel} \frac{\left(\ln \frac{2m_e c^2 \beta^2}{(1-\beta^2)I_m} - \beta^2\right)}{\left(\ln \frac{2m_e c^2 \beta^2}{(1-\beta^2)I_w} - \beta^2\right)}, \tag{1.6}$$

where $\rho_{e,rel}$ is the electron density of the material relative to water, I_w is the I-value of water and all other terms are previously defined. This formula was first defined by Schneider et al [12]. With this formula, the RSP of a material can be calculated from the electron density and the mean ionisation potential.

The I-value of the medium is an average of the excitation energies of a medium, weighted by their respective dipole oscillator strengths [13]. A first order approximation is that $I \approx Z \times 10$ eV [8, 14] however the exact I-value of a material is difficult to calculate accurately from first principles. For this reason, experimental measurements of I-values for elemental media and a selection of compounds are compiled and published in ICRU Report 49. The I-value for material m from elemental values can be calculated using the Bragg additivity rule:

$$\ln I_m = \left(\sum_i \frac{\omega_i Z_i}{A_i} \ln I_i\right)\left(\sum_i \frac{\omega_i Z_i}{A_i}\right)^{-1} \tag{1.7}$$

However, the complex nature of bonding in mixtures and compounds means that Bragg additivity is inexact and leads to uncertainties when calculating the I-value of materials, typically leading to an uncertainty of 1.5% when calculating proton ranges [15]. Therefore, a common method for obtaining I-values is to fit the Bethe-Bloch formula to measured stopping powers, usually through measurements of proton range. In this way, the I-value is treated as a free parameter that can be

adjusted to fit a model [11]. Recent work has sought to reduce the uncertainty in I-values by recalculating all of the elemental I-values such that they are optimised for use with the Bragg additivity rule [16].

1.5 Multiple Coulomb Scattering

Protons undergo many small deviations from their straight line path due to electromagnetic reactions with atomic nuclei. These small deviations are known as multiple Coulomb scattering (MCS). Individual scattering events are almost always negligible however the sum of many of the scatters in the beam leads to an almost-Gaussian distribution of proton trajectories. The non-Gaussian elements are due to large single scatters however these are considered negligible in proton radiotherapy, and only count for around 2% of the primary proton beam [7].

Whilst a full description of scattering is covered by Molière theory, a Gaussian approximation of the scattering angle given particle energy and material thickness is much simpler to compute. This approximation is described by Highland's formula:

$$\theta_0 = \left(1 + \frac{1}{9}\log_{10}\frac{x}{X_0}\right)\left(\int_0^x \left(\frac{14.1\text{MeV}}{pv(x')}\right)^2 \frac{1}{X_0}dx'\right)^{1/2} \text{rad} \tag{1.8}$$

where X_0 is the radiation length of the absorber material and pv is the particle momentum multiplied by velocity [17]. θ_0 is the projected angle of scatter. The Gaussian approximation can be used to aid the design of scattering filters for proton therapy [18].

Scatter is a particularly important consideration in proton CT as the image reconstruction must take into consideration energy losses along non-linear paths. A number of approaches have been devised to account for scatter by considering the most-likely path that a proton will take through an object. This can be achieved provided that accurate positional information is known about each proton used for imaging [19, 20, 21]. The presence of multiple Coulomb scattering places a fundamental limit on the spatial resolution achievable by proton CT [22]. We obtain from equation 1.8 that the scattering angle is dependent on the kinetic energy of the proton, therefore we can expect less scatter with a higher energy proton beam. With this knowledge, it is possible to define the scattering power of a material:

$$T(x) = \frac{d\langle\theta_y^2\rangle}{dx}. \tag{1.9}$$

Provided solely with positional information of each individual proton, it is therefore possible to perform tomographic reconstructions of scattering power [23],

as demonstrated by the PRaVDA Collaboration [24]. Whilst there is currently limited use for this information, it is feasible that scattering power data may be incorporated into Monte Carlo dose calculation for treatment planning, as knowledge of scattering power reduces uncertainties in the lateral spread of a proton beam. However, in this thesis we only are concerned with relative stopping power reconstructions.

1.6 Nuclear Reactions

In addition to the inelastic reactions with atomic electrons and the nucleus, there is a non-negligible chance of the incident proton undergoing a nonelastic nuclear reaction with the atomic nucleus of the absorber material. In a 160 MeV beam, typically around 20% of the primary protons will undergo a nuclear reaction with the medium. In order to undergo a nuclear reaction, the incident proton must have enough energy to overcome the Coulomb barrier of the nucleus which is around 8 MeV for materials relevant to proton therapy [25]. Nuclear reactions in proton therapy produce energetic secondary protons, deuterons, neutrons, gammas, alpha particles and other ions [7]. For proton CT, the detector systems must be constructed to be robust from radiation damage from nuclear reactions, known as non-ionising energy loss, that can cause displacement damage to the crystal lattice in semiconductor detectors. Some products of nuclear reactions may be used during proton therapy treatment to monitor the proton range in real-time [26]. For example, prompt-gamma imaging and positron emission tomography can be employed during treatment to resolve the source of the emission of secondaries and thus determine the position of the Bragg peak.

1.7 Summary

Proton therapy provides potential advantages in clinical use compared to conventional x-ray radiotherapy. Not only can critical organs be shielded from dose, but the patient will receive a lower integral dose to the body. This is particularly important for young people, where the risks of developing secondary cancers or experiencing growth defects or cognitive impairment due to the stray radiation dose are much higher. However, the full benefit of proton therapy may not be realised until the margins used for treatment planning can be reduced. A major contributor to proton range uncertainty, used to define the margins, arises from the conversion of x-ray CT Hounsfield Units (HU) to proton stopping powers. A proposed solution to re-

duce this uncertainty is the use of proton tomographic imaging. This thesis will discuss a method of performing proton CT and demonstrate its use, culminating in a comparison of Monte Carlo dose calculations performed on x-ray CT and proton CT data against a measurement taken in a dosimetric phantom.

Chapter 2

Proton Computed Tomography

Proton computed tomography (proton CT) is a method of tomographic imaging using protons. The motivation behind using protons for imaging arises from the desire to improve the accuracy of imaging for proton therapy in terms of accurate stopping power data. By using the proton treatment beam to image the patient, the contrast mechanism is proton stopping power, removing the need for an indirect conversion from x-ray attenuation currently used when planning proton therapy treatments [27].

Although the concept of proton CT has been around for as long as x-ray CT [28], there are no proton CT system in use clinically despite a number of research proton CT systems having been developed [29, 22]. The first experimental demonstrations of proton CT began in the 1970s. However, the spatial resolution of these systems suffered as multiple Coulomb scattering (MCS) was not accounted for [30]. There was an early acceptance that whilst there were benefits to proton CT, the technology and computing resources to perform a proton CT scan with sufficient spatial resolution in a clinical time frame were not yet available [31]. In recent years the growth in proton therapy has renewed interest in proton CT and a number of research groups are actively developing proton CT systems. Whilst the choice of specific instrumentation may vary between these systems, they all aim to reconstruct proton CT images by tracking individual protons and measuring their residual energy. Two recent reviews of the state of proton CT are [22] and [29].

2.1 Review

2.1.1 Motivation

The modern motivation for proton computed tomography is to reduce range uncertainty in proton therapy. Range uncertainty refers to the uncertainty in the range of the delivered beam used in proton therapy. Due to the steep dose gradient at the Bragg peak, proton therapy is highly sensitive to range uncertainties. Typically, a margin of the order of 3 - 3.5% is added to the expected proton range to account for this uncertainty. Because of this margin, the effectiveness of proton therapy is then reduced and the potential for more advanced treatments, where the distal edge of the Bragg peak may be used to spare a critical structure, is hindered [26].

Sources of range uncertainty include range straggling, where due to MCS each individual proton takes a different path thus 'smearing' the end of the proton beam range, patient set-up uncertainty, allowing for a tolerance in the position of the patient, and variation in the beam energy. Range straggling typically contributes an uncertainty of 1-2% of the beam range [26, 15] however this is likely to be reduced with the introduction of Monte Carlo treatment planning. Range uncertainty due to variation of the beam energy and patient set-up is much more random in nature and not necessarily dependent on the initial range of the beam. To account for these random uncertainties, an additional margin of the order of 1.2 mm is added to the beam range. Nevertheless, the use of proton CT equipment prior to treatment may have advantages in verifying the energy/range of the beam and also the patient position.

A major contributor to range uncertainty arises from the imaging modality currently used for treatment planning: x-ray CT [15, 2]. The significance of x-ray CT is an uncertainty of up to 3% [32]. Yang et al [2]provided a comprehensive study of range uncertainty associated with the use of x-ray CT for proton therapy treatment planning, and the stoichiometric conversion method used to convert x-ray absorption to proton stopping powers. The method entails a number of steps each with their own uncertainties. For soft tissue, where the sum of the uncertainties in quadrature is 1.6%, the individual sources are

- Uncertainties in parameterized stoichiometric formula to calculate CT numbers - 0.8%
- Uncertainties due to deviation of human tissue from ICRU standard tissue - 1.2%
- Uncertainties in mean excitation energies - 0.2 %

- Other sources - 0.6 %

The use of proton CT imaging would remove the first three steps of this process [22], and while there may be additional uncertainties associated with proton CT is should be feasible to reduce the total uncertainty - in bone, soft tissue and in lungs - to 1% or better [33, 29]. For a beam with nominally 10 cm range in water, this represents reducing the margins from ±3mm to ±1mm.

2.1.2 History

The first proton radiograph was performed in 1968 by Koehler, using a 137 MeV proton beam at the Harvard cyclotron [34]. A lead scatterer was placed in the beam to produce a beam with a radius of 10 cm, and a number of aluminium absorber sheets were placed in the beam path. A piece of photographic film was placed behind the absorber sheets with the resulting image demonstrating potential for protons to be used for imaging objects with high contrast, despite the poor spatial resolution. Koehler published further work in 1976 with Cormack performing the first quantitative proton CT experiments [30]. Two scintillating counters were used, one recording signal behind a known thickness of lucite and another recording the signal behind a phantom that was scanned across the counter. By comparing the relative counts, the density of the phantom could be reconstructed.

Whilst Koehler continued further work into proton radiography, other groups began to realise the potential of proton CT to offer better contrast in soft tissue than x-ray CT imaging, as well as the opportunity to significantly reduce the radiation dose to a patient given during imaging. Hanson proposed that proton CT may reduce the necessary imaging dose by up to 90% when compared to x-ray CT, and also that recording individual proton histories may improve the spatial resolution of the system. An event rate of 10^8 protons per second was deemed necessary to achieve the required timescales for clinical imaging [35]. Around the same time, Kramer et al demonstrated a system at a synchrotron facility in Argonne with a 205 MeV proton beam [36]. Using scintillator counters upstream and downstream of the image object, a density phantom and a number of human samples were imaged. The authors also noted that blurring due to MCS could be reduced if the positional information could be used in reconstruction.

Hanson et al demonstrated experimental proton CT images taken at the Los Alamos Meson Physics Facility (LAMPF) in 1982 showing images of test phantoms and human specimens produced by measuring the exit positions of individual protons with a multiwire proportional chamber and a range telescope comprising 32

scintillator plates [37]. The experimental setup devised by Hanson et al with separate tracking and range detectors is relevant today as many modern systems are based on this concept [22]. The beam was magnetically scanned with energies of the order of around 230 MeV, however the scan time was still around 10 hours. Despite the additional positional information, the reconstruction assumed that straight line paths were taken by the protons.

A small number of further proton CT systems were developed in the intermediate time however not until the 1990s was a system developed solely focused on the aim of reducing uncertainty in proton stopping power, fueled by the growth in interest in proton therapy. Publications from the Paul Scherrer Institute (PSI) are therefore considered to be the starting point of modern proton imaging [22].

2.1.3 Methodology

The general method of modern day proton CT is to track the position of individual protons entering and exiting the patient and then measure their residual proton energy after exiting the patient. Provided with knowledge of the initial beam energy, the energy loss through the patient can be determined. Non-linear reconstructions accounting for the most-likely-path that the proton took through the patient allow for backprojection accounting for MCS [19, 38]. Each proton can then be considered as a ray projection analogous to x-ray CT and a tomographic reconstruction is performed.

A schematic of an ideal proton CT system is shown in figure 2.1. In order to track each proton and determine its path through the patient, position sensitive detectors (PSDs) are located before and after the patient. Using a pair of PSDs allows the trajectory of the proton to be determined rather than just the position. The residual energy of the proton upon exiting the final tracker is determined by a residual energy-range detector (RERD). This may take the form of a calorimeter, used to determine proton energy or a range telescope that directly measures the proton range.

2.1.4 Design Constraints

In order to improve on x-ray CT for proton therapy, a specific aim for proton CT development is to develop a device capable of reconstructing RSPs with an accuracy of 1%, yielding a proton range error of less than 1 mm for a beam with a nominal range of 100 mm [29]. The RSP is reconstructed from measurements of the water-equivalent path length (WEPL) of protons that have propagated through

the imaging subject. In research proton CT systems, in the absence of a patient, phantoms are used as imaging subjects. The WEPL is a line integral of RSP of the phantom that the proton has propagated. Measurements of the WEPL that protons have taken are backprojected to obtain RSPs. The WEPL is closely related to the water equivalent thickness (WET) of a material, however the WET is a property of the material and the WEPL is a property of the individual proton.

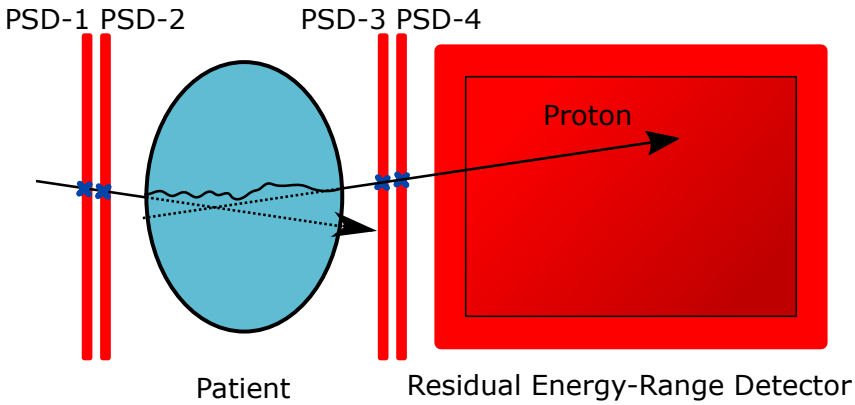

Figure 2.1: A schematic of an ideal proton CT system, redrawn from [22]. In this figure, the residual range-energy detector is a detector capable of measuring either the residual energy or range of the proton beam.

The design constraints in proton CT are set so that any uncertainty or ambiguity in measurement of the proton path or residual energy is minimal compared to the statistical variations between protons [22]. These statistical variations arise from the stochastic nature of proton interactions. Variations occur in the lateral position of the beam at a given depth in the patient (lateral straggling), proton direction at a given depth (angular straggling), energy at a given depth (energy straggling) and the final proton range for a given initial proton energy (range straggling). A combination of lateral straggling and angular straggling leads to a positional uncertainty in the patient of the order of 1 mm when reconstructing proton paths. The statistical variation in final proton range will be dependent on the initial energy spread of the beam however can be considered to be around 1% of the proton range. For a beam with a nominal energy of 200 MeV and an initial range of 260 mm in water the range straggling will be around 3 mm. The magnitudes of both of these uncertainties are likely to vary depending on the quality of the initial proton beam as well as the specific patient geometry however these values provide an idea of the limitations of proton CT.

There are further considerations when designing a proton CT system for clinical use. Keeping the imaging time short reduces the total dose given to the patient

as well as ensuring that use of the system can be realistically implemented into a clinical workflow. This requires a system to be efficient in proton detection. Detectors can be tuned to work optimally with knowledge of the specific time structure of the proton beam, however this varies between accelerator modalities due to the different methods of accelerating protons. Secondly, the size of the imaging field of view must be considered. This is currently limited by the range of the proton beam. Most proton therapy centers operate with a maximum beam energy of 200 - 250 MeV delivering between 26 - 38 cm range in water. Whilst this range may be sufficient to image paediatric patients and the skull, the range is not high enough to image areas such as an adult torso. Both of these design challenges would benefit from consideration by accelerator physicists with interest in developing proton CT.

2.1.5 Current proton imaging systems

A small number of collaborations have been formed since the early 2000s to develop proton CT systems and work on the associated challenges such as fast data acquisition and non-linear image reconstruction. The most significant of these groups include the collaboration between Loma Linda University and the University of California Santa Cruz (LLU/UCSC) with California State University, Baylor University, Northern Illinois University and the University of Wollongong each making contributions and the Italian PRIMA Collaboration.

The first proton imaging system in the modern era, used to reduce stopping power uncertainties was a proton radiography system capable of taking planar images at the Paul Scherrer Institue (PSI) in Switzerland. The system contains 2 tracking detectors either side of the image subject comprising scintillating fibres and a plastic scintillator range telescope. The active area of the imaging device was 22.0 x 3.2 cm^2. The system was used to optimise the HU to RSP conversion curve by comparing the calculated WET through an animal patient with measured WET from the radiography system for each proton path. By optimising the conversion curve, the mean WET deviation was reduced from 3.6 mm to 0.4 mm, suggesting that the modality could reduce a significant systematic error in the delivered proton range if used at the treatment planning stage [39, 40].

The LLU/UCSC collaboration began work in 2005 with an initial study into the electron density, and consequently stopping power, resolution of a potential proton CT system [33]. These studies showed that an accuracy of greater than 1% should be possible for proton CT. The collaboration went on to build two proton CT prototypes, namely the Phase II and Phase II instruments [29]. These proton CT systems were constructed based on silicon strip detector (SSD) technology for

individual proton tracking with scintillators providing the measurement of the residual energy of the beam. The tracking system of the Phase I system used two planes of SSDs in an x-y orientation. Each SSD was 400 µm thick with a pitch of 228 µm. The detectors were tiled to increase the field of view, however the x and y planes were offset from each other to reduce the effect of the "dead zone" around the edge of the sensor [41]. The energy measurement was performed by a calorimeter containing CsI:Tl crystals readout by photodiodes. The system was slow, with a scan time of several hours however did implement reconstructions taking advantage of the proton most-likely paths. Artefacts arose in the produced images due to the gaps between the SSDs, and the authors saw room for development in the calorimeter in the Phase II system [42].

The Phase II system operates between 10-100 times faster than the Phase I system and would be capable of imaging a human lead in less than 10 minutes [42]. The field of view of the system extends to approximately 8.8 cm x 35.0 cm where an object can be scanned through the system. The SSDs were improved by sawing the edges to minimise the "dead space" surrounding the detector such that they could be tiled more effectively. The calorimeter was redesigned to become a novel segmented energy-range detector, where 5 individual stages of a polystyrene-based scintillator, each measuring 5.1 cm in depth, were individually read out by photomultiplier tubes. Segmenting the scintillator reduced the dynamic range required on the readout electronics to determine the residual energy of each proton with the polystyrene material operating significantly faster than the CsI:Tl crystals used in the Phase I scanner. The system was used to image a number of test phantoms as well as a paediatric head phantom [43, 44], with reported results claiming to achieve WEPL resolution close to the theoretical limit of 2.8 mm and RSP accuracy of better than 3% for most materials with many better than 1%.

The PRIMA collaboration demonstrated a prototype system with a field of view of 5.0 x 5.0 cm^2, comprising SSDs to track protons and a YAG:Ce scintillator-based calorimeter to perform measurements of the residual proton energy. The YAG:Ce scintillator features a significantly shorter decay time than the CSI:Tl scintillator of the LLU/UCSC Phase I scanner and the SSD thickness was much lower than the LLU/UCSC design (200 µm), potentially reducing scattering caused by the detectors therefore improving the spatial resolution of the system [45]. Images of a 2 cm diameter plastic phantom have been published with an electron density resolution of 2.4% and a proposed PRIMA II scanner will increase the field-of-view of the system and feature a redesigned DAQ with an event rate exceeding 1 MHz.

Another Italian group, AQUA, performed proton radiography of a small

animal in 2013 [46]. The system used gas electron multiplier chambers as position sensitive detectors, with a stack of 48 polyvinyl-toluene plastic scintillators each read out by silicon photomultipliers providing the measurement of the residual range. The system only tracks protons as they exit the image subject, therefore the system can only assume linear proton paths through the image subject however this is sufficient for radiography. The active area of the detector is quite large at 30 x 30 cm^2. The rate capability of the system is also competitive at 1 MHz.

Other notable efforts include the collaboration between Northern Illinois University and Fermilab (NIU/FNAL), who constructed a system comprising scintillating fibres as trackers, and a scintillating range counter to determine the residual proton range [47]. Despite intending to use the system with a 200 MeV clinical beam, issues with the instrumentation and funding expiration unfortunately meant that the system wasn't tested [29].

Most recently, a group comprising the University of Bergen, Bergen University College, Haukeland University Hospital and Utrecht University are planning to develop a new proton CT system using CMOS monolithic active pixel sensors (MAPS) [48]. The group have published results testing a calorimeter that is based on the use of MAPS detectors, providing the opportunity to track multiple protons in each frame whilst measuring their residual range. A new prototype system is planned.

2.2 The PRaVDA Proton CT

The PRaVDA collaboration began in 2013, with the aim of designing and building a completely solid-state proton CT system. The PRaVDA system comprises 4 position sensitive detectors and a proton range detector, called the range telescope. The system was designed to be used with the proton beam at the iThemba Laboratory for Accelerator-Based Sciences (LABS), South Africa, a proton beam with a maximum range of approximately 240 mm in water. The beam is produced by a cyclotron. The beamline uses passive scattering to flatten the beam and generate a maximum beam size with a diameter of 10 cm. For the PRaVDA proton CT work, a beam energy of 125 MeV delivering nominally 118 mm range in water was used. A photograph of the PRaVDA proton CT system in place at iThemab LABS is shown in figure 2.2.

The PRaVDA system is novel in its application of silicon strip detectors (SSDs) to measure the residual proton range. The system is based on fully solid-state technology and also uses a novel reconstruction algorithm to reconstruct RSPs from list-mode data provided by the detector system. A motivation for using solid-state

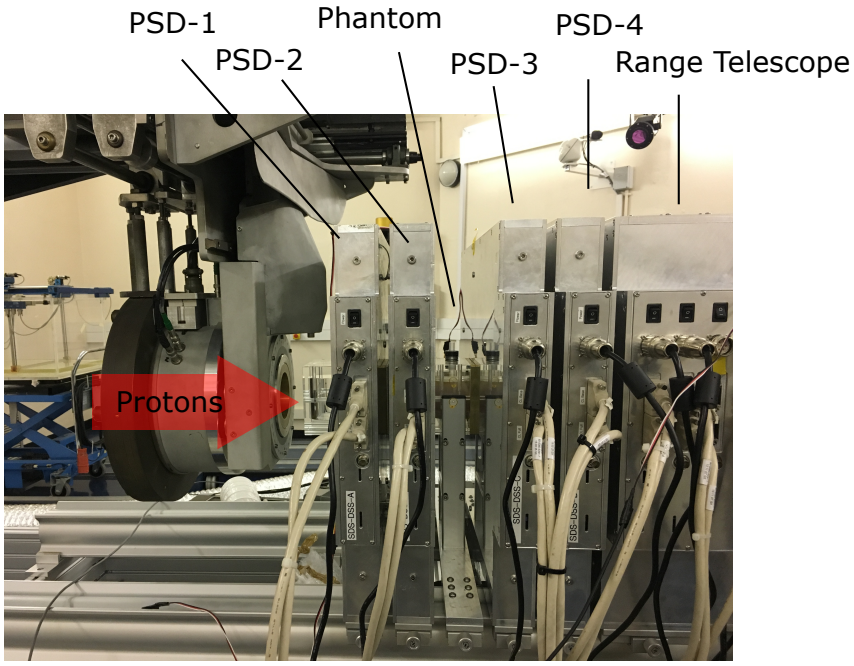

Figure 2.2: Photograph of the PRaVDA proton CT system at iThemba LABS.

technology is the capability of the detector systems to resolve multiple individual proton hits at a fast rate. One approach in proton CT is to use a scintillator-based range-energy detector, however the method is rate-limited due to scintillator relaxation time and issues with pulse shaping in the presence of multiple hits [42].

2.2.1 Tracker Units

The use of SSDs for application in PSDs is relatively commonplace amongst proton CT instrumentation [22]. The devices are popular due to their excellent efficiency, fast readout rate and low noise characteristics, whilst being radiation hard. SSDs are one-dimensional detectors, therefore typically two perpendicular planes of detector are used to obtain 2D positional information. The PRaVDA approach is novel in proton CT in that the PRaVDA PSDs use three planes of 1D SSDs in each PSD, also called the tracker units. The three detector planes are oriented at 60° to each other known as x-u-v orientation and create an effective pixel. This arrangement reduces ambiguities when reconstructing multiple protons hits in a single frame. The ambiguity rate in the case of 30 hits per frame is around 8% when using x-u-v orientation, compared to 100% in a 2 layer x-y orientation [49].

The strips in the PRaVDA SSDs are 4.8 cm long with a pitch of 90.8 µm, providing an active area of 93 x 96 mm^2 [50]. Each detector layer is 150 µm thick.

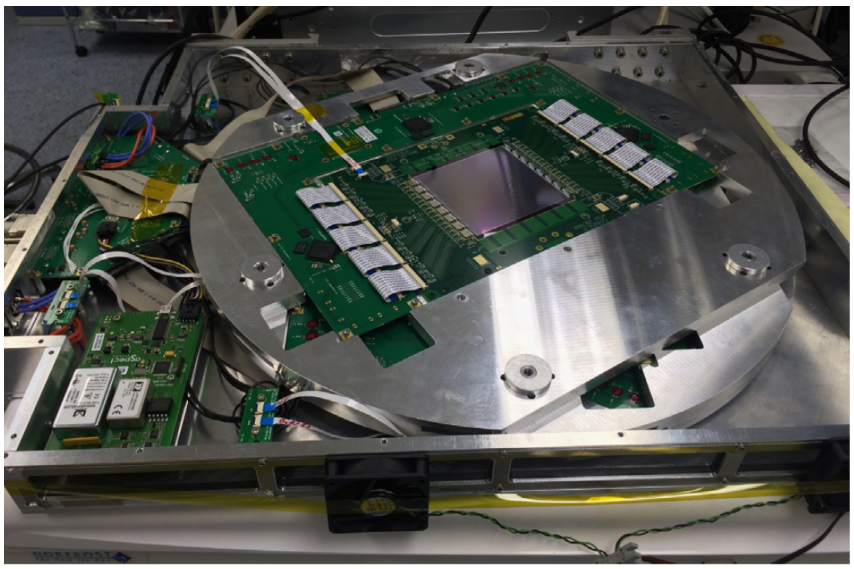

Figure 2.3: Photograph of a PRaVDA tracker unit with the top cover removed. The three planes of detector are attached to aluminium stiffeners and held in place with locating posts. The top layer of the SSD stack is visible and two layers are underneath.

Each detector comprises 2048 strips with 1024 read out by 8 ASICs on each side.

The readout cycle of the SSD detectors is synchronized with the RF signal used in the cyclotron at iThemba LABS, such that the detectors are triggered at the beam spill rate of 26 MHz. The SSD readout is performed by a custom ASIC that records a time stamp and a strip address when a signal is detected over a tunable threshold. The system allows two thresholds so that multiple hits per strip can be identified. Data is read out from the ASIC at a rate of 104 MHz, allowing up to 4 channels to be read out per ASIC per readout cycle.

The four tracker units are arranged so that there are two located before the patient and two afterwards. This arrangement allows the reconstruction of proton vectors entering and exiting the patient. By synchronising the detectors to the beam spill rate, protons from individual beam spills may be tracked across the four detector units [24].

2.2.2 Range Telescope

The PRaVDA range telescope is a range measurement detector and uses 21 layers of SSDs to measure residual proton range. Hits in the SSDs are registered along with a timestamp derived from the beam clock so that 1D proton tracks can be constructed offline. By operating at a sufficiently low beam current, individual protons may be

discriminated by their time stamps and their residual range is determined by the number of detector layers the proton is tracked through before coming to a stop. Each detector layer is separated from the next by absorber sheets of PMMA plastic measuring 2.0 mm thick, designed to increase the WET of each layer. The WET of the whole range telescope defines the maximum residual proton range that can be determined by the system. This is the dynamic range.

In the current set up, a proton must travel be tracked to at least the third layer of the range telescope in order to be considered as a candidate for use in reconstruction. This means that the minimum residual proton range in water that is detected is 3 times the WET of the detector layer. The detector layer comprises 150 µm of silicon and 2 mm of PMMA. The WET of a material is the material thickness multiplied by its RSP. The RSP of PMMA is approximately 1.16 and the RSP of silicon is approximately 2.15, giving each layer a WET of

$$\mathrm{WET}_{layer} = (0.15 \text{ mm} \times 2.15) + (2 \text{ mm} \times 1.16) = 2.64 \text{ mm}. \tag{2.1}$$

From this, we can perform calculations of the dynamic range of the range telescope. The theoretical minimum residual WET that is resolved by the range telescope is approximately 7.9 mm. The theoretical maximum residual WET that is measured is the total WET of the 21 detector layers and is calculated to be 55.4 mm. Interpolating the proton range-energy tables of PSTAR finds that these residual ranges correspond to energies of approximately 28 to 84 MeV. The WEPL of the proton is determined by subtracting the measured residual WET from the initial range of the proton beam. For a proton beam with an initial range of 116.8 mm in water, after subtracting the WET of the detectors in the trackers, the system is capable of resolving a theoretical maximum WEPL of 105.8 mm and a minimum of 57.5 mm.

In practice, the dynamic range is evaluated through a conversion curve and the last layer of the detector is used purely to reject tracks. If a proton in a track hits the last layer we cannot determine whether the proton has stopped in the last layer or exited the back of the range telescope, so if a hit is detected then the data is rejected to prevent errors introduced by misassigning the incorrect WEPL value. Therefore, this reduces the dynamic range of the detector.

Due to the finite lower limit on the resolvable WEPL, when imaging a phantom a range compensator is used. The range compensator comprises a PMMA cube measuring 81 mm on each side with a recess matching the exact size and shape of the phantom being imaged. The idea of the compensator is to ensure that each proton has a WEPL within the dynamic range of the detector. This is important

for protons around the edge of the phantom with low WEPL that may otherwise not be detected. The compensator is corrected for at the reconstruction stage.

The range resolution of the detector is also determined by the WET of each layer. The WET of each layer acts to discretize a nominally continuous distribution of measured proton WET. The WET resolution uncertainty of the range telescope from the discretization is calculated using

$$\sigma_{\Delta} = \frac{\Delta}{\sqrt{12}}. \tag{2.2}$$

where Δ is the WET of one layer. This leads to theoretical WET resolution of ± 0.5 mm. This corresponds to maximum error in the WEPL determination of 0.64%, and meets the requirement that the uncertainty in detector should be lower than the statistical uncertainty in the beam range.

Using sheets of different WET adjusts the dynamic range and the WET resolution of the detector. Using absorber sheets with a higher WET, either with a larger thickness or higher RSP, increases the dynamic range of the range telescope whilst reducing the resolution and vice-versa if sheets with a lower WET are used, therefore a compromise must be made.

As with the trackers, the detector readout cycle is synchronised with the cyclotron beam clock and each proton track is discriminated by using time stamp measurements and a strip address. This becomes less trivial in the range telescope as the proton slows down. An assumption made at the design stage is that each proton will reach the end of its range within one time stamp. At 26 MHz, this time stamp is approximately 40 ns. However, as the protons decelerate they spend more time travelling at a slower speed and hence may be in the detector for longer than a single time stamp. This was accounted for in experiment by running phase sweeps to find the optimal trigger point from the beam clock signal. The percentage of hits correlated from the first PSD to the range telescope was evaluated at each trigger point and the point that gave the maximum correlation was selected.

Initially, a CMOS monolithic active pixel sensor was proposed for use in the PRaVDA range telescope [51]. The proposed design comprised two wafer-scale sensors measuring approximately 9.6 cm x 4.8 cm, abutting along one edge to create an active area of 9.6 cm x 9.6 cm. The pixelated nature of the sensor meant that a large amount of protons could be detected in a single frame, compensating for the sensor's relatively slow readout speed (kHz refresh rate). However, tracking hits from multiple protons over many layers of pixel detectors proved problematic when more than 10 protons were in a single frame. In addition, concerns over the

radiation hardness of the CMOS sensor led the project to opt to use the same SSDs as specified for the tracker units. Despite these concerns, there remains interest in developing CMOS sensors for proton calorimetry and for proton CT [48, 52].

Calibration Curve

In order to use the PRaVDA range telescope as a range detector, a calibration is performed so that the last layer that a proton hits in the range telescope is known as a function of WEPL. The calibration curve was constructed by exposing the range telescope to protons that have traveled through a known thickness of PMMA calibration sheets placed at the isocentre of the proton CT system. The WET of each PMMA sheet was measured experimentally, therefore the proton WEPL in each calibration measurement is known. The distribution of proton last-layers is then constructed. The mode last layer, where most of the protons stop, is recorded. A linear fit is performed between the mode last layer and the WET of the PMMA calibration sheets to determine the WEPL of each proton that has travelled through as a function of the last-layer.

A linear fit is chosen because the total range in water of the proton should be a linear combination of range in the PMMA and range in the range telescope. The residual range should approximately be

$$\mathrm{WET}_{sample} = R_{total} - R_{res} = R_{total} - (L \times \mathrm{WET}_{layer}) \tag{2.3}$$

where L is the last layer. A linear fit would provide a negative gradient with a magnitude approximately equal to the WET of a single layer. By counting protons arriving at each layer in a Monte Carlo simulation of the PRaVDA system, we are able to confirm this theory. The intercept of the fit should be equal to the initial range of the proton beam. In practice the magnitude of the gradient is slightly lower than the WET of an individual layer. This appears to be an artefact in the data collection in the experiment and could be due to noise hits in the detectors being correlated unintentionally with proton hits. This has the effect of reducing the effective WET of each initial layer, therefore reducing the dynamic range of the range telescope.

As expected, the experimental fit is linear up until layer 21 at which point the WET of the calibration material is too small to be resolved due to protons escaping from the rear of the range telescope. Because the 21st layer is used to reject proton tracks, we can calculate that the lowest WET able to be measured by the range telescope is 66.2 mm, compared with the theoretical value of 60.1

mm. The calibration curve is shown in figure 2.4, alongside results from a Monte Carlo simulation and the theoretical calibration curve to show how the experimental results diverge slightly from the theory.

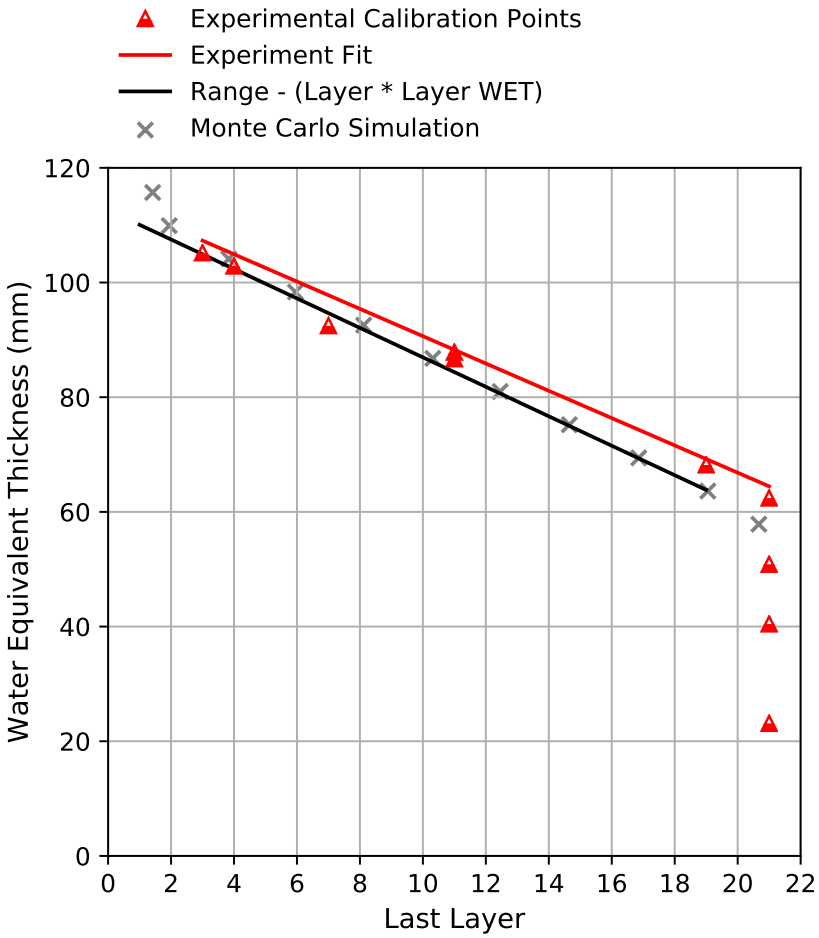

Figure 2.4: Range telescope calibration curve used in the proton CT scan. The WET of the PMMA calibration sheets is determined in Chapter 3. The minimum WET that can be resolved by the range telescope is 66.2 mm.

2.2.3 Data Acquisition

The raw data rate acquired by the PRaVDA system was approximately 9 GB/s. A series of internal and external multiplexers transferred data via camera-link cables to three PCs used to write binary files corresponding to data recorded in the strip detector system and in the front and rear halves of the range telescope. Each PC contained four solid-state hard drives writing data in a RAID0 striped array in order

to maximise the efficiency of the data acquisition system. The binary files were then processed offline to reconstruct the image.

2.2.4 Reconstruction

Before image reconstruction, raw binary files from the detector system are parsed to identify tracks from raw hit information, both in the PSDs and in the range telescope. The PSD reconstruction tracks individual protons by their time stamp to generate the input and output vectors for each individual proton. 1D tracks in the RT are made in the same way and are used to assign a WEPL to the associated proton. This process generates information in a list-mode format, rather than 1D profile conventionally used in image reconstruction.

The reconstruction method used by PRaVDA is a backproject-then-filter (BPF) approach [53]. Whilst standard CT reconstruction is usually performed using filtered back projection [54], BPF offers a number of advantages for proton CT. In filtered back projection, a 1D line profile is constructed from ray projections through a 2D object recorded in each slice. The 1D profile is convolved with a 1D filtering kernel and backprojected through a 2D reconstruction matrix. This is repeated over a number of angles to complete the reconstruction. Proton CT data differs from x-ray CT data as instead of a line profile, the data is in a list-mode format. By reordering the backprojection and filtering, the process removes the requirement of having to bin the proton CT data into 1D profiles is order to reconstruct the image. BPF is one of many novel reconstruction methods proposed for use in proton CT, with many examples of algebraic and iterative reconstructions in the literature [55].

2.3 Chapter Summary

In this chapter, proton CT is introduced and the PRaVDA proton CT system is discussed with particular attention paid to the resolution of the detector systems. The PRaVDA system was used in the following body of work to image two phantoms.

Chapter 3

Relative Stopping Power measurements at iThemba LABS

3.1 Introduction

In this chapter, a water tank dosimetry system is used to determine the range in water of the proton beam at the iThemba Laboratory for Accelerator Based Sciences (iThemba LABS), South Africa [56]. Various materials were inserted into the beam path and the change in the measured proton range in water induced by these materials was used to determine their water equivalent thickness (WET) and hence their proton stopping power relative to water (RSP). These measurements were performed during two experimental visits to iThemba LABS in May 2016 and November 2016.

3.2 Test Materials

3.2.1 PMMA Calibration Sheets

The PRaVDA proton CT system uses a range-based detector to determine the range of the proton beam after exiting the imaging subject, known as the residual range. The calorimeter uses layers of silicon strip detectors separated by PMMA absorbers synchronised with the cyclotron to measure how far each individual proton travels through the absorber medium after exiting the imaging subject. From this residual range, the water equivalent path length (WEPL) that the proton travelled through

in the imaging subject can be determined.

$$\text{WEPL} = \text{Range}_{total} - \text{Range}_{residual} \tag{3.1}$$

The residual range is determined by establishing the last layer in the range telescope that the proton reaches. A calibration curve is then used to determine the WEPL that the proton took. This calibration curve is produced by measuring the range distribution of protons in the range telescope having travelled through a known WET in the imaging medium. This is done by using varying thicknesses of calibration material placed at the imaging isocentre. The calibration material comprised a set of polymethyl methacrylate (PMMA) sheets covering a range of thicknesses. The WET of the PMMA sheets must be determined a priori and this is detailed in this chapter using the water tank. For clarification, the WET is a property of a particular sample, the RSP is a property of the material and the WEPL is a property of each individual proton path. Due to multiple Coulomb scattering, the WEPL that the proton takes through a particular sample is larger than the WET of the sample.

PMMA calibration sheets were used in the commissioning of the PRaVDA range telescope. Each sheet measured 20 cm x 20 cm, with thicknesses of 1 mm, 2 mm, 5 mm, 10 mm and 50 mm. The sheets were manufactured by Carville plastics and were annealed to ensure they were of uniform density. They were finished with a machine polish to ensure the thickness was within a tolerance of $\pm$ 0.1 mm. The sheets had a cut-out on either side so that they could be suspended by a jig in the imaging isocentre. A schematic is shown in figure 3.1. The WET of each sheet was determined, as well as the WET of a few combinations of sheets. The calibration sheets were then used to provide a known WET at the imaging isocentre such that the residual range in the calorimeter could be plotted against the WET of the PMMA in order to construct a calibration curve.

3.2.2 Tissue Equivalent Materials

The accuracy of the proton CT system was validated by scanning a phantom constructed from PMMA containing five so-called tissue equivalent materials (TEMs). TEMs are materials that are selected to replicate the x-ray absorption characteristics of human tissues for radiotherapy dosimetry purposes [57]. These materials are well characterised for use in x-ray dosimetry, however their proton RSPs are unknown. Therefore, their RSPs also must be determined through WET measurements.

The tissues replicated by the TEMs were cortical bone (SB5), lung (LN10),

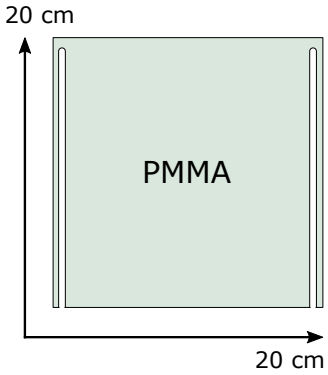

Figure 3.1: A 2D schematic of the PMMA calibration sheet. The cutouts on either side of the sheet allowed the sheet to be suspended in a jig and clamped using threaded bolts.

adipose/fat (AP7), as well as water (WT1) and "average" bone (RB2) which is designed to replicate bone incorporating the hard bone, spongiosa and marrow. The materials were supplied by Leeds Test Objects in cylindrical rods measuring 5 cm in length and 1.5 cm in diameter. The rods were then cut into 1.5 cm lengths, with one section being used for WET measurements and another being used in the construction of a phantom. The phantom was constructed by arranging these tissue equivalent materials in a cylindrical body made of PMMA, and was used to evaluate the performance of the PRaVDA pCT system. The segments for use in WET measurements are shown in figure 3.2. The material's chemical compositions are published online [58] and each sample was weighed and measured in order to establish the mass density of the particular sample. These properties are shown in table 3.1.

3.2.3 Water Tank

The water tank is a standard tool for dosimetry in radiotherapy. An ionisation chamber on a movable stage samples the radiation field in the water from the delivery equipment in 3-dimensions and allows the beam profile to be measured. For proton therapy, the water tank is particularly useful for determining the range in water of the proton beam from the 1D Bragg peak measured along the central axis. From the Bragg peak, the energy and standard deviation of the beam can be determined.

The water tank at iThemba labs was manufactured by Scanditronix and measures 645 mm wide (x-axis), 560 mm high (y-axis) and 675 mm long (z-axis), with PMMA walls that are 14.6 mm thick. The direction of the proton beam is parallel to the z-axis. A circular entrance window with a diameter of 125 mm, for

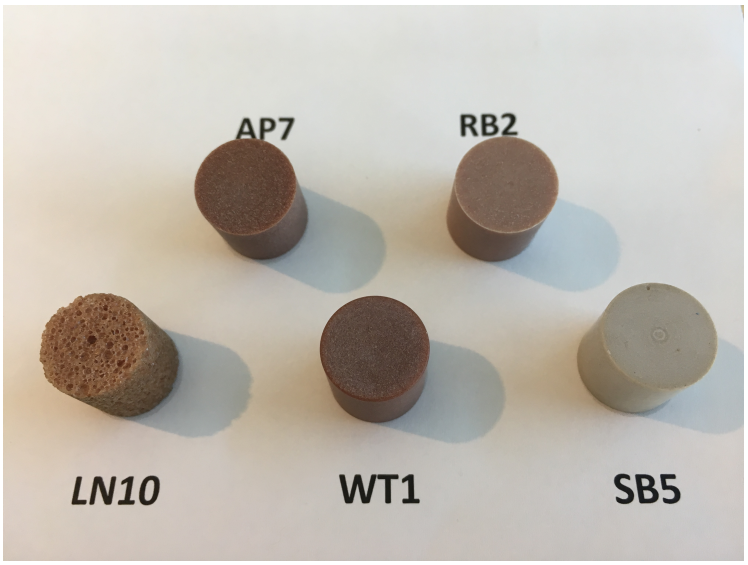

Figure 3.2: The samples of tissue equivalent materials used to measure their RSPs

Material	Length (mm)	Mass Density (g/cm^3)	Elemental composition by mass (%)						
			H	C	N	O	Cl	F	Ca
WT1 (Water)	14.96	1.02	8.41	67.97	2.27	18.87	0.13		2.35
SB5 (Cort. Bone)	15.01	1.85	2.60	30.58	0.98	38.93	0.06		26.85
AP7 (Adipose)	14.97	0.97	8.36	69.14	2.36	16.93	0.14	3.07	
RB2 (Rib Bone)	15.08	1.30	Mixture of SB5 (46.5%), WT1 (53.5%)						
LN10 (Lung)	14.88	0.28	Composition as WT1						

Table 3.1: Lengths, mass densities and nominal atomic compositions of the tissue equivalent material samples. Elemental compositions taken from [58]

measurements along the central axis, has been machined to an average thickness of 3.48 mm to reduce perturbation of the beam. The data acquisition system is calibrated so that the WET of the water tank wall is accounted for in the data output. The data acquisition system reports an integer value of dose between 0 and 1000 and the x, y and z-coordinates of each measurement point.

The water tank ionisation chamber is cylindrical and has an active volume 3.0 mm high and a diameter of 1.9 mm. The Bragg Peak measurement routine moves the ionisation chamber along the z-axis at the centre of the beam and integrates the charge collected in the chamber over a 0.1 mm region as the chamber moves towards the front of the water tank. The charge collected in the ionisation chamber is divided by the charge collected in a reference ionisation chamber, upstream in the beamline, to account for any fluctuations in the beam current. The dose value reported has arbitrary units and is typically scaled such that the maximum dose in the measurement is 1000. The chamber has been calibrated against a local, secondary standard chamber to ensure a uniform and linear response.

3.3 Theory

The WET of a material describes the thickness of the water in which a proton beam would lose the same amount of energy as in the material. Through proton range measurements, the WET of a sample can be determined [59]. If the thickness of the material is known, the RSP can be derived from the same measurements. The procedure is as follows. A reference Bragg peak is recorded with no material in the way of the beam. The material of interest is then placed in front of the water tank, and a new Bragg peak is recorded. The proton range in water is determined for both measurements, and the decrease in the proton range in water caused by the material is recorded as the WET of the sample material.

The median proton range occurs where the dose deposited falls to 80% of the maximum dose deposited, on the distal edge of the Bragg peak [7], referred to here as R_{80}. From this the WET, and thus the RSP can be determined using

$$RSP = \frac{\mathrm{WET}_m}{t_m} = \frac{R_{80,m} - R_{80,w}}{t_m}, \tag{3.2}$$

where t_m is the thickness of the material sample.

The uncertainty on the RSP is calculated in two steps. First the uncertainty in the WET was calculated using

$$\alpha_{\mathrm{WET}} = \sqrt{(\alpha_{R_{80,w}})^2 + (\alpha_{R_{80,m}})^2} \tag{3.3}$$

then the uncertainty on the RSP is calculated using

$$\alpha_{RSP} = RSP \times \sqrt{(\frac{\alpha_{\mathrm{WET}}}{\mathrm{WET}})^2 + (\frac{\alpha_{t_m}}{t_m})^2} \tag{3.4}$$

By making multiple measurements of the WET, the RSP of each material may be calculated by taking a weighted mean of all measurements, defined as

$$RSP_{mean} = \frac{\sum_i w_i RSP_i}{\sum_i w_i} \tag{3.5}$$

where the weighting w is the inverse of the squared uncertainty:

$$w_i = \frac{1}{\alpha_i^2}. \tag{3.6}$$

The associated uncertainty on the weighted mean is then:

$$\alpha_{RSP,mean} = \left(\sum_i \frac{1}{\alpha_i^2} \right)^{-1/2} \tag{3.7}$$

3.4 Method

3.4.1 Reference Measurements

Reference measurements of the proton range were taken using the water tank prior to any measurements using the sample materials, with the experimental set up shown in 3.3. A second set of reference measurements was taken after the sample measurements to ensure that the range of the proton beam remained stable. The range of the Bragg peak is determined by the energy of the proton beam. The energy of the beam reaching the water tank can be adjusted upstream in the beam nozzle by inserting graphite wedge degraders into the beam path that reduce the energy of the beam. The wedges comprise two triangular sections adjacent to each other to provide a continuously variable thickness of absorber. Their position is defined by a control system that moves the wedges appropriately so that the beam delivers a nominal range in water. The nominal range in water set by the wedges refers to the depth at which the Bragg peak reaches 50% of the maximum dose along the distal edge.

In the first experiment (May 2016), all measurements were taken with a full energy beam i.e. the wedge degrader system was not used. This provides a nominal proton range in water of 240 mm. In the second experiment (November 2016), measurements were taken using the full energy beam and two degraded beams. The

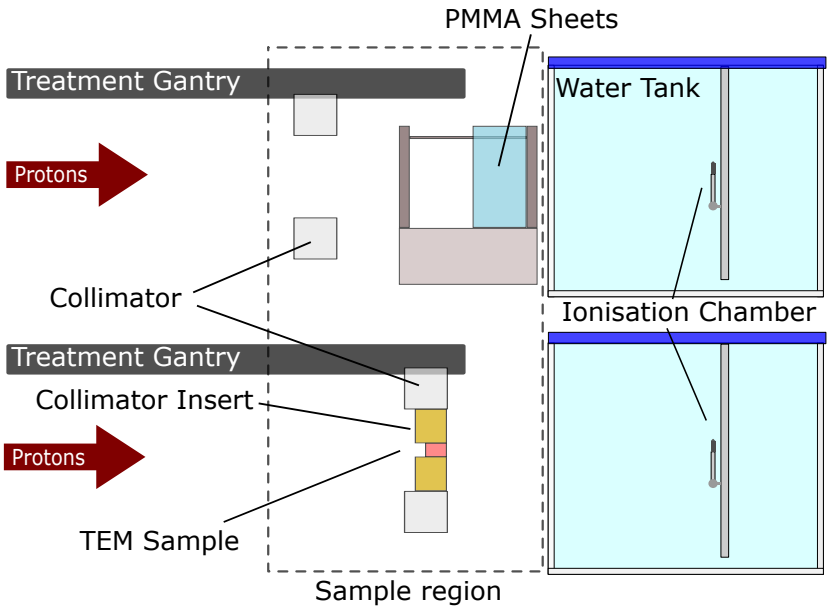

Figure 3.3: Schematic of the water tank measurements, showing the set up for the WET measurements of the PMMA calibration sheets and the tissue equivalent material samples. The PMMA sample, the TEM sample and the collimator insert all removed from the beamline to measure reference beams.

nominal range in water of these beams was 240 mm, 118 mm and 52 mm, roughly corresponding to mean energies of 191 MeV, 125 MeV and 80 MeV at the point of delivery. Reference ranges for each experiment and wedge setting were calculated by taking the mean range of the pre-sample and post-sample beams with the standard deviation as the uncertainty.

3.4.2 PMMA Calibration Sheets

In the first experiment, shown in figure 3.4, each PMMA sheet had its WET measured individually to check for uniformity between the sheets. An H-bridge measuring 16 cm in length was inserted in front of the water tank. The H-bridge held a jig comprising locating pins set in a square arrangement to ensure that each PMMA sheet was held perpendicular to the beam. Each sheet was inserted into the jig and nuts were used to hold the sheets in place. The individual sheets measured 50 mm, 10 mm, 5 mm, 2 mm and 1 mm.

In the second experiment, the WET of combinations of PMMA sheets was measured, using the full range beam and the two degraded beam settings. The

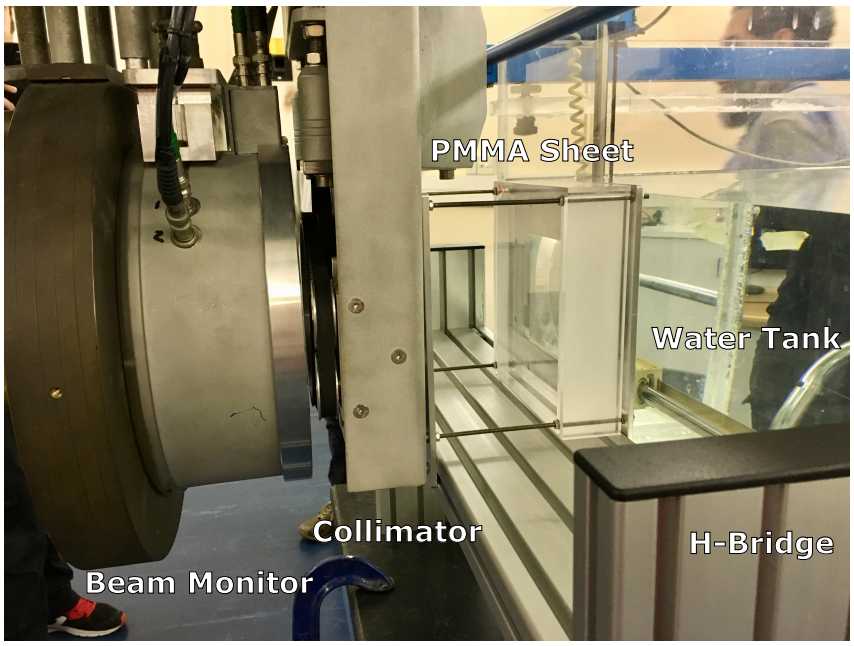

Figure 3.4: Photograph of a PMMA calibration sheet, 50 mm deep in the jig in front of the water tank. The proton collimator is shown on the left-hand side.

combined thicknesses were 50 mm, 20 mm, 12 mm and 10 mm.

3.4.3 Tissue Equivalent Plastics

To measure the WET of the tissue equivalent materials, a brass collimator with a circular aperture 15 mm in diameter was inserted into the end of the proton beamline. The collimator is 60 mm deep and completely stops the proton beam, such that the only protons that can pass must go through the aperture. The tissue equivalent materials were then inserted into the aperture such that they were flush with the front face. This is shown in figure 3.5. Any air gaps around the edge of the tissue equivalent materials had a negligible effect on the range distribution of protons along the central axis.

In the first experiment, each sample was measured with a nominal 240 mm range in water beam. In the second experiment, the samples were first measured with a nominal 240 mm range beam before using the wedge degraders to achieve a 118 mm range beam and a 52 mm range beam. A schematic of the experimental set up is shown in figure 3.3.

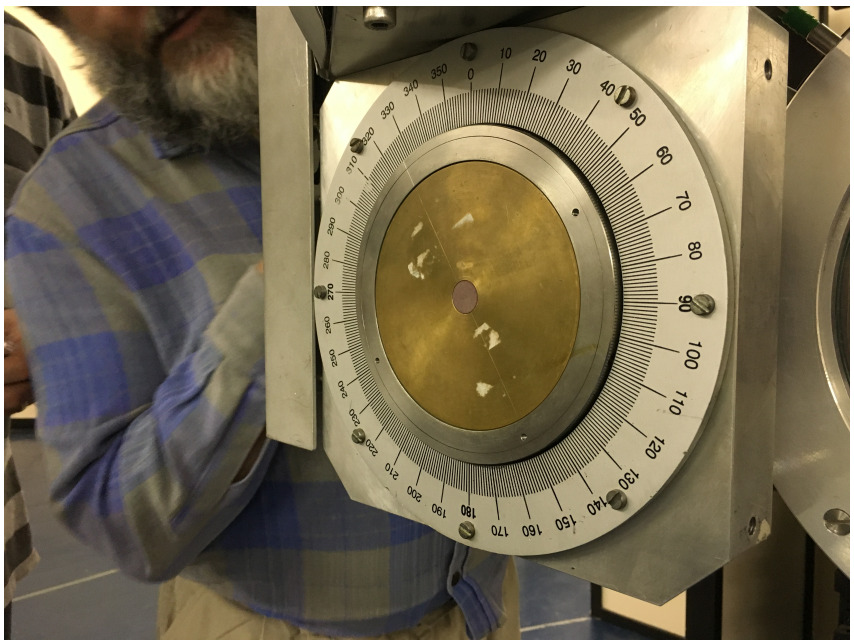

Figure 3.5: Photograph of the brass collimator with a 15 mm diameter tissue equivalent material inserted into the aperture.

3.4.4 Determining uncertainties in the water tank measurements

The range at 80% of the dose maximum was determined through linear interpolation of the measured data points. During the May 2016 experiment, the water tank data acquisition software performed a smoothing routine to reduce noise on the measurement prior to output. However, any range uncertainty due to the measurement noise was not accounted for. In order to calculate the uncertainty on the measurement, for the second experiment the automated smoothing and scaling was disabled and replicated manually.

The smoothing routine used by the water tank is a moving least-squares fit that fits a cubic spline over a window of 31 points. Whilst the smoothing algorithm is proprietary and no further information was supplied by the manufacturers, the description of the smoothing routine is comparable to a Savitzky-Golay filter. Therefore, a Savitzky-Golay filter was applied to the raw dataset, comprising 41 Bragg peak measurements. Other filtering techniques were tested, such as a median filter. A cubic spline fit was performed to the median-filtered data set however the Savitzky-Golay filter outperformed the median filter by offering a lower root-mean-square residual when comparing the filtered data-set to the raw dataset.

An example showing the filter on one Bragg peak measurement is shown in figure 3.6. Residuals were calculated by subtracting the dose measurements of the

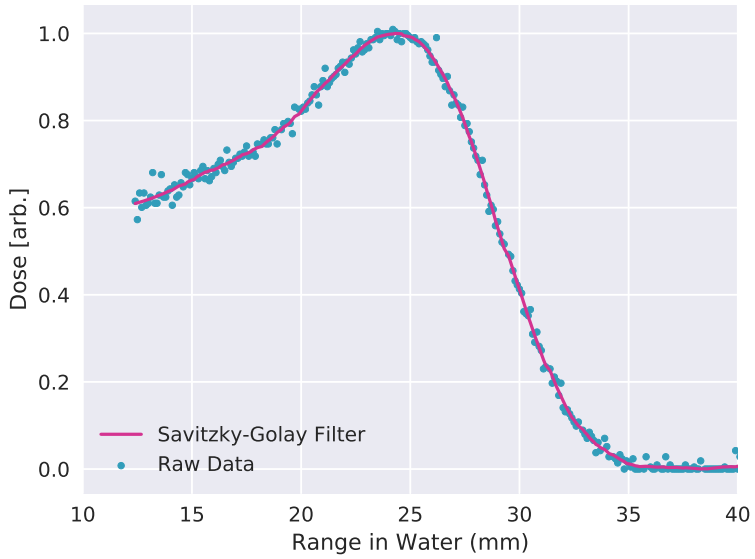

Figure 3.6: Bragg Peak measurement showing raw data points and linear interpolation of filtered data.

filtered data set from the raw data set, divided by the maximum dose measurement at the Bragg peak. A Durbin-Watson test was performed on each Bragg peak measurement from the November data set. The test evaluates whether the residuals are normally distributed around zeros, and therefore a homoscedastic uncertainty may be used. A homoscedastic uncertainty is one that is equal for each data point. A value close to 2 indicates that the residuals are distributed normally [60]. The mean statistic over the 41 Bragg peaks taken over the experiment was 2.2, suggesting that a homoscedastic uncertainty can be applied.

The homoscedastic error bar is calculated by assuming that the filtered dataset correctly describes the Bragg peak, and thus a chi-square test of the raw data against the filtered data would yield a reduced chi-square statistic of 1. From this assumption, the homoscedastic uncertainty is calculated as the root mean square residual over the entire data set:

$$\alpha^2_{dose} = \frac{1}{\nu} \sum (y_{raw} - y_{filtered})^2 \tag{3.8}$$

where ν is the number of data points. The mean uncertainty on the dose was calculated to be 2.24% of the dose maximum. This uncertainty was then applied to all of the dose measurements made during the first experiment. The uncertainty on the range was then calculated by considering the range at 82.24% of the dose

Measurement	R_{80} [mm]
Reference Beam 1	238.24 ± 0.05
Reference Beam 2	238.16 ± 0.05
Mean	238.20 ± 0.08

Table 3.2: Reference beam range measurements from May 2016. Reference beam 1 was taken prior to any sample measurements and reference beam 2 was taken after the sample measurements were complete.

maximum and 77.76% of the dose maximum, accounting for scaling errors due to the uncertainty. However, this uncertainty proved negligible compared to the bin width of the measurement performed with the ionisation chamber, which was ± 0.1 mm.

3.5 Results

3.5.1 Reference Beams

The ranges of reference beams for the experiment in May 2016 are given in table 3.2. The range of the beam decreased by 0.08 mm, most likely due to a slight decrease in the proton energy from the cyclotron, however this range difference is negligible and well within the tolerance of the machine. Small changes in the energy of the beam protons emitted from the cyclotron are expected and usually a multi-layer Faraday cup (MLFC) is used to monitor these changes so that corrective action may be taken.

During the experiment in November 2016, the range of the beam changed more significantly over the course of the measurements. This is shown in table 3.3. This was not accounted for during the experiment due to a fault with the MLFC, and therefore introduces a more significant uncertainty into the reference range of the beam. A simulation study suggested that a range increase of 0.6 mm would be caused by a 0.15% increase in the energy of the protons ejected from the cyclotron which is feasible over a long measurement period, hence the requirement for the MLFC. The measurements can still be used in RSP calculation however we must account for the range shift by using a larger uncertainty. It should also be considered that the accuracy of proton CT relies on confidence in the range of the beam, as the initial energy or range of the beam is set at calibration time. Therefore, there is an uncertainty in the accuracy of proton CT due to uncertainty in the range of the beam.

Measurement	R_{80} (mm)		
	240 mm Beam	118 mm Beam	52 mm Beam
Reference Beam 1	238.49 ± 0.01	116.24 ± 0.01	50.33 ± 0.01
Reference Beam 2	239.14 ± 0.01	116.82 ± 0.03	51.16 ± 0.01
Mean	238.88 ± 0.33	116.59 ± 0.45	50.74 ± 0.54

Table 3.3: Reference beam ranges from the November 2016 experiment. 240 mm, 118 mm and 52 mm refer to the nominal R_{50} range of the beam, set by the wedges. Reference beam 1 refers to measurements taken before to any sample measurements and reference beam 2 refers to those taken after the sample measurements were complete.

3.5.2 PMMA Calibration Sheets

The results of the RSP calculations for each measurement are shown in figure 3.7. As is expected, the magnitude of the uncertainties scales with the size of the sample. This is because the absolute uncertainty in the WETs and absolute uncertainty in the material thicknesses are relatively similar for each sample and is uncorrelated to the sample size. Therefore, for the smaller samples which also have a lower WET, the relative uncertainty becomes much larger. The calculated uncertainty appropriately accounts for most of the RSP results that sit either above or below the weighted mean value in figure 3.7. The measurements from the May 2016 experiment suggest a bias in the 2 mm calibration sheets as they appear to have a systematically lower RSP than all other samples, however the November 2016 experiment shows this is not the case when these five calibration sheets are combined. A possible explanation for this systematic shift is a small energy drift in the cyclotron that was not measured before correcting itself. Another explanation could be an error introduced in the measurement due to range straggling due to the presence of small air gaps.

The reference beam measurements in November 2016 show good agreement with those taken in May 2016 over the three beam energies used. The combinations of PMMA sheets comprising more layers (5 x 2 mm, [5 x 2 mm] + [2 x 1 mm]), have a higher measured RSP than a single 10 mm sheet of PMMA. A possible reason for this is range straggling. The interfaces between the many sheets of PMMA will have small air gaps that affect the energy distribution of propagated protons. A larger spread in energies will affect the gradient of the distal edge of the Bragg peak and affect the range measurement R_{80}. For example, the measured Bragg peak for the 240 mm beam with 5 x 2 mm sheets of PMMA has a measured R_{80} 0.4 mm lower than the R_{80} value for the single 10 mm sheet of PMMA in the November experiment. This corresponds to a WET difference of 0.4 mm, which is 4% of the physical thickness of the sample, hence the discrepancy on the reported RSP values.

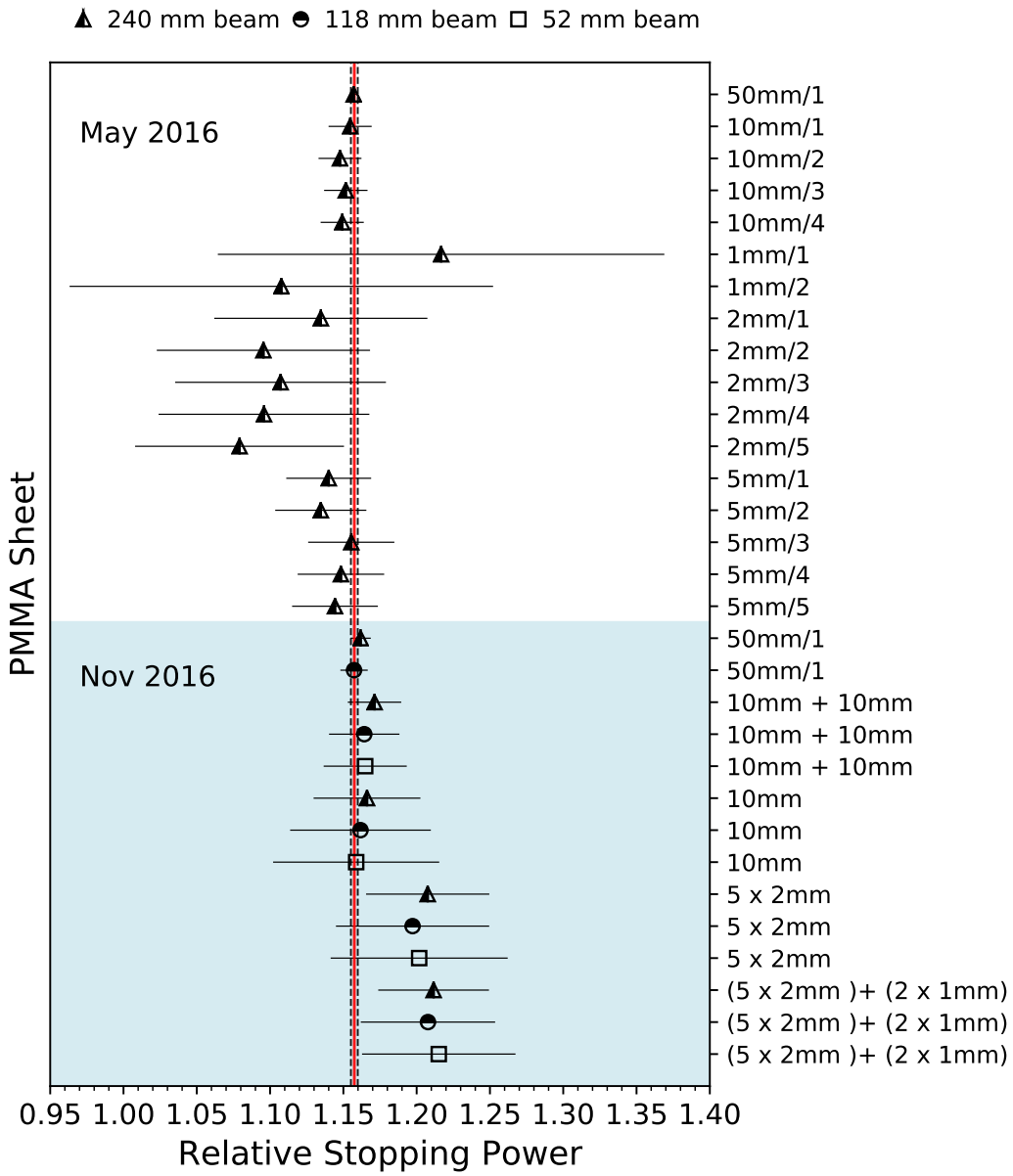

Figure 3.7: RSP results from the PMMA calibration sheets, acquired over two experiments and using proton beams with 240 mm, 118 mm and 52 mm range in waters. The horizontal lines show the uncertainty in each measurement (1σ) and the red line shows the weighted mean result. The combined uncertainty is shown with the two horizontal dashed lines.

However, this range difference is well within the tolerance of the equipment hence the weighted mean value is with the error bars for the majority of the measurements.

The weighted mean RSP over all the measurements is 1.157 ± 0.002, and this is within the error bars of most of the measurement points. This value is also in agreement with an RSP value calculated using the PSTAR database of proton stopping powers [61]. At 100 MeV proton energy, the stopping power of PMMA relative to water is given as 1.158.

3.5.3 Tissue Equivalent Materials

RSP measurements from both experiments are shown in figure 3.8. The first measurement point in each plot is from the range measurements performed in May 2016, with the other three points from the November 2016 measurements. The magnitude of the error bars on each sample is related to the uncertainty in the range of the reference beams.

With the exception of LN10 and SB5, each tissue equivalent material shows an increased RSP with the 52 mm range beam. However, across the energy range used energy dependence in the RSP values should not be evident. Furthermore, reducing the energy of the beam should lower the RSP for material with mean ionisation potentials lower than water. This suggests that a measurement error is likely.

Over all of the material samples, the largest deviation from the weighted mean value is the 52 mm range beam measurement of AP7, where the absolute RSP difference is 0.028 RSP. Sources of this error would be tolerance on the position of the wedge degraders, affecting the range of the beam by ±0.5mm, energy drift in the accelerator and error in establishing the height of the Bragg peak in noisy data. Each one of these is accounted for in the error bars and hence the error bars on each measurement point overlap with the weighted mean value.

With the exception of LN10, the weighted mean RSP for each tissue equivalent material was calculated with a precision of better than 0.64%, providing a measurement that can be used as a benchmark for the PRaVDA proton CT system. The numerical results are shown in table 3.4. The relative uncertainty on the RSP of LN10 is 2.2%. This is because the absolute uncertainty on the WET of each of the samples is comparable, however because the WET of LN10 is less than a third of that of the next lowest WET sample (AP7), the relative uncertainty is larger. A way of reducing this uncertainty and increasing the accuracy of the results would be to use material samples with a larger thickness.

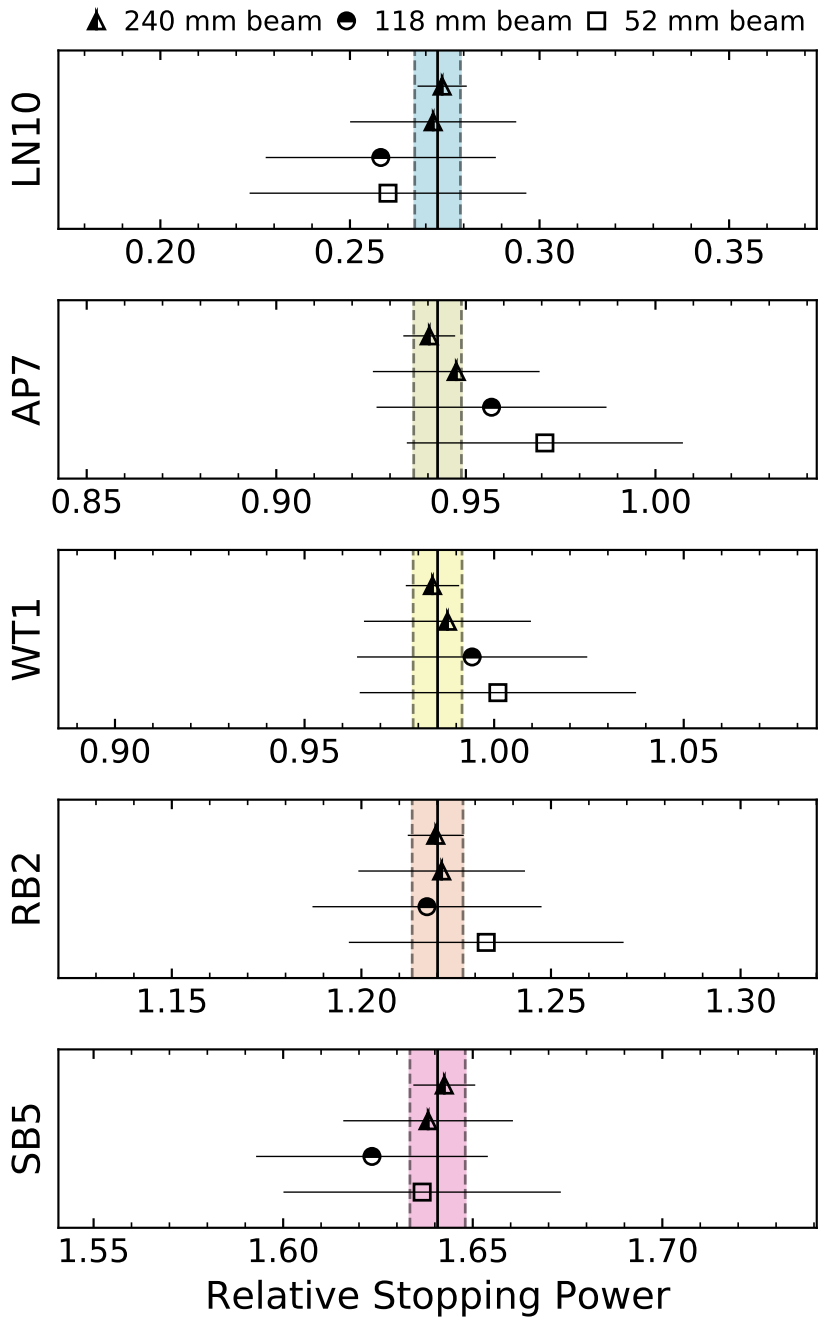

Figure 3.8: RSP results from the tissue equivalent materials, acquired over two experiments and using proton beams with 240 mm, 118 mm and 52 mm range in waters. Each plot is centred on the weighted mean result, with the 1σ uncertainty for each measurement shown. The top data point in each plot is from experiment 1, when the beam was more stable hence there is a lower uncertainty in the measurement than in the next three points.

Material	RSP_{mean}	Uncertainty
PMMA	1.157	0.002
LN10	0.273	0.006
AP7	0.943	0.006
WT1	0.985	0.006
RB2	1.220	0.007
SB5	1.641	0.007

Table 3.4: RSPs calculated from the weighted mean of all measurements.

3.6 Conclusion

Measurements of the WET and RSP of a range of PMMA calibration sheets were taken at iThemba LABS. The uncertainty in the RSP of the calibration sheets is a source of uncertainty in the reconstructed RSPs from the proton CT system, so it is important to keep the uncertainty low. The measured RSP of the PMMA sheets was 1.157 ± 0.002. This value is in agreement with the RSP of PMMA calculated using the PSTAR database [61]. The uncertainty in the RSP calibration sheets corresponds to 0.17% of the weighted mean value. This value can then be used when considering the uncertainty in the proton CT results.

The RSPs of the tissue equivalent inserts were calculated so that they can be used to evaluate the accuracy of proton CT reconstructions from the PRaVDA system. The values were calculated with an accuracy of better than 0.64% for each material with the exception of LN10 where the low WET of the material means that a similar absolute uncertainty in RSP value to the other TEMs leads to a relative RSP uncertainty of 2.2%. This could be reduced by measuring the RSP of a sample with a larger physical thickness.

The work done to evaluate the homoscedastic uncertainty on the dose measurements will be developed further in the following chapter, where a chi-squared test will be used to validate a Monte Carlo simulation with experiment.

Chapter 4

X-ray CT to Proton Stopping Power Conversion

4.1 Introduction

In order to compare x-ray CT and proton CT for use in proton therapy treatment planning, the x-ray CT image must be converted from x-ray attenuation, measured in Hounsfield Units (HU), to proton relative stopping powers (RSPs). In this chapter, a HU to RSP conversion curve is produced using the stoichiometric method proposed by Schneider [12]. This is done so that we can compare proton CT and x-ray CT images of phantoms used later in this thesis.

The method, first proposed in 1996, is widely used in proton therapy treatment planning [11] despite its well documented uncertainties [2]. Whilst some modifications to the Schneider method account for some of these uncertainties [62], the Schneider method is used in other studies as well as in hospitals as a gold standard method for converting HU to RSPs in single energy x-ray CT, so it is appropriate to use it here [63].

The conversion curve generated in this chapter will be used to compare the quantitative accuracy of x-ray CT in reproducing RSPs of tissue equivalent materials in two phantoms, for comparative studies with proton CT.

4.2 Theory

The stoichiometric method for converting x-ray CT Hounsfield Units to proton stopping powers was first proposed by Schneider in 1996 and has since proved to be the most popular and commonly used conversion method for proton therapy treatment

planning [12]. Schneider's method consists of four steps:

1. Take an x-ray CT scan of a number of materials with known properties covering the Hounsfield Unit range.

2. Plot the measured Hounsfield Units as a function of electron density and perform a least-squares minimisation to fit the data and derive the relationship between Hounsfield Units and electron density. This relationship will be scanner-specific and should be performed on each x-ray CT scanner intended for proton therapy treatment planning.

3. Using the fitted relationship found in step 2, calculate theoretical Hounsfield Units for human tissues using tabulated tissue composition data such as those listed in ICRU46 [64].

4. Calculate proton RSPs for the same human tissues using the Bethe-Bloch formula and plot them against the theoretical Hounsfield Units. A piecewise fit will then yield a Hounsfield Unit to RSP conversion curve.

4.2.1 Hounsfield Unit to Electron Density calibration

The Hounsfield Unit (HU), also known as a CT number, is defined as

$$\mathrm{HU} = \frac{\langle \mu_x \rangle - \langle \mu_w \rangle}{\langle \mu_w \rangle} \times 1000 \tag{4.1}$$

where $\langle \mu_x \rangle$ and $\langle \mu_w \rangle$ are linear x-ray attenuation coefficients of the material x and water respectively. This would mean that typically the Hounsfield Unit of air is -1000, the Hounsfield Unit of water is 0 and for bone a Hounsfield Unit of up to around 2000 could be expected. For the following work, scaled Hounsfield Units are preferred where $HU_{air} = 0$ and $HU_{water} = 1000$. This is defined as

$$\mathrm{HU}_{scaled} = \mathrm{HU} + 1000 = \frac{\langle \mu_x \rangle}{\langle \mu_w \rangle} \times 1000 \tag{4.2}$$

In the energy range typically used for x-ray CT imaging (80-160 kV), x-ray attenuation occurs through photoelectric absorption, coherent scattering and incoherent scattering. The linear attenuation coefficient may be parameterised as a sum of these components each with a different Z-dependence [65, 12]. These components are represented by k_{ph}, k_{coh} and k_{KN}, where KN is an abbreviation of Klein-Nishina. The Klein-Nishina coefficient describes Compton scattering for x-ray

energy photons. The scaled Hounsfield Unit becomes

$$\mathrm{HU}_{scaled} = \rho_{e,rel} \frac{k_{ph}\hat{Z}_{eff}^{3.62} + k_{coh}\tilde{Z}_{eff}^{1.86} + k_{KN}Z_{eff}}{k_{ph}\hat{Z}_{water}^{3.62} + k_{coh}\tilde{Z}_{water}^{1.86} + k_{KN}Z_{water}} \times 1000 \tag{4.3}$$

where $\rho_{e,rel}$ is the electron density of the material relative to water and Z_{eff}, $\hat{Z}$ and $\tilde{Z}$ are calculated using the Bragg additivity rule:

$$\hat{Z}_{eff} = \frac{\sum_i w_i Z_i^{3.62\,(1/3.62)}}{\sum_i Z_i^{3.62}}, \tilde{Z}_{eff} = \frac{\sum_i w_i Z_i^{1.86\,(1/1.86)}}{\sum_i Z_i^{1.86}}, Z_{eff} = \frac{\sum_i w_i Z_i}{\sum_i Z_i}. \tag{4.4}$$

Z_{eff} is the effective Z-number of the material and w_i is the fractional composition by weight of each element in the mixture.

A least-squared minimisation is used to find the values k_{ph}, k_{coh} and k_{KN} in equation 4.3 using the known electron density of the materials in the x-ray CT scan and the scanned Hounsfield Units. These k-values are specific to the x-ray CT scanner used and characterise the x-ray response of the CT scanner. Whilst they may be calculated from the literature as they relate to the photoelectric, coherent scattering and Klein-Nishina cross-sections, fitting to measurement accounts to the specific characteristics of the x-ray spectrum from the particular CT scanner.

4.2.2 Calculated Hounsfield Units and stopping powers

Once the scanner specific parameters k_{ph}, k_{coh} and k_{KN} are known, theoretical Hounsfield Units for a set of reference tissues can be calculated. The reference tissues used typically would come from ICRU46 [64], collating work from Woodard and White [66, 67]. These tables provide nominal elemental compositions of human tissues, as well as their mass densities and electron densities. Equation 4.3 is used to calculate these theoretical Hounsfield Units.

As well as these theoretical HUs, RSPs are calculated for the same reference materials using the simplified Bethe-Bloch formula:

$$RSP_m = \rho_{e,rel} \frac{\left(\ln \frac{2m_e c^2 \beta^2}{(1-\beta^2)I_m} - \beta^2\right)}{\left(\ln \frac{2m_e c^2 \beta^2}{(1-\beta^2)I_w} - \beta^2\right)} \tag{4.5}$$

where $\rho_{e,rel}$ is the relative electron density of the material m, I_m and I_w are the mean ionization potentials, or I-values, of the material and water respectively and β is the velocity of the proton in units of c. This formula ignores the shell

Table 4.1: Elemental I-values defined by the Seltzer-Berger rule.

Element, i	Gaseous compounds (eV)	Solids and liquids (eV)
H	19.2	19.2
C	70	81
N	82	82
O	97	106
F	-	112
Cl	-	180
All Others	-	$1.13 \times I_i$

correction, density correction and Barkas corrections to the Bethe-Bloch formula. However it is simple to calculate and is used by the majority of proton therapy clinics [11].

The I-value of the material is calculated using Bragg additivity:

$$\ln I_m = \frac{\sum_i \frac{w_i Z_i}{A_i} \ln I_i}{\sum_i \frac{w_i Z_i}{A_i}} \tag{4.6}$$

where I_i is the I-value of the ith element in the mixture. To improve the accuracy of Bragg additivity, the elemental I-values are modified in a methodology proposed by Seltzer and Berger, adopting new I-values for use in solids and liquids when composing compounds. This modification is summarised in table 4.1 [14].

4.2.3 Piecewise Fit

The calculated RSPs are plotted against theoretical Hounsfield Units and a piecewise linear fit is then used to construct the conversion curve across the HU and density range. Schneider originally did this by joining each point, however the piecewise method suggested by Ödén et al [14] uses a series of fixed knot points to define linear regions. Between the knot points, a linear fit is performed with the constraint that each piecewise section must be contiguous.

4.3 Uncertainties in the Stopping Power Conversion

The uncertainties in the x-ray CT to proton stopping power conversion curve have been studied and reported in the literature [2, 15]. Whilst some systematic uncertainties can be reduced by generating several calibration curves for use on different sizes of patient and specific to certain treatment sites, in clinical use there is a chance

that the incorrect calibration curve may be selected. Therefore, it is safer to account for these uncertainties and design treatment plans with them in consideration.

4.3.1 X-ray CT Artefacts

The quantitive accuracy of x-ray CT is sensitive to a number of factors such as the size of the imaging subject, the number of x-rays used to generate the image and artefacts caused by high density gradients.

The size of the imaging subject affects the quantitative accuracy of the conversion due to beam hardening. The x-ray beam used to generate the image in a CT scanner is polyenergetic, with a non-uniform spectral distribution around the mean x-ray energy. As the x-rays propagate through the imaging subject, lower energy components of the spectrum are absorbed and thus the mean energy of the x-ray spectrum increases [62]. The linear attenuation coefficient of a material is energy-dependent, and the energy-dependence is Z-dependent, meaning materials with a significantly different atomic number to water will have a different energy-dependence to water.. Therefore, it can be seen using equation 4.1 that the Hounsfield Unit value will be affected [2].

The beam current describes the fluence x-rays propagating through the imaging subject. At lower currents, the image reconstruction will be susceptible to Poisson noise. The amount of noise in the image is dependent on the size of the phantom for a given current. This is made more complicated by beam current modulation. Modern x-ray CT scanners will automatically reduce the beam current to reduce the total dose delivered to the patient. A variable current range can be set, however it is difficult to quantify exactly how the noise will manifest in each slice.

Interplay describes artefacts introduced by large variations in density in the image. These large changes can cause ring or ripple artefacts that affect the quantitative accuracy of the Hounsfield Unit measurement [68]

Due to the complex nature of x-ray CT reconstruction, these artefacts are difficult to account for from first principles. However, these uncertainties can be accounted for empirically by analysing scans of different sized phantoms, using a fixed beam current and by varying the position of the sample materials. The variation in Hounsfield Units for each sample over the range of measurements can be used to evaluate uncertainty in Hounsfield Unit measurements before they are converted into stopping powers [2].

4.3.2 X-ray HU Parameterisation

In the stoichiometric method, X-ray HU are parameterised as a function of the effective Z numbers of a material and three k coefficients, as shown in equation 4.3 through a least-squares minimisation to determine k_{ph}, k_{coh} and k_{KN}. In this fit, some uncertainty is introduced. This can be evaluated by calculating residuals between the measured HUs of the calibration materials and calculated HU for the same materials using equation 4.3.

4.3.3 I-values

The I-value of a medium is claimed to be a major source of uncertainty in the stoichiometric method [15], contributing up to a 1.5% uncertainty in the range of the proton beam. However, this study negates the correlation of elemental I-value uncertainties in both the sample material and water. Therefore, this uncertainty estimate is slightly pessimistic [11].

The I-values of individual elements are used to calculate the I-values of human tissues used in the stoichiometric method. The choice of elemental I-values has been covered by several authors [14, 11], as has the contribution of uncertainty in the I-values to the RSP [2]. Yang et al found that when calculating RSPs using formula 4.5, an uncertainty of $\pm 10\%$ in elemental I-values corresponds to uncertainties in RSPs of 0.17%, 0.23% and 0.65% in the lung, soft tissue and bone regions respectively. However, no direct measurements of the RSP were performed so the accuracy of these values was not evaluated.

Doolan et al compared different sources of I-value data, as well as different forms of the Bethe-Bloch formula to calculate RSPs of tissue equivalent materials [11]. Using the Schneider RSP formula (equation 4.5) with I-values taken from ICRU 49, Doolan calculated an RMS error of 0.96% in stopping power between calculated RSPs and directly measured RSPs. The largest error was -2.09%, seen in the lung equivalent material LN-450.

4.3.4 Choice of materials in conversion curve

The materials used to define the conversion curve can influence the accuracy of the curve when calculating the RSP of human tissue. A degeneracy in the conversion curve occurs both close to water, and at higher Hounsfield Unit measurements. Some plastics such as PTFE and Mylar have a disproportionately high RSP given their HU and distort the accuracy of the curve. Conversely, some tissue substitutes such as PVC and sulfur have a lower RSP given their HU. This potentially means

that the conversion curve may perform more poorly for tissue equivalent materials than for human tissues when converting x-ray HU to RSPs. For this reason, the conversion curve used will be constructed using a combination of human tissues and tissue equivalent materials.

4.3.5 Choice of proton beam energy

It is known that the Bethe-Bloch approach is inaccurate for proton energies below 1 MeV however at this point the proton range is small enough (< 0.03 mm in water) that such errors are negligible [62]. More importantly, the RSP of the material may vary across the energy range of the therapeutic proton beam. As the beam loses energy in the material, the absolute stopping power of the material increases. If this increase occurs at a different rate to the equivalent rate in water then the RSP of the material becomes more strongly energy dependent. This occurs mainly in materials with an effective atomic number away from water, such as bone. Yang et al [2] report an uncertainty of upto 0.4% in RSP calculation due to not accounting for the energy of the proton beam, however they note that the range calculation was more accurate when using a proton energy of 100 MeV to calculate RSPs vs an energy of 175 MeV.

4.4 Method

4.4.1 Scanning

Three phantoms were used to generate the conversion curve. The first was a Gammex®RMI electron density calibration phantom comprising a 35 cm cylinder of Solid Water (TM) and cavities for 15 tissue equivalent inserts. Their compositions are described in table 4.3. Each insert is 3 cm diameter and 6 cm in length. The inserts were then individually scanned at the centre of a 20 cm diameter cylindrical water chamber, and 85 mm diameter cylinder ring made from Perspex, referred to as the donut phantom. Each phantom is shown in figure 4.1. The RMI phantom allowed the effect of interplay to be quantified by moving the inserts around. The range of diameters between the RMI phantom, water chamber and donut phantom allowed the variation of HU measurements due to the beam hardening effect to the quantified.

Each scan was performed at University Hospital Coventry and Warwickshire using a modified Radical Brain protocol, with a 300 mA beam current and 120 kV mean energy. Beam current modulation was disabled. Hounsfield Units were

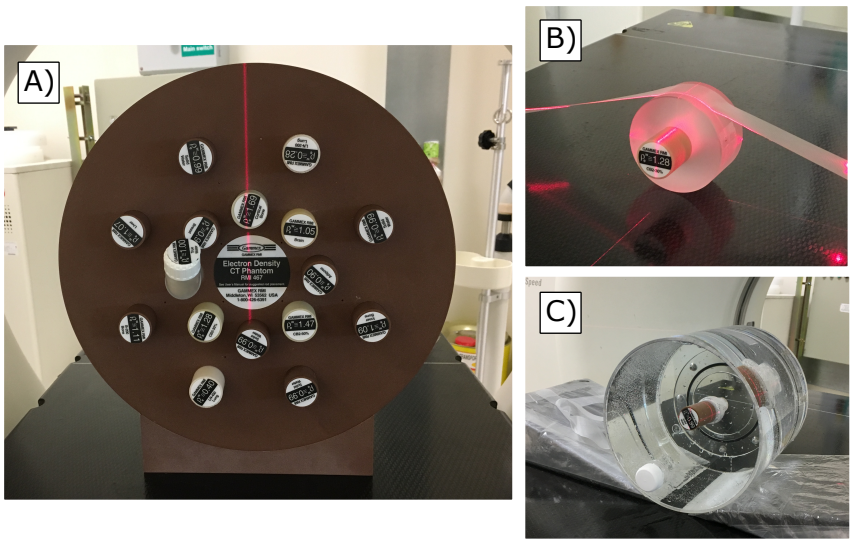

Figure 4.1: Three calibration phantoms used to generate the conversion curve. Shown are a) Gammex RMI Electron Density phantom, b) Donut phantom and c) Water chamber. Phantoms B) and C) both use the inserts from the Gammex RMI Electron Density phantom.

measured over 50 slices on a 300mm^2 circular region of interest (ROI) around the centre of the insert. A single slice from each phantom is shown in figure 4.2.

4.4.2 Parameterisation

A mean Hounsfield Unit measurement was calculated from the three phantoms. A least-squares minimisation of equation 4.3 was performed using the mean Hounsfield Units in order to determine the coefficients k_{ph}, k_{coh} and k_{KN} using MATLAB. Uncertainties on the parameterisation were taken by considering the root-mean-square residual in the lung, soft tissue and bone regions individually [2].

4.4.3 Conversion Curve

Using the fitted k coefficients from the previous section, theoretical Hounsfield Units were calculated for a) tissue equivalent materials listed in ICRU44 and b) tabulated human tissues listed in ICRU46 using equation 4.3. As shown in Schneider's paper [12], the choice of materials can significantly affect the gradient of the conversion curve in the bone region. Omitting Mylar, PVC and PTFE from the fit was considered however it was thought that for use with a plastic phantom, as long as they did not significantly impact the gradient of the piecewise fit, it would be safer to include them.

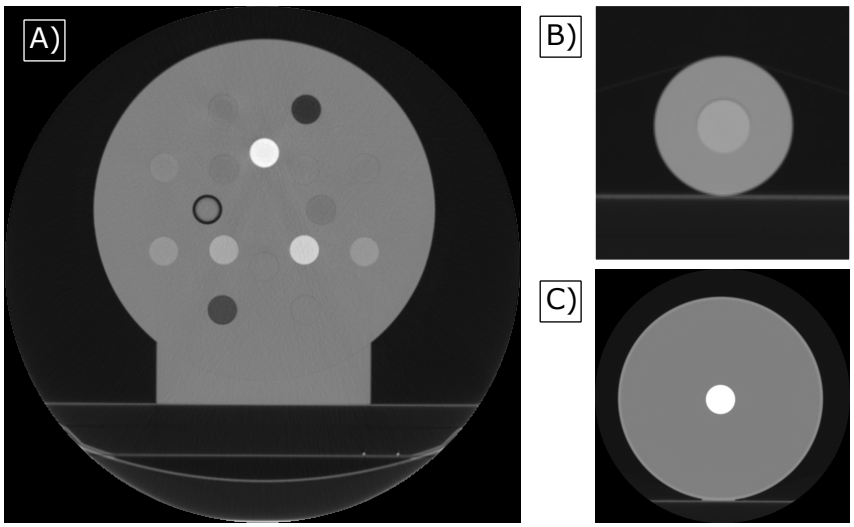

Figure 4.2: X-ray CT images taken from the three calibration phantoms at University Hospital Coventry and Warwickshire used to generate the conversion curve. Shown are a) Gammex RMI Electron Density phantom, b) Donut phantom and c) Water chamber containing the cortical bone insert.

The RSPs of the materials were also calculated using equation 4.5, with their I-values calculated using 4.6. The calculated Hounsfield Units and RSPs were then fitted using a piecewise linear fit, performed using the Python library PWLF [69] with knot points at HU = 0, 250, 880, 980, 1035, 1100, 1340 and 2500. These points were selected by Ödén et al [14].

4.4.4 Uncertainties

Uncertainties in the scanning of the phantom and parameterisation of Hounsfield Units manifest as uncertainties in HU measurement. Therefore, in order to consider the effect that an uncertainty in the HU measurement may have on the RSP, it is necessary to consider the first derivative of the conversion curve:

$$\frac{dRSP}{RSP} = \frac{dHU}{HU} \times \frac{HU}{HU + {}^{b}/_{a}} \tag{4.7}$$

where a, b are the slope and intercept of the conversion curve at the point HU respectively. These uncertainties can then be combined with uncertainties in the calculation of RSPs through an RMS sum. In this work, it was deemed that uncertainties in the x-ray HU measurements and parameterisation formula could be measured. Yang et al [2] studied comprehensively uncertainties in the stoichiometric method therefore their values for RSP uncertainty due to energy dependence of

Source	Uncertainty in converted RSP value (%)		
	0 <HU <800	800 <HU <1200	1200 <HU
CT scan size	3.44	0.65	3.88
Stoichiometric parameterisation	2.80	0.67	1.81
Elemental I-values*	0.96	0.96	0.96
Beam energy used to calculate RSP*	0.2	0.2	0.4
Conversion Curve Fit	0.69	0.08	0.57
Total	4.59	1.80	4.44

Table 4.2: RSP uncertainties in the conversion of x-ray Hounsfield Units to RSPs. Starred values are taken from the literature [2, 11].

the RSP calculation will be used, whilst Doolan's [11] value of RMS error in RSP calculation will be used as an uncertainty due to I-value calculation.

4.5 Results

The results from the x-ray CT scans of the RMI phantom, donut phantom and the water chamber are shown in figure 4.3. The magnitude of the variation in HU measurements due to phantom size increases with the electron density of the material. The strong divergence in the measurement of materials with higher electron density, into the bone region, is due to beam hardening. The tissue equivalent materials in the bone region have a higher effective Z-number than water and consequently their energy dependence of their x-ray attenuation is stronger than material in the soft tissue region. The larger phantom had higher image noise resulting in a larger standard deviation a given measurement, compared to the two smaller phantoms however this is too small to be seen on the plot as an error bar. A mean Hounsfield Unit measurements was calculated for each phantom. Normalised residuals for each phantom compared to the mean result are shown in figure 4.4. Taking the same approach as Yang et al [2], uncertainties in Hounsfield Units were calculated by taking the RMS residual in the lung region, soft tissue region and bone region, corresponding to 0 to 800 HU, 800 to 1200 HU and $>$ 1200 HU respectively. These were 3.44%, 0.65% and 3.88% respectively. Varying the position of the inserts in the RMI phantom resulted in a negligible change in the HU measurement so this was not investigated further.

The mean Hounsfield Units were fitted with equation 4.3 to find the coefficients k_{ph}, k_{coh} and k_{KN}. These values were -0.0006, 0.0001 and 2.1598 respectively.

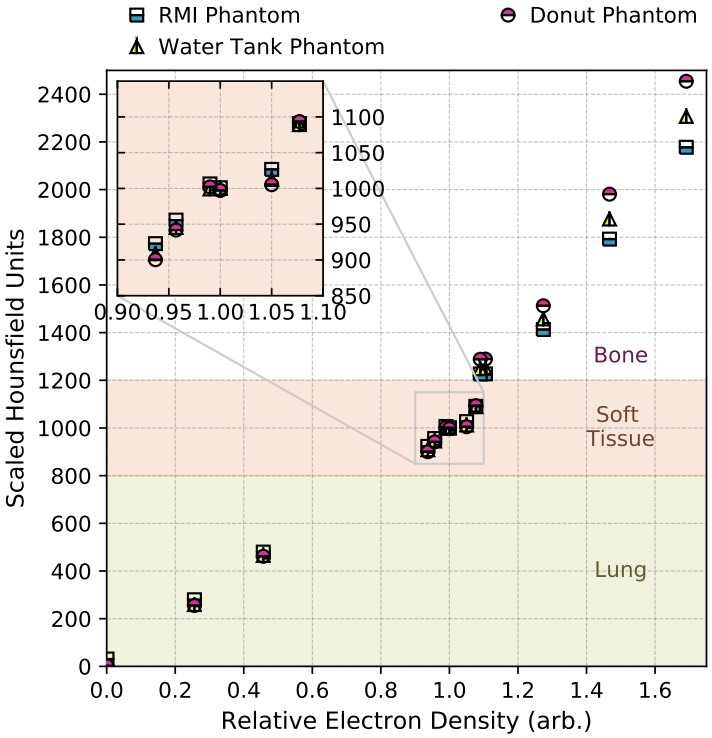

Figure 4.3: Hounsfield Units vs Electron Density for the three calibration phantoms

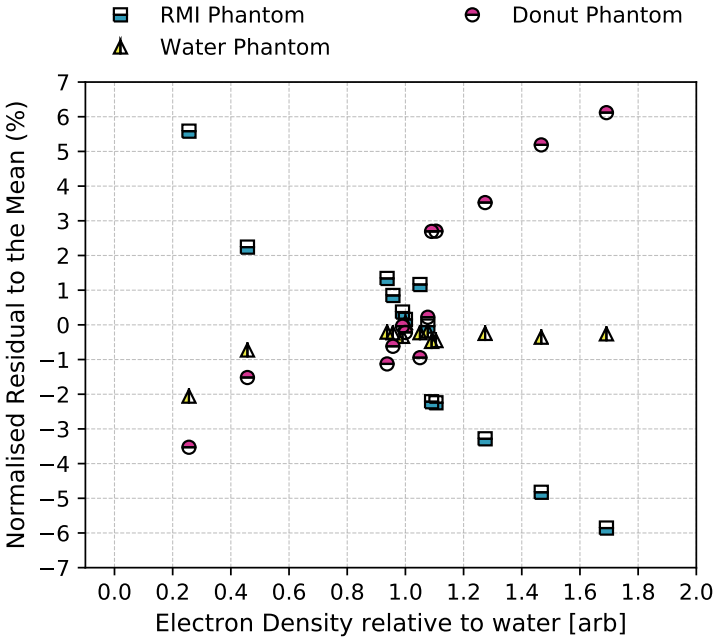

Figure 4.4: Normalised residuals in HU measurements to mean Hounsfield Units

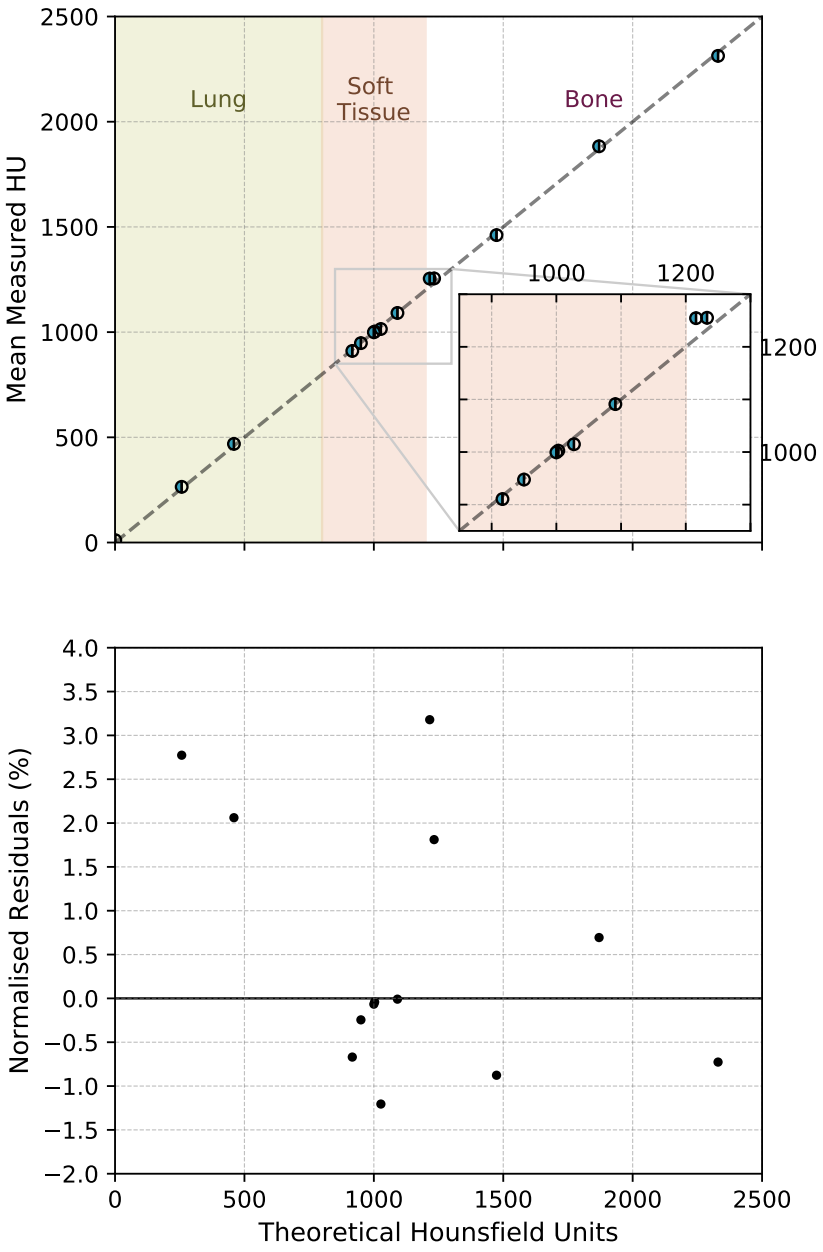

Figure 4.5: Mean Hounsfield Units vs Theoretical Hounsfield Units, calculated through parameterisation of equation 4.3

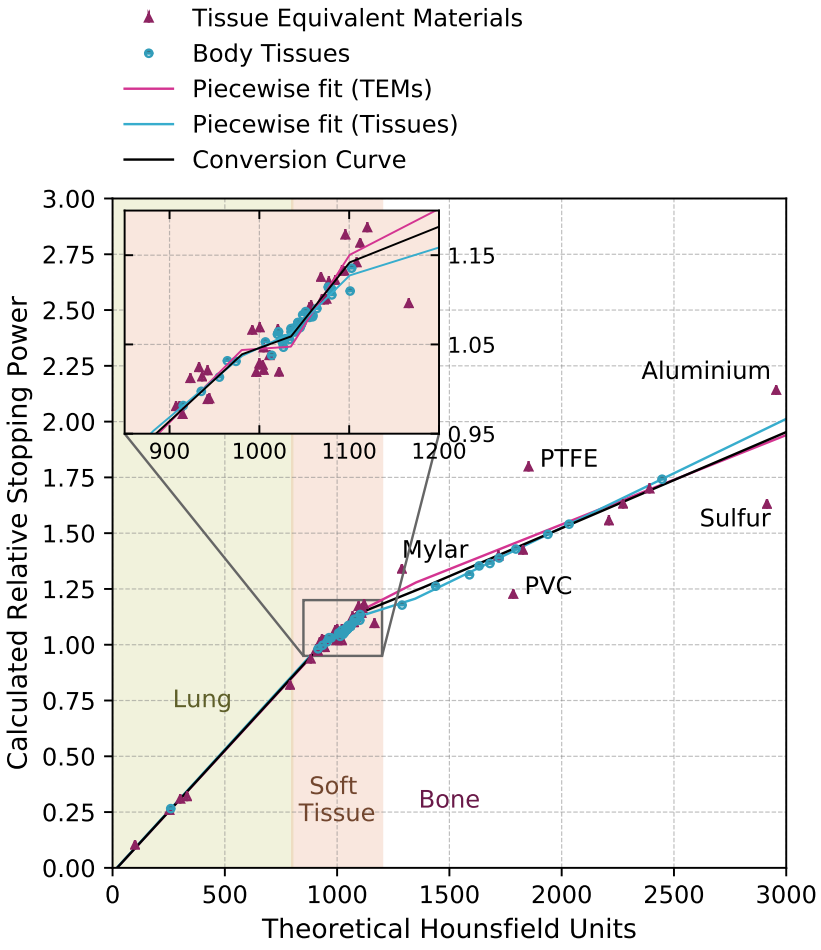

Figure 4.6: Conversion curves calculated based on human tissues and tissue equivalent materials. The materials labelled on the plot are significant outliers, however they were included in the tissue equivalent material fit as their net effect on the fit was minimal. The outliers were useful for defining uncertainties on the fit.

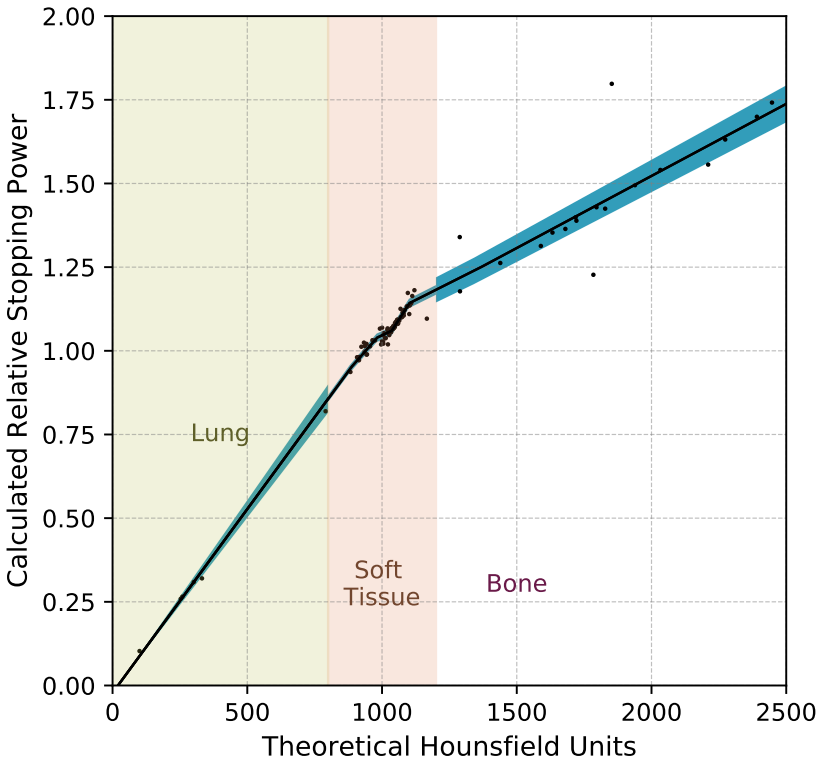

Figure 4.7: HU to RSP conversion curve with 1σ uncertainty highlighted in blue, calculated from the uncertainties evaluated in table 4.2.

Figure 4.5 plots the measured HU units against values calculated using the fit and can be used to evaluate the fit. The RMS residual was again evaluated in the lung, soft tissue and bone regions. The RMS residuals were 2.80%, 0.67% and 1.81% respectively.

RSPs and Hounsfield Units were then calculated for the reference set of body tissues and tissue equivalent materials. A piecewise linear fit was performed to each reference set using the Python library PWLF [69], with knot points at 0, 250, 880, 980, 1035, 1100, 1340 and 2500. This is shown in figure 4.6. It can be seen in the bone region that there is a divergence between the human tissue fit and the tissue equivalent material fit that manifests as an uncertainty in the final RSP conversion. A piecewise fit considering all of the data points was then performed, to be used as the conversion curve. This is shown in figures 4.6 and 4.7, with the total highlighted in blue. A breakdown of the uncertainties is given in table 4.2.

Uncertainties in the RSP due to uncertainties in elemental I-values are taken from [11], as they encompass uncertainties in the calculated RSP of tissue equivalent materials. The uncertainty value due to the beam energy is taken from [2]. The uncertainty in the conversion curve fit takes the RMS residual in the lung, soft tissue and bone regions between the calculated RSP of each material in the piecewise fit, and the RSP value of the fitted curve at each point.

The uncertainties shown in table 4.2 are comparable with those calculated by [2], with the exception of the bone region. Yang reports an uncertainty value of 0.5% in the stoichiometric parameterisation, however for the measurements here the evaluated value of 2.17% is considerably larger.

It can be seen that even accounting for a relatively large uncertainty, the conversion curve may perform poorly when converting HU to RSP of some materials used as tissue substitution. The fit of the conversion curve also overestimates the RSP of materials in the bone region. Optimisation of the knot points may improve the fit however this is outside of the focus of this thesis. Furthermore, the relative quantity of dense materials such as cortical bone in proton therapy treatment sites is low compared to the quantity of soft tissue, therefore the RSP uncertainty in the bone region is largely diluted when considering proton range uncertainty in a therapeutic situation.

4.5.1 Evaluation

The conversion curve was used on an x-ray CT scan of the PRaVDA Bauble phantom. The Bauble phantom contains five tissue equivalent plastic inserts and an air cavity in a cast PMMA sphere with a radius of 75 mm. The inserts and their

compositions are described in chapter 3. The phantom was scanned using the same protocol as the calibration scans. Hounsfield Unit measurements were made using a cylindrical ROI over 10 slices for each insert, and over 30 slices at the centre of the phantom for PMMA, on each scan. A look-up table based on the conversion curve was used to calculate the RSP of each insert and the result was plotted against the RSP as measured in chapter 3. This is shown in figure 4.8.

The RSPs calculated using the conversion curve are over-estimated with respect to the RSPs measured by the water tank. The RMS error on the measurements is 6.7%, with a maximum error of 9.3%. The magnitude of the error in this particular example is much larger than we would expect to see in the clinic. For one, the physical size of the phantom used to evaluate the conversion curve is very small and hence the bone insert in particular is particularly sensitive to this size difference. Any conversion curve used in the clinic would go through a more robust evaluation and quality assurance tests to ensure it is suitable for use before treating patients. However, because the focus of this thesis is on a non-optimised proton CT system, we merely wanted to follow the appropriate steps to obtain an x-ray CT conversion curve that is suitable for use with simple phantoms. One way in which we could improve the accuracy in the conversion is to scan the Bauble phantom inside a water chamber to increase beam hardening and obtain a HU measurement similar to the average calibration conditions.

4.6 Conclusion

A study of the x-ray CT Hounsfield Unit to proton stopping power conversion process yielded conversion curves for use in a comparison of the performance of x-ray CT and proton CT on plastic phantoms. An evaluation of the curve demonstrated pitfalls in the conversion of HU to RSPs when using tissue equivalent materials. The relatively large systematic errors in the measurements are not covered by the uncertainties accounted for when producing the conversion curve, hence proving the need for a more robust system to obtain RSP measurements for proton therapy treatment planning [2].

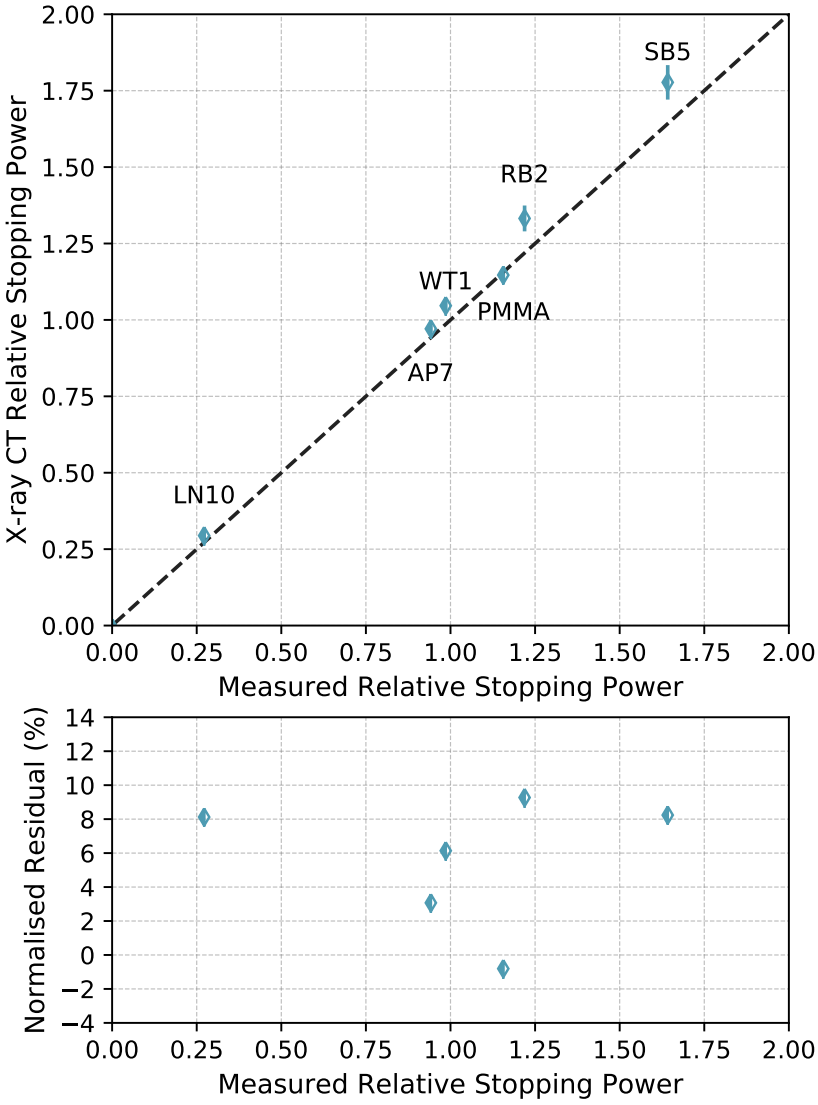

Figure 4.8: RSPs of tissue equivalent materials taken from an x-ray CT scan of the PRaVDA Bauble Phantom calculated using the stoichiometric method plotted against RSPs for the same materials measured using a water tank.

Table 4.3: The mass density, relative electron densities and chemical compositions of the Gammex® inserts from the RMI Electron Density calibration phantom

Material	Mass Density (g/cm^3)	Relative Electron Density	Elemental Composition (%)										
			H	C	N	O	Cl	Ca	P	Mg	S	Si	Ar
LN300 Lung	0.290	0.256	7.43	57.86	1.96	20.71	0.08			11.19		0.77	
LN450 Lung	0.450	0.457	7.44	58.03	1.97	20.69	0.08			11.22		0.57	
SB3 Cortical Bone	1.819	1.691	2.66	30.34	0.99	39.08	0.04	26.48		0.41			
IB3 Inner Bone	1.140	1.090	6.97	56.73	1.79	19.71	0.11	6.38	8.30				
CB2-50% $CaCO_3$ Bone	1.56	1.467	4.03	40.34	1.52	34.13	0.07	19.62		0.30			
CB2-30% $CaCO_3$ Bone	1.33	1.274	5.60	51.77	2.12	28.47	0.09	11.77		0.18			
B200 Bone Mineral	1.153	1.105	6.94	56.62	1.81	19.81	0.11	6.39	8.31				
AP6 Adipose	0.954	0.937	9.44	73.50	2.07	14.86	0.13	0.00					
Breast	0.980	0.957	8.97	71.36	2.25	16.45	0.13	0.93		0.01			
Liver	1.109	1.077	8.40	68.41	2.25	18.50	0.14	2.26		0.03			
Brain	1.049	1.050	9.77	72.13	1.69	16.34	0.07	2.26					
Solid Water	1.020	0.99	8.39	68.59	2.19	18.40	0.03	2.26		0.14			
Water	1.000	1.000	11.19			88.81							
Air	0.001	0.001		0.01	75.53	23.18							1.28

Chapter 5

Bauble Phantom CT: Comparison of x-ray CT and proton CT

5.1 Introduction

In this chapter, we present the first proton CT scan from the PRaVDA proton CT instrument. The proton CT scan is of a phantom known as the Bauble phantom. The phantom was designed to evaluate the accuracy of proton CT in reconstructing RSPs. This proton CT scan is the first to be performed using a fully solid-state system, with semiconductor detector technology being used in both the tracking system and the range telescope. The data presented was acquired at iThemba LABS in November 2016.

Two CT reconstructions of the proton CT dataset were performed, one assuming that the protons took linear paths, whilst the other accounts for multiple Coulomb scattering inside the phantom by backprojecting through non-linear proton paths. Images are presented to qualitatively discuss the differences in image quality between the proton CT reconstructions and a comparative x-ray CT scan. Furthermore, artefacts in the proton CT images are explored and explanations as to their causes are offered.

The accuracy of stopping power reconstruction in proton CT is analysed and compared to both x-ray CT and measurements taken with the water tank. These stopping power results are important in the context of proton therapy treatment planning, where proton CT aims to reduce the uncertainty associated with calculated proton range in order to reduce the planning margins in proton therapy.

Finally, the ability of proton CT to accurately reproduce stopping powers is compared with dual-energy x-ray CT (DECT) by performing theoretical calculations to model range uncertainty. DECT effectively takes two CT scans using x-rays of different energies. The energy-dependence of x-ray attenuation is exploited to provide more information about the Z-number of the material being imaged compared top single energy x-ray CT. For this reason, there is a strong interest in using DECT in proton therapy treatment planning and it should be considered as a competitor to proton CT [70, 71]. A recent study modelled proton range uncertainty on images generated using a number of DECT methods [63]. We perform a similar modelling in order to compare with results with the literature for DECT and standard, single-energy x-ray CT.

5.2 The Bauble Phantom

The Bauble phantom was constructed in order to evaluate the accuracy of proton CT in RSP reconstruction. A spherical phantom body measuring 75 mm in diameter was cast from two pieces of polymethylmethacrylate (PMMA), with vertical recesses designed to contain rods of tissue equivalent materials to create inhomogeneities. These materials were arranged to create a high contrast and low contrast section of the phantom. These two sections contain materials with a broad range of RSPs and a narrow range of RSPs respectively and represent two different challenges for the CT modality: reproducing an image accurately with high gradients in stopping power and accurately reproducing RSPs such that regions with small variations in RSP can be distinguished. The high contrast region of the phantom contains air, LN10 and SB5, whilst the low contrast region contains AP7, WT1, and RB2. These tissue equivalent materials represent lung, cortical bone, adipose, water and rib bone respectively. Their properties and RSPs were introduced and discussed in chapter 3. A cross-section of these two halves is shown in figure 5.1.

5.3 Proton CT Scan

The proton CT scan was completed using the PRaVDA proton CT system described in chapter 3 at iThemba LABS in November 2016. A schematic is shown in figure 5.2. The phantom was placed on a rotational stage controlled by an encoded stepper motor in order to precisely rotate the phantom in steps of 1 degree. A range compensator was attached to the entrance window. The range compensator is a cube of PMMA with a recessed spherical volume in the centre designed to match the

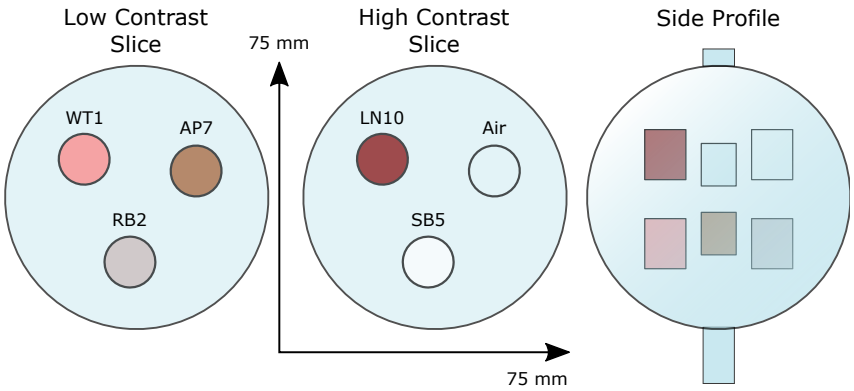

Figure 5.1: A schematic of the PRaVDA Bauble phantom showing the high contrast and low contrast regions respectively.

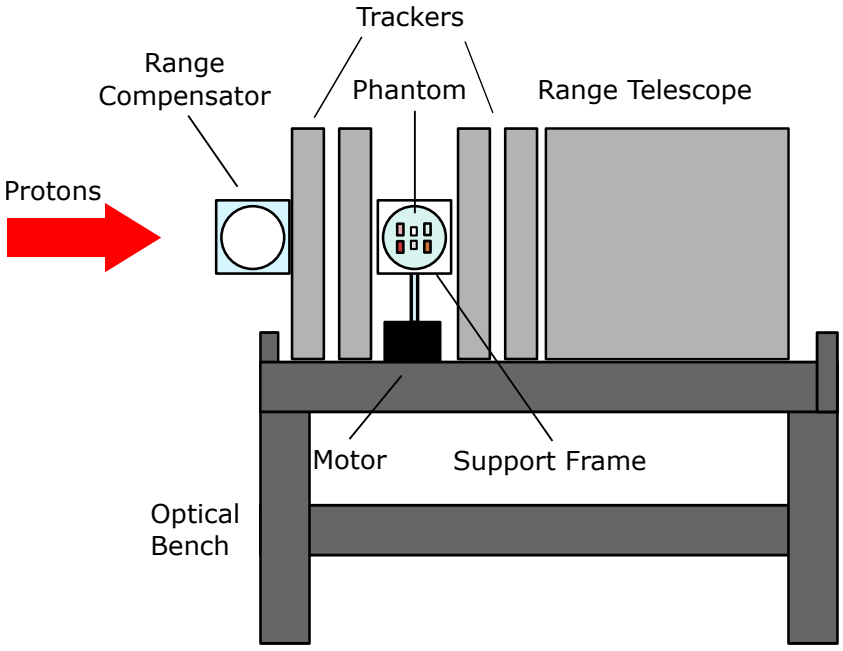

Figure 5.2: A schematic of the PRaVDA proton CT system.

spherical volume of the phantom. The range compensator is designed to reduce the range of protons that would travel through the shallower segments of the phantom. Without this compensator, the protons would escape the range telescope and their residual energy cannot then be determined. The range compensator is corrected for at the reconstruction stage. With knowledge of the trajectory of the incoming proton, the water equivalent path length (WEPL) that the proton took through the compensator can be determined and subtracted from the measured water equivalent thickness (WET) determined in the range telescope.

The system captured proton data for 6 seconds for each angle, operating at a beam current of around 500 pA, corresponding to approximately 2 million protons per second. The total acquisition time was 18 minutes accounting for reinitialisation of the sensors. Time stamps for each beam spill of the cyclotron were used to discriminate individual protons. Cuts were applied to the data to consider 2 million protons per angle that were tracked through the system and did not scatter out. Two reconstructions were performed using a novel backproject-then-filter approach [53], assuming linear and non-linear proton paths. The linear proton path reconstruction assumes that protons have travelled through straight lines through the phantom, and the non-linear proton path reconstruction accounts for multiple Coulomb scattering. Small deviations to the proton path are calculated by calculating linear deviations based on a cubic-spline path.

5.4 Comparison of x-ray CT and proton CT

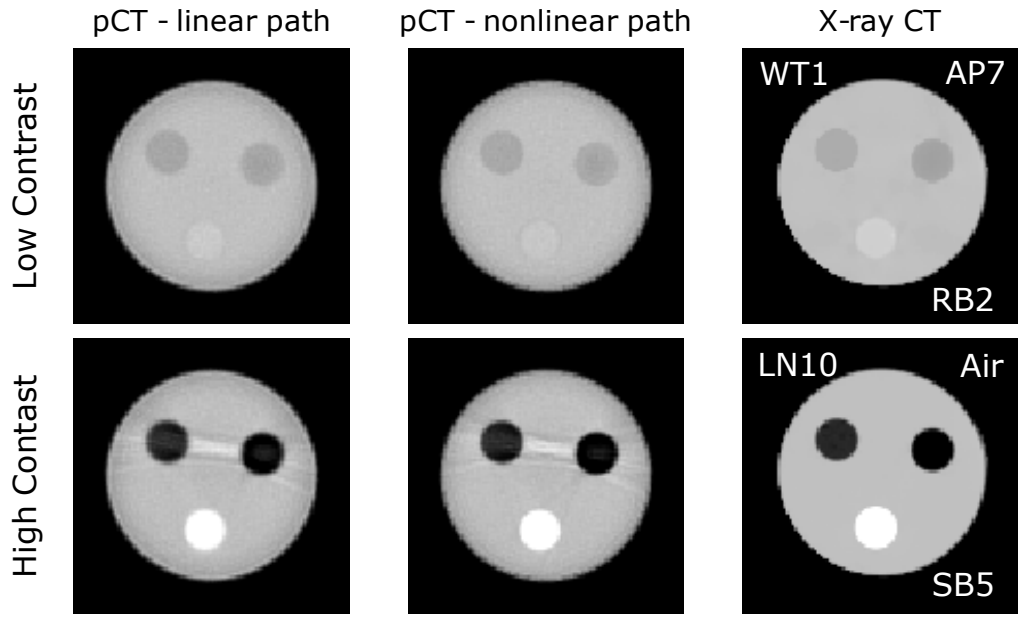

Figure 5.3: A comparison of CT images from proton CT and x-ray CT scans of the Bauble phantom. The labels on the x-ray CT image correspond to the circular inhomogeneities visible in each section of the phantom.

5.4.1 Image Quality

Images have been selected from two proton CT reconstructions, linear proton path and non-linear proton path, and an x-ray CT reconstruction, showing the low contrast and high contrast halves on the phantom. The proton CT images are an average of three 1 mm slices, giving an effective slice thickness of 3 mm. The x-ray CT image has a slice thickness of 2.5 mm. The proton CT images have pixel sizes of 1mm^2 and the x-ray CT scan was rebinned from an image with pixel sizes of 0.46mm to pixel sizes of 1mm^2.

Qualitatively, the non-linear path proton CT reconstruction appears to have sharper edges around the periphery of the phantom body when compared with the linear path reconstruction. However the x-ray CT image is superior in terms of image quality with significantly less noise than both of the proton CT scans. In the proton CT reconstructions, a streak artefact is visible in the high contrast region of the phantom, between the two low-density inhomogeneities LN10 and air. This artefact increases the reconstructed RSP of the PMMA body between the two

inserts. A second artefact in the proton CT scans that is less immediately obvious on the image is a darker ring at the exterior of the phantom. This ring artefact causes a reduced RSP measurement in this region. These artefacts both become more apparent when considering cross-sections through the reconstructed images.

5.4.2 Cross-Sections

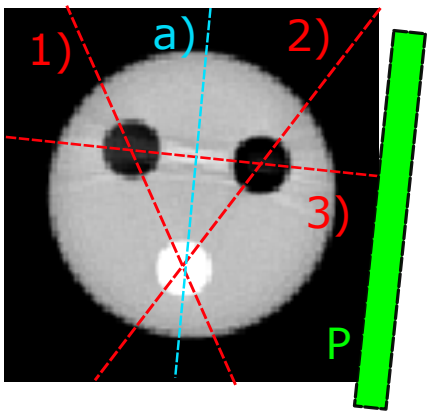

Figure 5.4: Schematic illustrating the position and orientation of cross sections discussed in the following figures. The cross sections labelled 1, 2 and 3 highlighted in red were used to compare imaging modalities, whilst the cross section a) highlighted in blue was used to highlight the streak artefact. The box P represents a 1D projection taken through the image.

Cross sectional profiles have been taken across three lines in the high contrast and low contrast regions. Each profile crosses two inhomogeneities and shows how the reconstructed RSP varies across the image. For illustrative purposes, the orientation of the cross-sectional profiles is shown in figure 5.4, labelled 1), 2) and 3). These profiles shown are averaged over a 1 cm slice thickness and are shown in figures 5.5 and 5.6. The expected RSP value for the relevant materials is also plotted alongside the profiles.

In the low contrast region, the x-ray CT image systematically overestimates the RSPs. This is expected, considering the results in chapter 4 where the converted RSPs of the insert materials were slightly overestimated through the HU to RSP conversion process. However, compared to both proton CT modalities, x-ray CT shows superior accuracy at the edges of the phantom, demonstrating the effect of the proton CT ring artefact. The linear and non-linear reconstructions appear to be very similar in performance. It was considered that a reason for the poor performance at edges could be the size of the image reconstruction matrix. The x-ray CT image

was reconstructed with pixels of size 0.46 mm, compared with 1 mm pixels in the proton CT. However, the ring artefact seems to be more significant than the size of the reconstruction matrix. This is demonstrable by comparing the penumbra measurements.

The penumbra at the edge of the phantom is calculated firstly by considering the distance at which the profile falls from 80% of its maximum value to 20% of its maximum value at the edges of the phantom. Secondly the penumbra from 90% to 10% is evaluated. This is calculated as an average of all three profiles. The proton CT penumbra from 80% to 20% is 2.41 mm for the linear proton CT reconstruction, 2.45 mm for the non-linear proton CT reconstruction and 2.06 mm for the x-ray CT reconstruction. The penumbra from 90% to 10% is 5.62 mm for linear path proton CT, 4.94 mm for non-linear path proton CT and 3.60 mm for x-ray CT. The most significant difference in the penumbra between proton CT and x-ray CT arises when considering the larger penumbra, suggesting that the edge artefact is more significant than the inherent spatial resolution of the image.

In the high contrast region, it can be seen that both proton CT methods reconstruct the stopping power of SB5 more accurately than x-ray CT. However, in the low density regions (LN10, Air), proton CT fails to reconstruct the stopping powers accurately. In the cross section containing both the air and LN10 insert, the streak artefact mentioned above can be seen to distort the reconstructed stopping power of PMMA. The inability of the reconstruction to correctly reproduce low stopping powers particularly in the air inhomogeneity suggests that the ability of the range telescope to resolve high energy protons impacts on the image reconstruction.

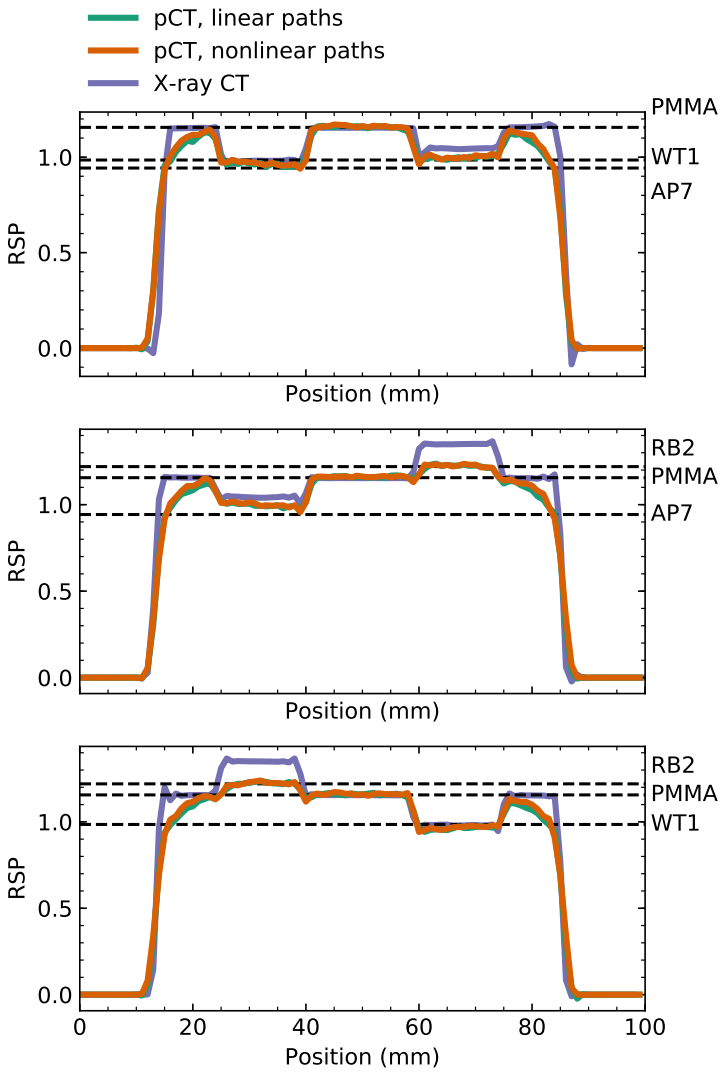

Figure 5.5: Three cross sections taken through the CT images in the low contrast region of the phantom taken at 120 degrees with respect to each other, such that each cross section intersects two inhomogeneities. These cross sections are illustrated in figure 5.4.

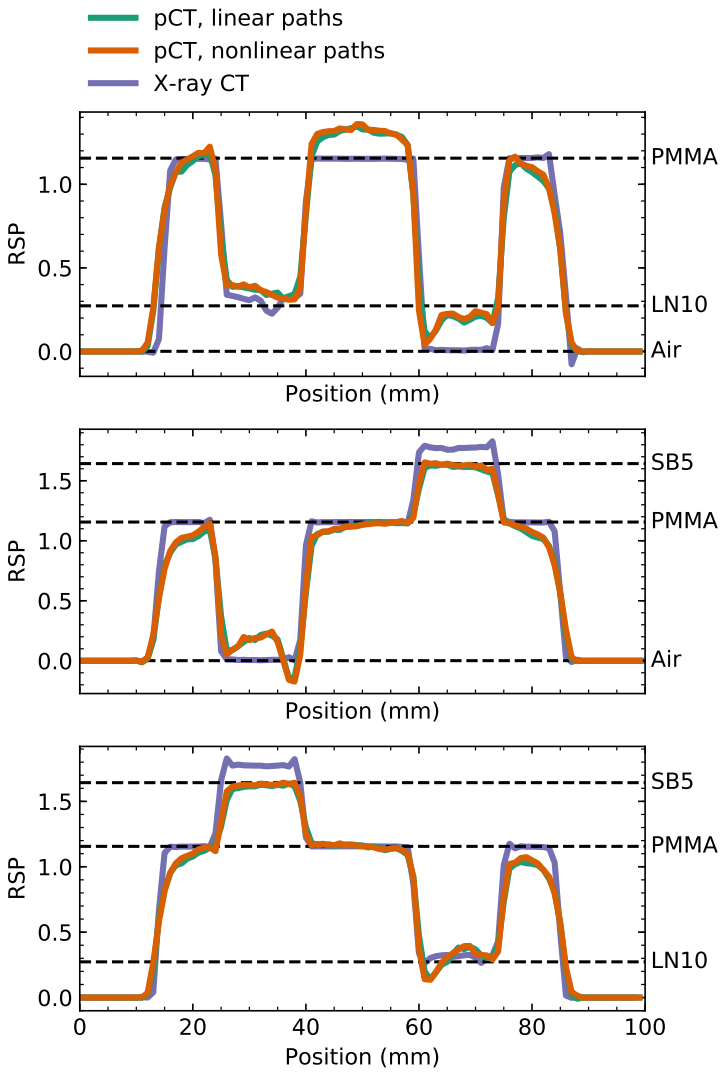

Figure 5.6: Three cross sections taken through the CT images in the low contrast region of the phantom taken at 120 degrees with respect to each other, such that each cross section intersects two inhomogeneities. These cross sections are illustrated in figure 5.4.

The cross section shown in figure 5.7 is taken through a single 1 mm slice at the centre of the phantom, corresponding to a region of homogeneous PMMA. Other than the large penumbra seen at the edge of the profile, no significant features or artefacts can be seen in this slice.

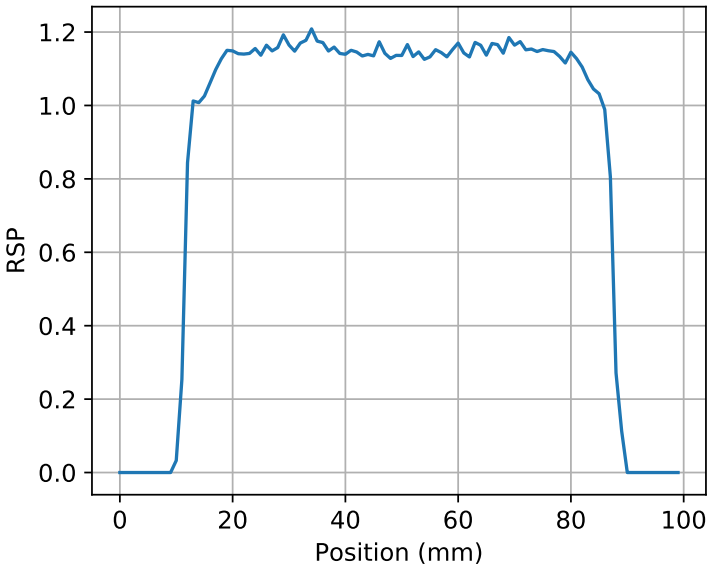

Figure 5.7: A cross section through a homogeneous region of the Bauble phantom.

5.4.3 Artefacts

Condsidering the cross-sections shown previously provides evidence that the artefacts in the proton CT images may significantly impair the ability of proton CT to accurately reconstruct RSP. By considering a 1D profile through the reconstructed image, labelled as 'P' in figure 5.4, an explanation as to the cause of each artefact is offered. The profile was made by rotating the image so that the centres of the LN10 and Air inserts were aligned parallel with x-axis of the pixel matrix, and the RSPs in each pixel were summed along this axis. This projection provides the water equivalent thickness along each row of pixels. An ideal 1D profile was also modelled by creating a matrix of true RSP values from the known geometry of the phantom. Comparison of the experimental and modelled profiles will follow.

Streak Artefact

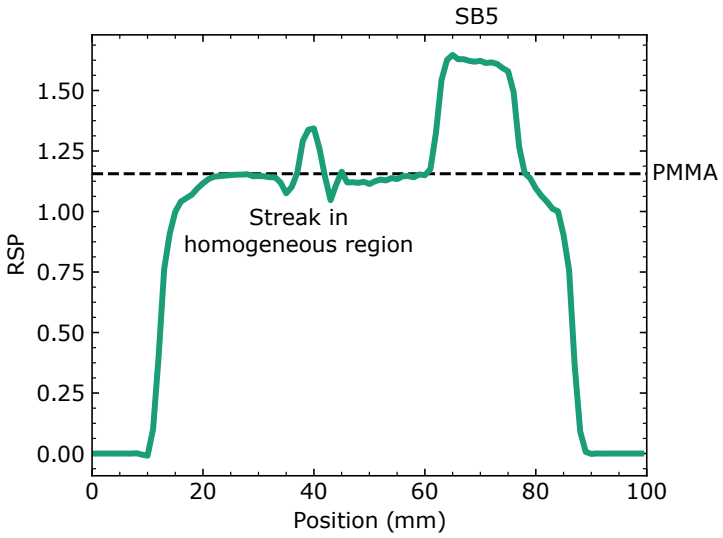

Figure 5.8: Proton CT cross-section through the high contrast region of the Bauble phantom. This profile is shown in blue in figure 5.4.

The streak artefact appears in both the linear and non-linear path reconstruction in the high contrast region, seen in figure 5.3. A 1D slice through the phantom, labelled in figure 5.4 as a), is shown in figure 5.8. This slice shows the features of the streak artefact through the PMMA body. Where the RSP value should be uniform, the streak is a peak in value with a trough at each side. The streak artefact is parallel with protons paths that have been reconstructed through both the LN10 and Air insert, suggesting that these two low-density inserts may be causing the artefact.

A simulated 1D projection of the profile is shown in figure 5.9, alongside a 1D projection from the linear path reconstruction. A radially varying offset to replicate the range compensator has been added to each profile, therefore the profiles should be relatively flat except for the presence of inhomogeneities. The total water equivalent thickness (WET) of the range compensator and the homogeneous region of the phantom is 93.6 mm, and the modelled profile shows this. The two features in the profile show where the proton path intersects the LN10 and Air inhomogeneities and the SB5 inhomogeneity. Where the protons have travelled through both the LN10 and Air inserts, the WET that the proton travels through reaches a minimum of 63 mm. It is at this point that the streak artefact manifests in the 1D profile through the reconstructed image. Comparing the model profile with the image profile suggests that the signal or data used to reconstruct the image is clipped. This could be caused by the range telescope. For now we are neglecting the approximately

4 mm offset between the modelled profile and the reconstructed profile.

The range telescope resolves the WEPL of each proton has travelled through by measuring the range of protons after the phantom. This WEPL is used in the reconstruction and is obtained through a conversion curve. The WEPL of the proton tells us the WET of the material that has been traversed. As shown in chapter 2, there is a limit to the minimum WET that the range telescope can resolve, as higher energy protons which have gone through a lower WET will continue past the end of the range telescope. Hence, the measured WET will be higher than the true value, explaining why the WET signal may be clipped. The point at which the range telescope can no longer resolve the WET is marked on the plot. This minimum is 68.2 mm, meaning that the measured WET through the two low RSP inhomogeneities is outside the dynamic range of the range telescope. During the reconstruction, as the backprojection algorithm combines well-conditioned WET profiles at alternative angles with the clipped WET information, a streak artefact is formed.

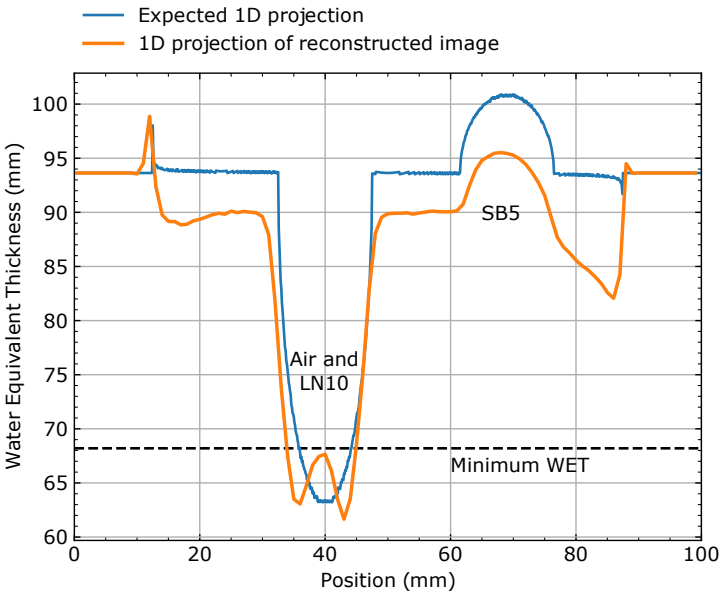

Figure 5.9: Modelled 1D projection through the phantom at location P, as shown in 5.4, compared against the same 1D projection through the reconstructed image.

Ring Artefact

The effects of the ring artefact are visible in figures 5.5 and 5.6, where the proton CT reconstructions underestimate the RSP of PMMA at the edges of the phantom compared to x-ray CT. Over a radius of approximately 10 mm at the edge of the

phantom, the mean RSP averages 0.97, compared to an expected value of 1.156. When summing the WET through the centre of the phantom projection, this corresponds to an underestimation of the WET of approximately 20mm $\times$ 0.1860. This WET underestimation is 3.7 mm, and would explain the offset between the expected profile and the image profile in the previous section. The cause of this artefact is less trivial than the previous artefact however a proposed explanation is that the compensator was misaligned to the phantom during the experiment as discussed below.

Whilst modelling the expected 1D profile, the compensator correction was shifted by 0.5 mm to investigate the effects of possible collimator misalignment. This can be seen in figure 5.10. The chosen value was arbitrary however some new characteristics were introduced into the expected profile that correspond to those seen in the image profile. The peak and trough at the extremities of the phantom edges became larger, and the 1D profile became sloped. In this figure, an offset has also been added to the image projection to account for the ring artefact at the edges of the phantom. The profiles now look much more similar. Whilst determining the exact misalignment is outside of the scope of this work, there is reason to believe that this could be corrected by altering the compensator correction at the reconstruction stage.

At this point it is also worth highlighting that when the WET is corrected for the ring artefacts, the evidence for the clipped WET signal becomes much more clear. This artefact exists in the data and it is not clear how to correct for this therefore we must avoid this clipping during experiment. This most likely would require an improved detector system, or at the very least further optimisation of the current range telescope. In the novel reconstruction algorithm used, 1D profiles are not calculated prior to reconstruction as the proton CT data is in a list-mode format [53]. Computing the 1D profiles from the initial raw data set is computationally expensive. However, if the profiles were to be constructed it may be possible to correct for the clipped data by performing an interpolation between the points on the profile where the projection crosses the WET threshold, although the quantitative accuracy could not be guaranteed.

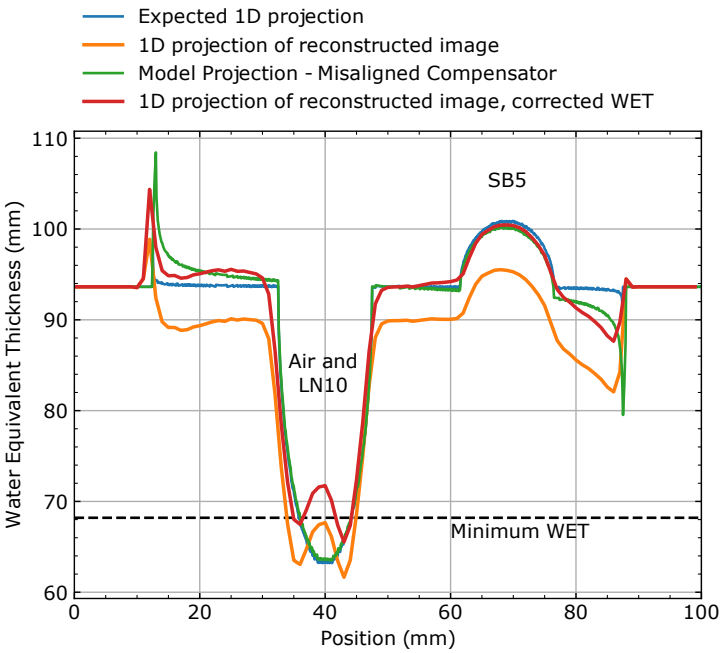

Figure 5.10: Modelled 1D projection through the phantom at location P, as shown in 5.4. The modelled projection was also modified by shifting the compensator correction by 0.5 mm to see the effect. The original 1D projection of the image is also shown with and without a WET correction, applied to counter the loss of WET across the profile due to the ring artefact.

5.4.4 Stopping power results

Mean stopping powers for each material were determined by segmenting slices of the proton CT image into circular regions in MATLAB using a Hough transform function from the MATLAB File Exchange [72]. A total of 28 slices were used, comprising 14 mm depth in the high contrast and low contrast segments of the phantom. These were selected to neglect any partial volume effects occurring at the ends of the inhomogeneities. A first Hough transform detected the radii of the spherical PMMA in each slice, and a second Hough transform determined the centres and radii of the inhomogeneities. Masks were then created for each material in the dataset, with 1 mm subtracted from the diameter of the inhomogeneities to remove the influence of partial volume effects, where a geometric boundary crosses the pixel, on the results. A further 5 mm was omitted from the edge of the PMMA to neglect the influence of the compensator misalignment on the results. A total of 89176 pixels were considered for PMMA and 1918 pixels for each inhomogeneity.

The mean stopping power and the standard deviation was recorded for each

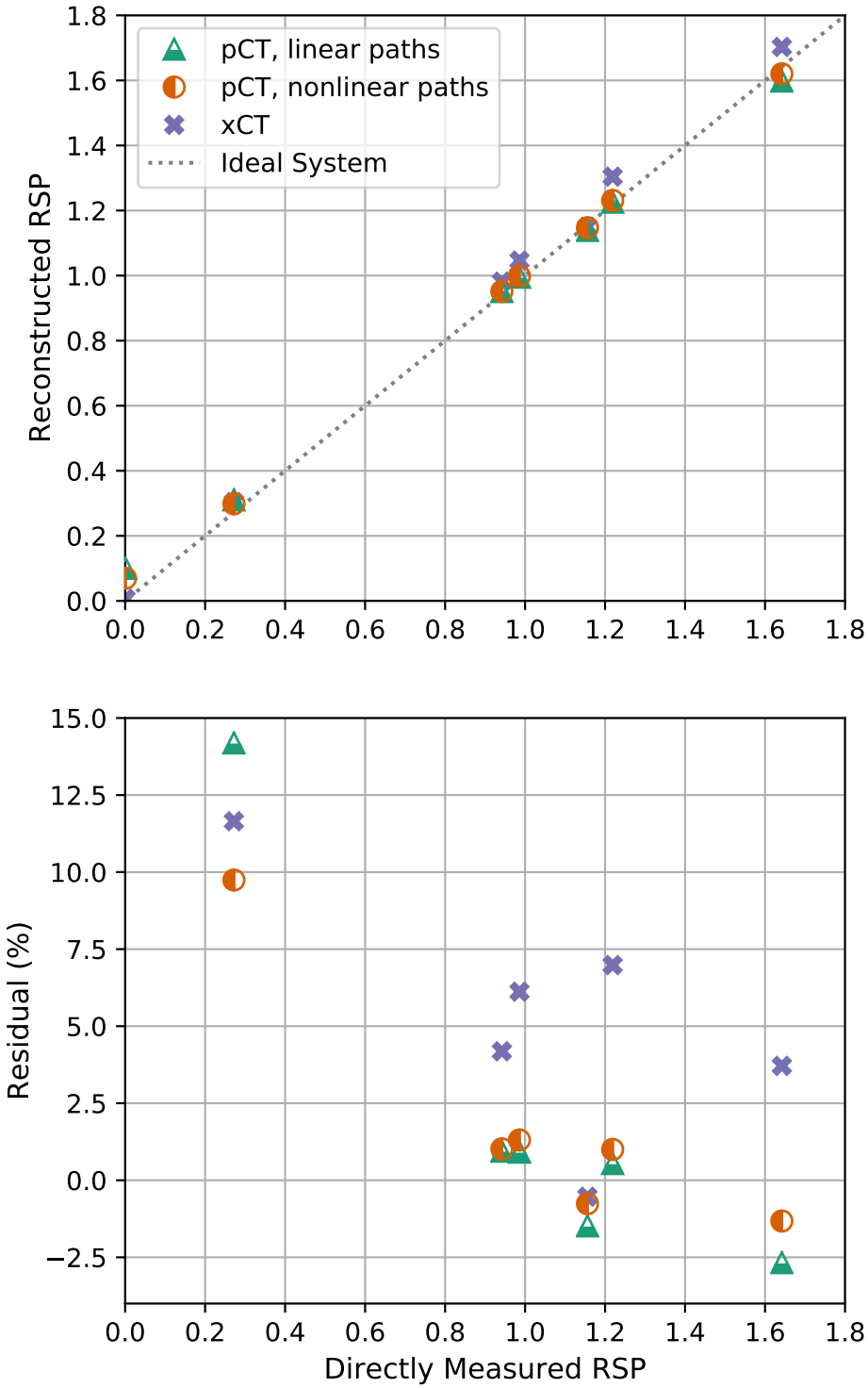

Figure 5.11: RSP measurements from different CT modalities compared to RSPs calculated using water tank proton range measurements.

material. Their results are summarised in table 5.1. With the exception of LN10 and Air, the reconstructed RSP of the materials was within 1.3 % of the value measured by the water tank. The reconstructed stopping power values of LN10 had an absolute error of 0.039 and 0.027 for linear and non-linear proton paths respectively. In 5 cm of LN10, this RSP error would correspond to a proton range-in-water error of 1.95 mm and 1.35 mm respectively for linear and non-linear path reconstructions.

RSP distributions from the non-linear path reconstruction are shown in figure 5.12. The bin width of the histograms are set to be 0.02 RSP, with the axes limits to be the mean value +/- 4 times the standard deviation. The stopping power values from the materials in the high contrast region of the phantom (LN10, SB5) have a much larger standard deviation on their values than those in the low contrast region. The distributions appear to be less Gaussian, with a tail on the left hand side of the PMMA and SB5 distributions. This is caused by the presence of the streak artefact discussed in the previous section.

The mean stopping powers as measured by proton CT are plotted in figure 5.11, alongside the RSPs measured by the x-ray CT. Both the non-linear and linear path reconstructions of the proton CT image outperformed the x-ray CT in terms of accurately reproducing RSPs for the inhomogeneities. Whilst the linear path proton CT reconstruction was marginally more accurate than the non-linear path proton CT reconstruction for the AP6, WT1 and RB2 inserts, in PMMA, LN10 and SB5 the non-linear path reconstruction was significantly better than the linear path reconstruction. The significant difference in density between LN10, PMMA and SB5 in the high contrast segment of the phantom would introduce more proton scatter, hence the non-linear path reconstruction deals with this better than the linear-path reconstruction.

A fit to test the linearity of each proton CT reconstruction method was performed. The fit was constrained so that the function passed through the origin, yielding a function of the form $\mathrm{RSP}_{pCT} = m\mathrm{RSP}_{WaterTank}$. The gradients of the fit were 0.992 ± 0.017 and 0.999 ± 0.012 for the linear path and non-linear path reconstructions respectively, suggesting that both fits were linear within one standard deviation and reinforcing the fact that the non-linear path reconstruction is slightly superior in the reconstruction of accurate RSPs.

Material	True RSP	pCT - linear paths			pCT - non-linear paths		
		RSP	SD	% error	RSP	SD	% error
Air	0.001	0.100	0.133	-*	0.084	0.132	-*
LN10	0.272	0.311	0.096	14.3%	0.299	0.090	9.9%
AP6	0.942	0.951	0.025	0.96%	0.952	0.026	1.1%
WT1	0.986	0.996	0.025	1.0%	0..999	0.025	1.3%
PMMA	1.156	1.14	0.044	-1.4%	1.147	0.042	-0.8%
RB2	1.219	1.226	0.023	0.6%	1.233	0.022	1.1%
SB5	1.624	1.598	0.043	-1.6%	1.620	0.034	-0.2%

Table 5.1: RSP results for the different materials, taken from the two proton CT reconstructions. The evaluated error is the relative difference to the RSP of the material as measured by the water tank. It was not deemed appropriate to evaluate this error for the air cavity because the RSP of air is so small that any deviation from this value is an extremely large percentage.

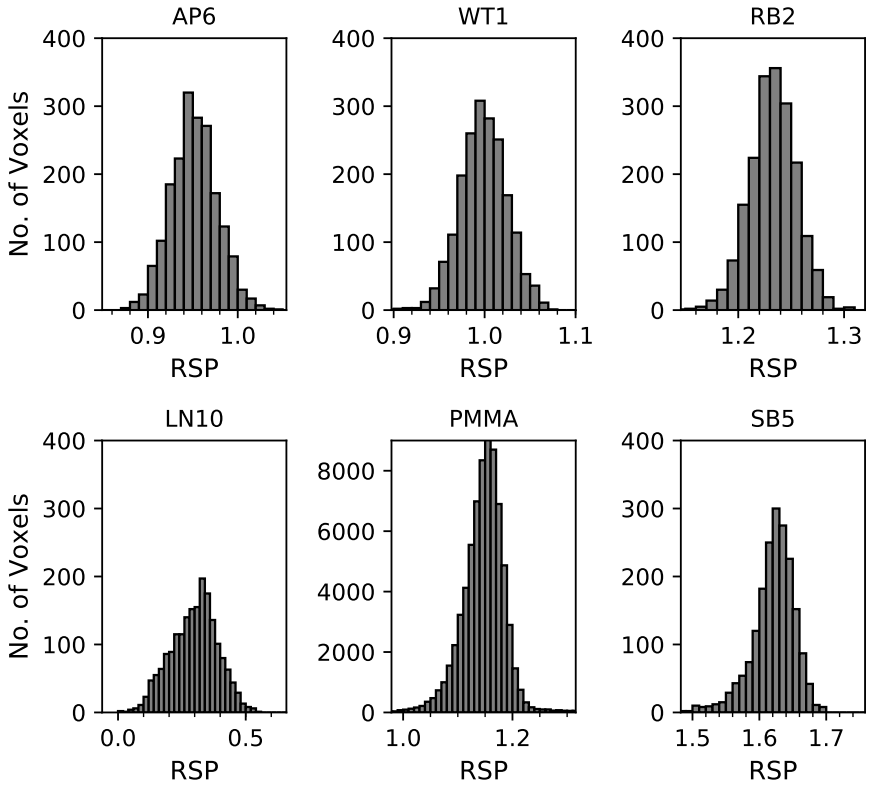

Figure 5.12: Distributions of voxel RSP values for each material in the phantom.

5.4.5 Range uncertainty calculation

The effect of proton CT accuracy on proton range uncertainty was considered next by following the method of Bär et al [63].

Proton range uncertainty in this context refers to confidence in the known proton range. The range uncertainty will be affected by systematic errors in the reconstructed stopping power, and also by random error seen in the distributions of RSPs, for example caused by noise in homogeneous regions. In order to estimate range uncertainty, the RSP errors on each voxel were used to resample a model of a proton depth-dose curve used to calculate proton range. Using this result, the effect of RSP errors in proton therapy treatment planning can be explored.

The depth-dose curve is represented as a series of 1 mm pixels, where each 1 mm step represents a voxel of water with an RSP value of 1 and WET of 1 mm. A random RSP error is then applied to each 1 mm step, based on a probability density function of RSP errors calculated from the CT image. For example, if a 1% error is sampled then the RSP of the voxel will become 1.01 with a WET of 1.01 mm. This is repeated along all of the voxels until the total WET along the path is equal to the original range of the beam. The difference between the physical thickness and the water equivalent thickness is then the range error. By repeating many times, a distribution of range errors is constructed.

Both the linear and non-linear path proton CT reconstructions were imported into MATLAB. The RSPs in each voxel were measured in the same way as the previous section, with the values shown in figure 5.12. The relative error in each voxel was calculated by subtracting the RSPs measured by the water tank from the voxel RSP values, and dividing by the water tank RSP value, giving a percentage error shown in figure 5.13. Figure 5.14 shows the distribution of RSPs in the image over i) the whole phantom and ii) the phantom neglecting RSP errors in the high contrast PMMA region, where the streak artefacts described previously affected the quantitative accuracy of the result. The reason for this omission is that this artefact could be removed with a range telescope with a larger dynamic range and it is not an inherent property of the proton CT imaging modality. We opted to include the RSP errors from our bone tissue equivalent materials as well as the soft tissue-like materials in the PDFs to increase the number of samples in our dataset.

The range error calculation was performed with nominal proton ranges of 30 to 350 mm range in water in 10 mm steps. At each nominal range, the depth-dose curve was recalculated 10^6 times and the range error recorded for each calculation. The results from each range error calculation produce a Gaussian distribution at each range value. The mean of the distribution informs us of any systematic uncer-

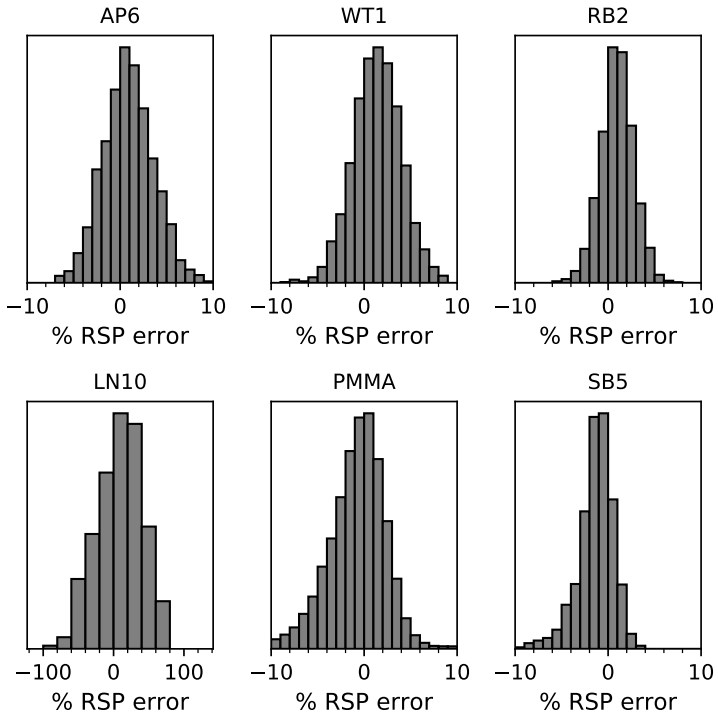

Figure 5.13: Distributions of voxel RSP error percentages for each material in the phantom.

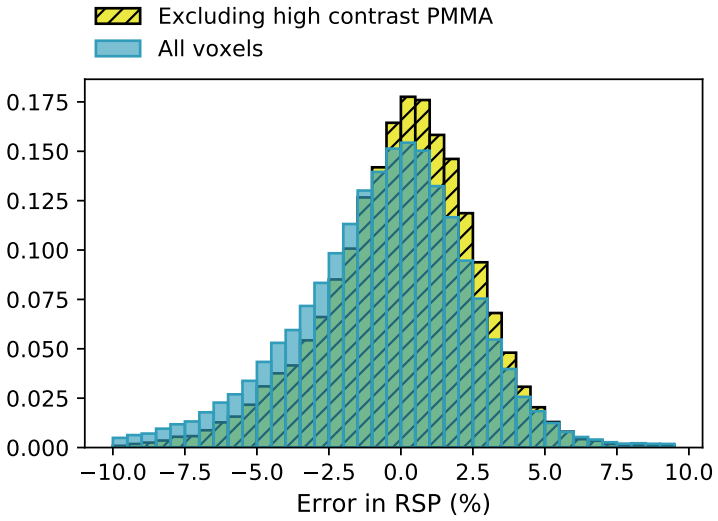

Figure 5.14: Histograms representing probability density functions of RSP errors in the non-linear path proton CT image. The two histograms show the distribution of RSP errors over all of the voxels, and also when the PMMA voxels in the high-contrast region are omitted.

tainty in the reconstructed RSP values and the standard deviation informs the range uncertainty at each point. The mean values and standard deviations are plotted in figure 5.15, with an average value over all of the ranges given in table 5.2.

The linear path reconstruction, including all of the PMMA voxels, has the largest systematic bias in all of the results with a mean range error of 1.31 %, suggesting that the proton CT image underestimates the RSP in most voxels. This range error is reduced to 0.67% if the high contrast PMMA region, where the streak artefact exists, is omitted.

The non-linear path reconstruction including all of the PMMA voxels has a reduced range error compared to the linear path reconstruction. For the data set we have, the inherent bias in the result is reduced by more than 50%. This result is comparable with the linear path result where the artefacted PMMA region is excluded. Omitting the artefacted region with the non-linear reconstruction produces a range error of 0.02% with a maximum range uncertainty of 0.92%, significantly reducing the bias in the result.

RSP error PDF	Mean Range Error	Max Range Uncertainty
Linear Path	1.31%	1.42 %
Linear Path, exc. streak artefact	0.67%	1.07 %
Non-linear path	0.61%	1.29 %
Non-linear Path, exc. streak artefact	0.02%	0.92 %

Table 5.2: Evaluated range errors and range uncertainties based on PDFs of RSP errors in the proton CT images. Results excluding high contrast PMMA refer to PDFs made that exclude parts of the proton CT reconstructions where imaging artefacts affect the quantitative RSP value.

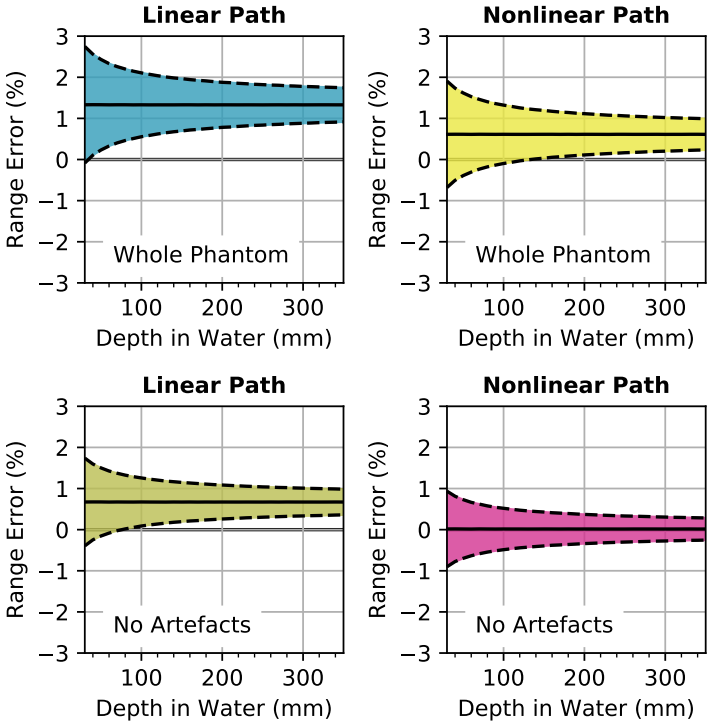

Figure 5.15: Estimated range uncertainty based on resampling of depth-dose curves using RSP error data from the proton CT image.

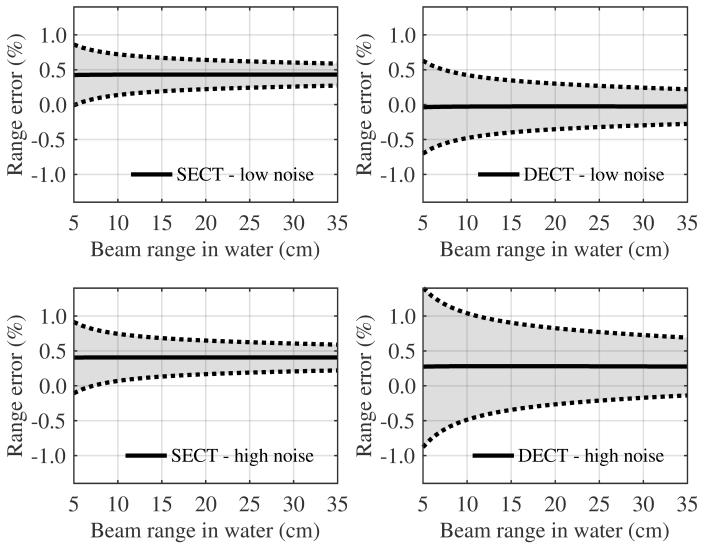

Figure 5.16: Estimated range error results in soft tissue for single energy and dual energy x-ray CT, reproduced with permission from [63]. Low noise and high noise refer to artificial Gaussian noise added to the reconstructed simulated images, in an effort to replicate the noise conditions seen in experiment.

5.5 Discussion

These first results from the prototype proton CT system designed and built by PRaVDA are promising, however they must be considered in the wider context of imaging for proton therapy. Much research has taken place to improve the accuracy of RSP reconstruction, with other proton CT collaborations reporting results with more clinical relevance. As well as proton CT, simulated and experimental studies have shown that dual-energy x-ray CT (DECT) can also deliver reduced stopping power errors compared to standard, single energy x-ray CT (SECT). Furthermore, work with proton radiography has shown that HU to RSP conversion curves can be optimised to reduce stopping power errors, and a number of in-vivo range verification techniques are being developed to monitor the range of the treatment beam after delivery.

In recent years, significant effort has gone into developing DECT as an imaging modality for proton therapy. The equipment required to perform DECT scans is already available in the clinic so many of the technical challenges associated with developing the imaging equipment have already been passed. Recent work by Bär et al demonstrates the ability of DECT to improve the accuracy of RSP estimation and a reduction in range uncertainty associated with proton CT [63, 16]. In these two publications, the authors show simulated results from a humanoid phantom, and experimental measurements using biological tissue.

Bär et al demonstrate the potential for DECT to reduce range uncertainty compared to single energy x-ray CT (SECT), as shown in figure 5.16. This figure shows the range uncertainty associated with the SECT and DECT in soft tissues, calculated as a function of range error on simulated SECT and DECT scans. Each result is presented without noise and with Gaussian noise applied onto the x-ray CT dataset prior to conversion to proton stopping powers so that the effect of image noise on range uncertainty is also considered. This is important because noise is currently a limiting factor in DECT. In a DECT scan, essentially the patient would have two x-ray CT scans, so to reduce the imaging dose given to the patient the beam current is reduced thus increasing image noise. What is noticeable in figure 5.16 is that in the absence of noise, DECT offers the potential to improve on SECT results primarily through reducing range error. However when noise is applied, the DECT method offers little benefit over SECT when purely considering RSP accuracy. There is a suggestion though that the extra data derived from the DECT scan would allow the derivation of specific interaction cross-sections for the object being imaged [73]. These cross-sections would increase the accuracy of proton therapy by allowing

accurate Monte Carlo treatment planning to take place.

Comparing the results of Bär et al with the range uncertainty results presented in this chapter suggest that whilst noise persists in DECT, there is still a need for proton CT. Whilst SECT outperforms DECT and proton CT in terms of the range uncertainty, the range error in our proton CT scan is lowest compared to SECT and DECT.

We now discuss our results in context with an alternative proton CT system. The LLU/SCSC Collaboration recently published work on their Phase II proton CT scanner. Their scanner uses silicon strip detectors as trackers, similar to the PRaVDA instrument however their energy measurements are performed using a scintillator-based range telescope [74, 42]. Results were presented demonstrating the ability of their system to accurately resolve stopping powers in a Somatom calibration phantom, a cylindrical phantom containing cylindrical rods of plastic materials of varying stopping powers. Due to the tiling of the silicon trackers, the imaging area of the LLU/UCSC Collaboration scanner (40 x 10 cm) is much larger than the PRaVDA proton CT system. As a result, a full size calibration phantom could be imaged. The group report an accuracy of better than 3% in reproducing the stopping powers of various calibration plastics [43]. Performing a linear fit of reconstructed stopping powers vs expected stopping powers yields a gradient of 0.994 with a standard deviation of 0.009, provided that the straight line is constrained to cross the origin [42]. A comparative fit of our proton CT data shown in figure 5.11 yields gradients of 0.992 ± 0.017 and 0.999 ± 0.012 respectively. The results suggest that the PRaVDA proton CT system behaves comparably to the LLU/UCSC system. It should also be noted that the Somatom phantom didn't contain a lung-equivalent material, however the LLU/UCSC system has benefited from further development than the PRaVDA system and that imaging the larger, standard calibration phantoms without the need for a compensator is a significant achievement.

Further work by the LLU/UCSC Collaboration shows a proton CT scan of an anthropomorphic phantom [43, 42]. This proved a more significant challenge for the system, where the accuracy of the RSP reconstruction was reduced, primarily due to one outlier data point due to cortical bone. This is because in the anthropomorphic phantom, the thickness of the cortical bone is close to the size of the reconstruction matrix and thus the reconstructed value is distorted by partial volume effects. Whilst the reconstruction matrix could be reduced in size, the extra time requirements to collect and process the extra required proton data would hinder efforts to bring proton CT closer to the clinic. The reconstruction matrix size

is also restricted by inherent limitations of the spatial resolution of proton CT due to multiple Coulomb scattering [22]. One study into the effect of the reconstruction grid shows that for the same level of Gaussian noise, the distribution of RSP errors is reduced with the size of the reconstruction matrix, however typically only small amounts of cortical bone are ever in the path of the proton during treatment therefore we may be able to tolerate the RSP error in bone [2]. In addition to the experimental data gathered by the LLU/UCSC Collaboration, a high-resolution model of the anthropomorphic was generated for use in Monte Carlo simulation [44]. The phantom model was released publicly with the latest version of Geant4. This model could prove extremely useful in benchmarking imaging modalities against each other in simulation, as well as being a useful tool to inform the design of better proton CT systems based on Monte Carlo modelling.

The modern era of proton imaging arguably began with the proton tracking radiography work done at PSI [40]. Through the use of radiography on a dog's head, the water equivalent thickness that each proton travelled through was measured and compared against calculations done on an x-ray CT image that had been converted to stopping powers. The gradient of the HU to RSP curve was varied in order to minimise the errors between measurement and calculation. The error in the calculated integrated WET was reduced from 3.6 mm to 0.4 mm. Whilst there is no indication of the percentage magnitude of this error, if we assume that the average WET of the 20 x 20 cm^2 image is 20 cm we can consider the reduction in range error to be from 1.8% to approximately 0.2%; an order of magnitude's difference. Similar improvements were observed in plastic and animal phantoms by performing proton radiography with a single detector [75], showing that perhaps a full tomographic reconstruction may not be necessary.

There are shortcomings in the PRaVDA data compared to the proton CT and DECT data shown here. For example, the PRaVDA system necessitates the use of a range compensator, which would not be feasible in clinical use where more irregular geometries will need to be imaged. Secondly, the image size in both of the examples here is superior to the PRaVDA system. Both the LLU/UCSC Collaboration and the DECT technology demonstrate their ability to reconstruct non-uniform shapes and larger sizes than the PRaVDA system. A limiting factor in PRaVDA is the energy resolution of the range telescope as well as the detector sizes. Results from the LLU/UCSC Collaboration suggest that abutting strips sensors lose a minimal amount of proton hits and this approach may yield good results if further development of PRaVDA is to take place. However, a limiting factor in both proton CT systems is the ability of the detectors to resolve individual proton signals at

clinical beam currents. This means that the proton CT scan time is still too long to be considered to be feasible in a clinical work flow.

5.6 Conclusions

Considering the above results, there is a need for further study of the PRaVDA system. Furthermore, a more detailed study of the effect of RSP errors on range uncertainty may be necessary, rather than the 1-dimensional study presented by Bär et al and shown above. A Monte Carlo simulation of the iThemba LABS beamline and the PRaVDA instrumentation may provide a useful tool for further development. In addition, the simulation may be used as a diagnostic tool to investigate the artefacts in the existing proton CT image. Provided that a Monte Carlo simulation is validated and can produce realistic results, parameters such as the beam energy, size of the detector elements and phantom geometries can be modified to study their effect on the final image.

These conclusions lead to the work discussed in the following two chapters, where a Monte Carlo simulation of the iThemba LABS beamline is configured to produce accurate dose distributions compared to water tank measurements, and a Monte Carlo model of a dosimetric phantom is generated based on an x-ray CT and proton CT dataset. The Monte Carlo model will allow a direct measurement of the difference in calculated proton range for the same beam based on the x-ray CT and proton CT image modalities, as well as a comparison with a direct measurement of the dose distribution so that the most accurate result can be determined.

Chapter 6

Commissioning of a Monte Carlo simulation of the iThemba Beamline

6.1 Introduction

In this chapter a Monte Carlo simulation of the iThemba LABS beamline is introduced. The Monte Carlo simulation allows study of the beamline and modelling of experiments. An aim of this thesis is to use Monte Carlo to calculate a dose distribution in a phantom imaged with proton CT, using the proton CT image, and compare the simulated dose distribution with an experimental measurement. In order to do this, the Monte Carlo simulation must first be tuned and validated against experimental data, which is done in this chapter. In order to tune the simulation we must first demonstrate that the scoring method is robust to geometric changes, such as the collimator size and the detector size. Secondly, the energy of the primary proton beam entering the beamline must be optimised. Finally, the I-value of the sample of polyethylene used in the phantom construction is found by comparing simulated results against data. Parameters in the simulation were tuned so that the range of simulated Bragg peaks matched experimental measurements described in chapter 3.

We opted to tune the I-value of polyethylene because the material comprises the body of the phantom described in chapter 7. In order to study the proton range in a Monte Carlo model of the phantom, we want to accurately know the properties of the materials. The currently accepted I-value of polyethylene is 57.4 ± 8 eV [57]. Using the Bethe-Bloch equation, this corresponds to an uncertainty in the relative

stopping power of polyethylene of 3.5%. This translates to a range uncertainty of greater than 1 mm when modelling the phantom. We seek to reduce this uncertainty by comparing simulated Bragg peaks against water tanks measurements with a sample of polyethylene in the beam. By adjusting the I-value of polyethylene in the simulation, we can determine a new I-value for polyethylene with reduced uncertainty.

6.2 PRaVDASuperSimulation

The PRaVDASuperSimulation (SuSi) is a Geant4-based Monte Carlo simulation used to model the PRaVDA proton CT system, comprising a modular set-up of beamlines, phantoms and detector systems. A macro-based control system allows the user to select a model of either the iThemba LABS proton beamline or the MC40 cyclotron at the University of Birmingham, a range of phantom options and/or components comprising the PRaVDA pCT system.

Geant4 provides an object-oriented toolkit for performing Monte Carlo simulations of particle transport written in C++ [76]). Included with Geant4 is a large collection of validated interaction data that is frequently updated and is used to accurately model the electromagnetic, hadronic and nuclear reactions that a proton projectile will undergo.

The simulation of the iThemba beamline was initially developed by Steve Peterson and Jeyasingam Jeyasugiththanm from the University of Cape Town [77] in 2009. During the PRaVDA project, the simulation was extended to include detailed modelling of the PRaVDA instrumentation [78]. Over the course of the project, physics libraries in Geant4 have been updated. Most significantly, the I-value of water has been revised from 75 eV to 78 eV [79]. This increases the simulated range in water by 1.2 mm for the full energy iThemba beam.

Geant4 physics lists provide a modular library of interaction models and cross-sections allowing the user to specify relevant physics models for their simulation. In SuSi, the physics list HADRONTHERAPY_1 was selected from the Hadrontherapy Geant4 examples [80] recommended for medical applications [81]. For the energy range relevant for proton therapy, hadronic interactions are calculated using the Binary-Ion Cascade (BIC) model. Electromagnetic interactions are handled using the G4EmStandardPhysics_option4, the most accurate option for medical physics applications. Radioactive decay is considered using G4RadioactiveDecayPhysics.

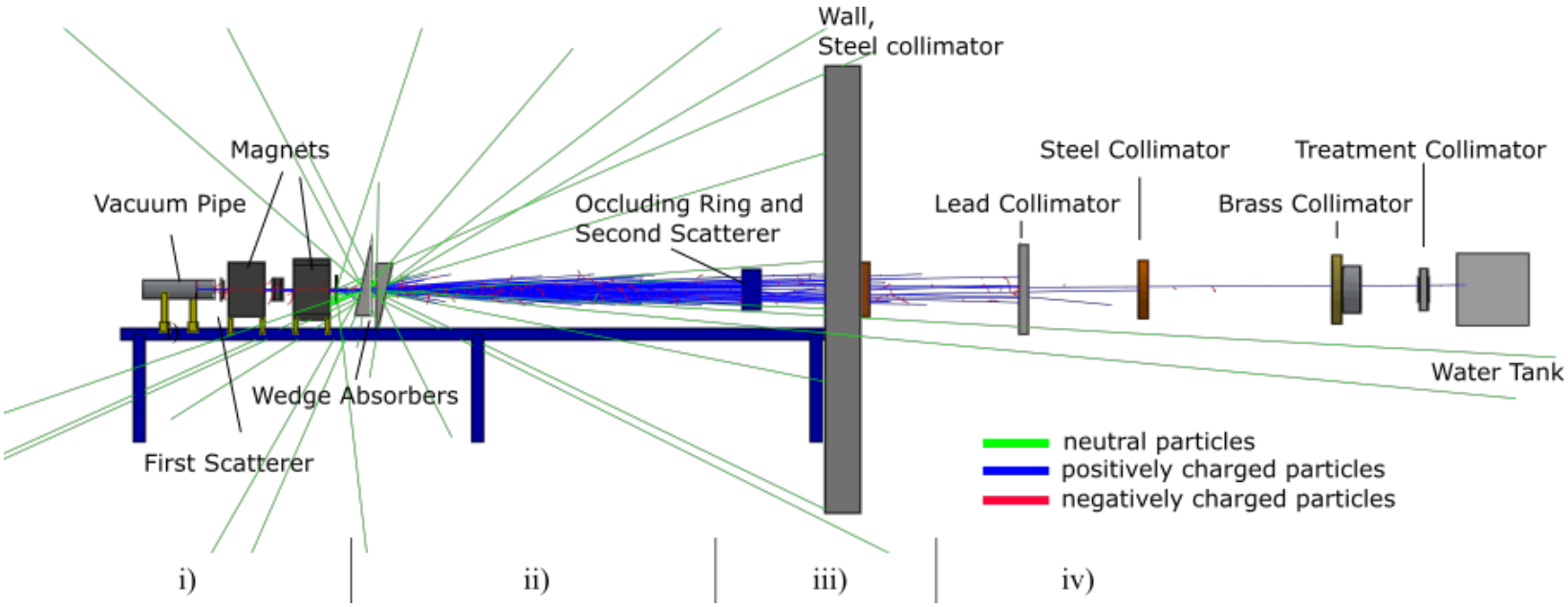

Figure 6.1: Visualisation of the simulation of the iThemba beamline with major components labelled. In this simulation, the wedges were set to give a 52 mm range in water beam at the water tank. Primary protons are shown in blue beginning in the vacuum pipe, the location of the Geant4 general particle source. Secondary electrons are shown in red and neutrons and gammas are shown in green.

6.2.1 iThemba beamline geometry

The proton beamline at iThemba LABS geometry is depicted in figure 6.1, taken from SuSi to provide reference for the following section. The beamline is arranged in a double-scattering configuration, where two thin scattering plates of high-Z material are used to generate flat, broad beam at the patient collimator. The principles of the design are explained in Koehler et al [18].

i The proton beam enters the beamline through a vacuum pipe connected to the cyclotron. We begin modelling the proton beam in this vacuum pipe as a general particle source and define a proton energy distribution. Primary protons are then produced with an energy randomly sampled from this distribution. A reference ionisation chamber acts as the first scatterer immediately at the exit of the vacuum window. Steering magnets then act to focus the beam, whilst the multiwire ionisation chamber monitor constantly monitors the beam position providing feedback to the steering magnets.

ii The range trimmer plates, lead plate and double-wedge energy degraders act as an energy selection and tuning system for the treatment beam. The lead plate is attached to the wedge degraders in a way so that the plate is only in the beam when the wedges are open. The wedges comprise two blocks of graphite mounted back to back on a drive mechanism that allows them to be driven together to provide a variable absorber thickness in order to modify the energy, and therefore the range, of the beam at the final collimator. The drive mechanism is encoded such that the range of the beam is within $\pm$ 0.5 mm of the requested range, provided that the energy of the beam is within tolerance. If the energy of the beam is out of tolerance, adjustments to the range can be made by adding or removing range trimmer plates just upstream of the energy degraders. Each range trimmer plate is made of thiolyte, a paper-based compound, measuring 0.622 mm thick with a RSP of 1.343, constituting a water equivalent thickness of 0.835 mm. Previous work calibrated the vertical wedge position as a function of the delivered range [77].

iii The multilayer Faraday cup and range monitor were inactive during our experiment and acted as collimators. The occluding ring and central stopper constitute components in the double-scattering system. Mounted on the second scatterer, the central stopper removes the central portion of the beam spot and the occluding ring removes protons with a high angular displacement from the central beam axis. The remaining protons are then scattered on the second scatterer to

produce a flat lateral beam profile.

iv Finally, a series of shielding collimators are used to reduce scattered protons and secondary particles and to ensure a sharp penumbra at the edge of the lateral beam profile. The final treatment collimator assembly allows the insertion of a collimator to define the treatment beam size. For the experiments performed at iThemba we used an 85 mm diameter collimator, with the exception of the measurements taken of the relative stopping power of the tissue equivalent materials, where the sample materials were held in place by a 15 mm collimator.

In figure 6.1, a modelled water tank is shown at the end of the system. The water tank is used as a scoring volume. In a scoring volume, a particular property of the simulation is recorded for further analysis. In this case, we aim to replicate Bragg peaks so we score the energy lost per unit length by particles inside the water tank. By binning the data together into steps along the Z-axis, we obtain a Bragg peak.

6.2.2 Preliminary simulation work

One aim of this chapter is to tune the energy of the proton beam in SuSi so that simulated Bragg peaks replicate experimental measurements taken with the water tank, shown previously in chapter 3. The nominal energy of the proton beam entering from the cyclotron is around 201 MeV however we have no exact measurements of the experimental conditions on the day. The two measured Bragg peaks we will use for this work are shown in figure 6.2. These measurements were taken during an experimental visit to iThemba LABS in November 2016. The first Bragg peak, referred to as reference beam 1, was one of the first measurements acquired during the experimental run prior to our work measuring material RSPs. The second Bragg peak, reference beam 2, was taken around 4 hours later after all the samples had been measured. The first Bragg peak was measured with a broad proton beam, where the collimator aperture was 85 mm in diameter. The second Bragg peak measurement used a 15 mm collimator as it was taken immediately after measurements of material RSPs. Two major differences can be seen between the Bragg peaks. The peak to plateau ratio in reference beam 2 is lower than that in reference beam 1. Secondly the range measurement R_{80} on reference beam 2 had increased by 0.6 mm compared to reference beam 1. Whilst it is understood that the energy of beam may vary slightly affecting the measured range, prior to tuning the energy we wanted to replicate the characteristics of these two Bragg peaks and understand whether the use of the collimator affects the measured range of the beam.

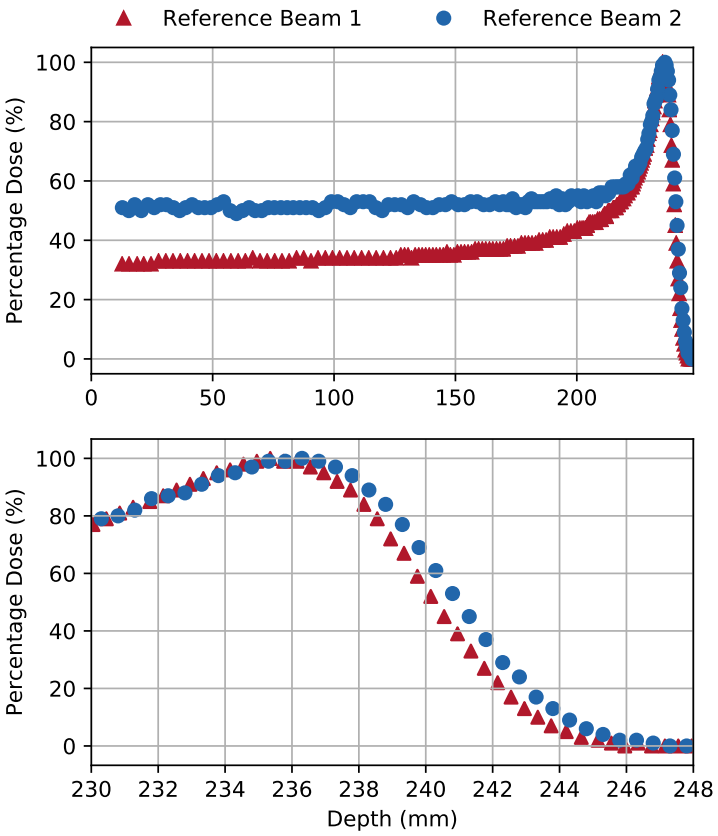

Figure 6.2: The reference Bragg peaks taken with the water tank, as described in chapter 4. Reference beam 2 was taken around 4 hours after reference beam 1. Reference beam 1 was delivered with an 85 mm collimator, whilst reference beam 2 was taken with a 15 mm collimator.

Two simulations were performed of the iThemba beamline, one with a final collimator aperture of 85 mm and one with an aperture of 15 mm. Each simulation was performed with 250 million primary particles, taking around 600 hours of CPU time each. Energy deposition was measured in bins of 0.1 mm length along the beam axis in a central region of the water tank measuring 3 mm high and 1.9 mm wide. This was done to replicate the spatial properties of the ionisation chamber used in the water tank measurements. A cubic spline was fitted to the data and the range R_{80} was found for each peak. The uncertainty on R_{80} was also calculated by considering the RMS residual between the data and the spline fit. In this way, the contribution of noise due to poor statistics in Monte Carlo can be quantified. Secondly, the peak to plateau ratio of the Bragg peaks was also calculated.

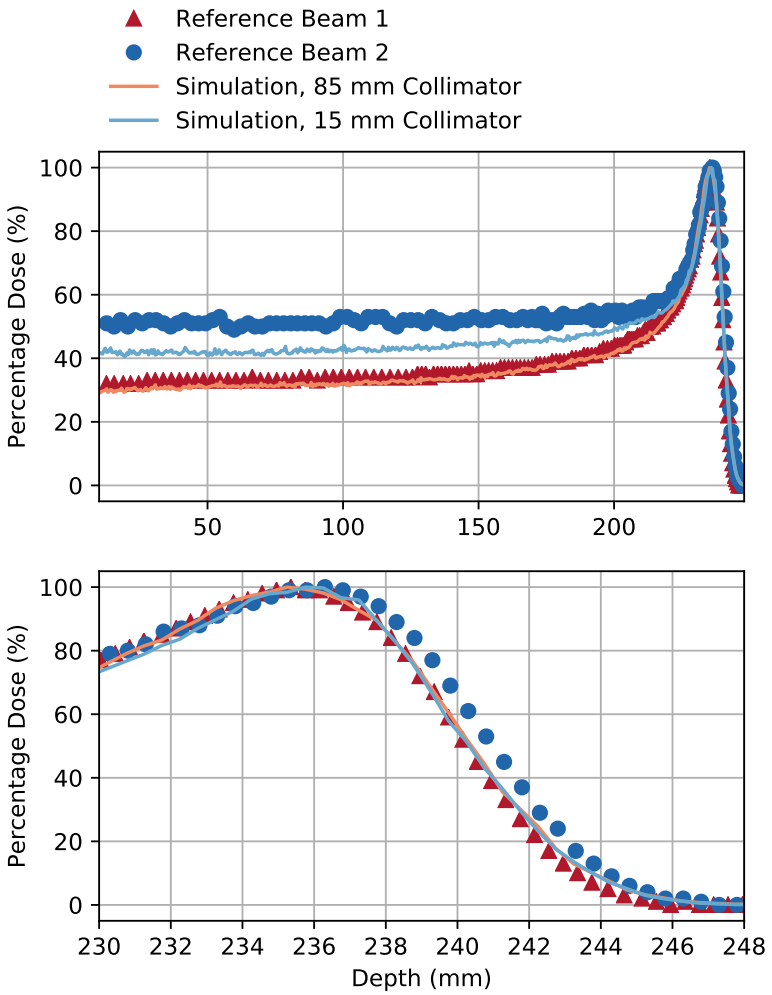

Figure 6.3: The reference Bragg peaks with two simulated depth-dose curves showing the effect of the collimator. Dose was scored in a portion of the water tank the same size as the ionisation chamber used in the experimental measurements.

	Experiment	**Simulation**	
	Peak to Plateau	Peak to Plateau	R_{80} [mm]
Ref . Beam 1 85. mm Coll	3.33	3.24	238.58 ± 0.11
Ref Beam 2 15. mm Coll	1.7	2.47	238.54 ± 0.22

Table 6.1: Peak to plateau ratios and ranges for the two simulated beams shown in figure 6.3, scored using a volume representing an ionisation chamber. Peak to plateau ranges for the experimental measurements are also included.

The two Bragg peaks are shown in figure 6.3. They show good agreement with the reference curves in terms of the peak-to-plateau ratios, shown in table 6.1. Whilst the energy of the simulated beams has not yet been tuned, the energy source in the two simulations is exactly the same so we can determine whether the collimator size affects the measured range in the simulation. The two simulated Bragg peaks ranges agree with each other within error. This suggests that the collimator does not affect the measured range and thus we must consider that between the two reference Bragg peak measurements, the energy of the cyclotron changed slightly. We note that the uncertainty on the beam with the smaller collimator is larger than the beam with the 85 mm collimator.

Both of these simulations were computationally expensive. In order to tune the energy we wish to run a large number of simulations. By improving the statistics of the measured Bragg peak, we could reduce the number of primaries required in the simulation. One method of achieving this is by extending the scoring volume to cover the whole water tank. We ran two more simulations to replicate the reference beam conditions however this time scored the energy deposition in the whole water tank volume. We were able to obtain sufficient statistics with 4 million protons, reducing the CPU time to 10 hours per simulation. The results from this simulation are shown in figure 6.4. TheR_{80}values in each simulation agree within error. The peak to plateau ratio of the 85 mm collimator beam agrees with that from the reference experiment. However, the plateau region in the simulation with the 15 mm collimator does not match with the experiment. The dose in the plateau region dips before rising to the Bragg peak. This can be explained by considering the lateral scatter of the proton beam. Immediately after the collimator there will be a proportion of protons with lower energy than the primary beam. These protons scatter laterally and increase the dose at the front of the water tank. This is not measured in the reference beam because the dose deposited is outside of the measurement volume along the central axis. The peak to plateau ratios and ranges are shown in table 6.2.

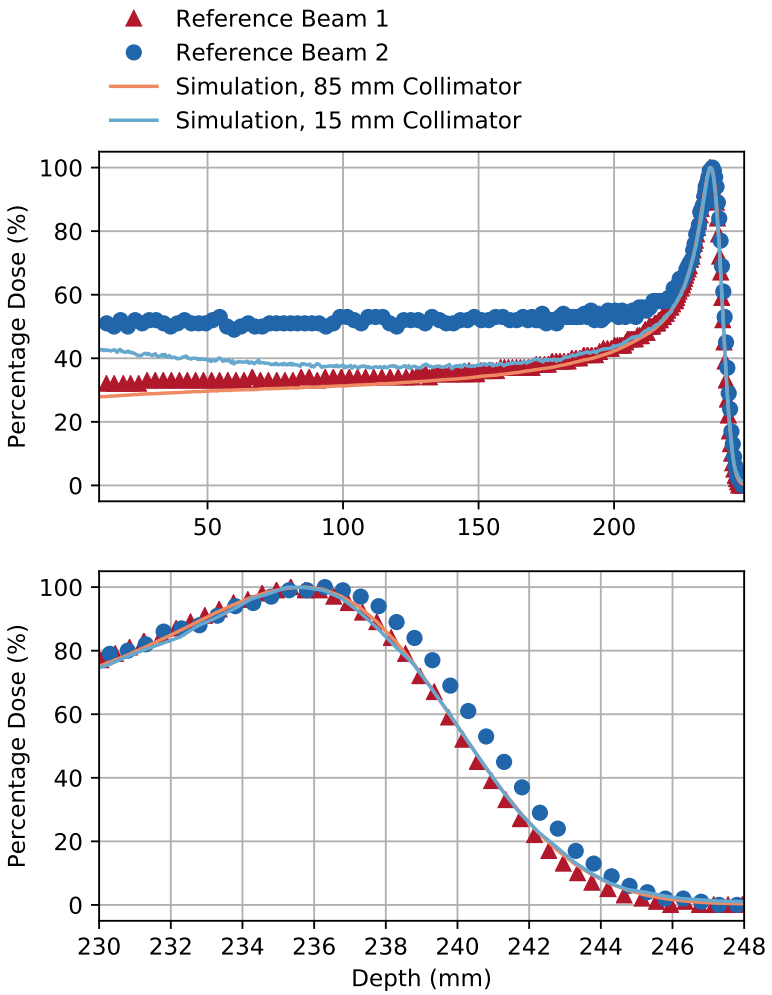

Figure 6.4: The reference Bragg peaks shown with two simulated depth-dose curves where dose was scored in the whole water tank volume.

	Experiment	**Simulation**	
	Peak to Plateau	Peak to Plateau	R_{80}
Ref . Beam 1 85. mm Coll	3.33	3.38	238.54 ± 0.01
Ref Beam 2 15. mm Coll	1.7	2.54	238.45 ± 0.08

Table 6.2: Peak to plateau ratios and ranges for the two simulated beams shown in figure 6.4, scored using the whole water tank. Peak to plateau ranges for the experimental measurements are also included.

Now we can consider the four results together; each simulation comprises the same primary particle source and geometry with the exception of the final collimator and scoring volume size. The two depth-dose curves simulated with the 85 mm collimator show good agreement with each other, suggesting that for these Bragg peaks the scoring volume size has little effect on the measured depth-dose curve. The peak-to-plateau ratio, evaluated by comparing the ratio of the depth-dose curve at its maximum point and at 50 mm depth in water is 3.38 when measuring using the whole water tank and 3.24 when measuring using the small scoring volume. The peak to plateau ratio measured in the water tank data with the 85 mm collimator is 3.33.

The measurement of the depth-dose curves using the 15 mm collimator in the simulation appear to be influenced more significantly by the choice of the scoring volume. The plateau region of the simulated curve with the larger scoring volume has a decreasing slope before rising to the Bragg peak, unlike the measurement taken in the water tank. Evaluating the peak to plateau ratio at 50 mm depth however doesn't describe this effect very well. The peak to plateau ratios for the large and small simulated curves are 2.54 and 2.47 respectively. The measured depth-dose curve has a peak to plateau ratio of 1.7. This suggests that there is a larger, lower energy component in the proton beam in the measurement that is not being accounted for in the simulation when using the smaller collimator aperture.

We can conclude that the detector geometry has an effect on characteristics of the beam measurement, however by using the full water tank as a scoring volume the required computational time is reduced by a factor of 50. Therefore, we turn our attention to the distal edge of the Bragg peak. The distal edge of the Bragg peak is often used to characterise or describe the desired beam in proton therapy. The iThemba nomenclature uses the point at which the depth-dose curve falls to 50% of its maximum to describe the range of their beam. This appears to be purely historical. Other centres prefer to refer the range at which the curve falls to 90%. The range at which the dose falls to 80% is also used widely and approximately corresponds to the median range of a distribution of protons, or the point at which the proton fluence falls to 50% of its maximum. Range measurements at R_{80} of the four simulated depth-dose curves are compared to see if the collimator size or scoring volume size has an effect on the measured range. These range measurements are shown in table 6.3.

Each range measurement has an associated uncertainty that is dependent on the noise in the simulation. Table 6.3 shows that the reduced detector size contributes to this uncertainty. All of the simulations agreed on the proton range within

R_{80} (mm)	15 mm Collimator	85 mm collimator	Difference
Detector Volume	238.54 ± 0.22	238.58 ± 0.11	0.04 ± 0.25
Whole Volume	238.45 ± 0.08	238.54 ± 0.01	0.09 ± 0.08
Difference	0.09 ± 0.23	0.04 ± 0.11	

Table 6.3: Simulated proton ranges in water measured using the whole water tank volume and a subset of the volume corresponding to the size of the ionisation chamber, using a large and small collimator aperture.

error. The maximum difference in the range R_{80} between all of the simulations was 0.09 mm. Therefore, we can continue our Monte Carlo work by scoring in the entire water tank volume, provided that we focus our analysis on the distal edge of the Bragg peak.

6.3 Tuning of the energy source

6.3.1 Introduction

Simulated primary protons are generated at the entrance of the vacuum pipe in the iThemba Beamline using a Geant4 general particle source. The general particle source class allows the user to generate a beam or emittance source with a specified shape and size, spatial distribution and divergence angle. The energy distribution of the source may also be specified. In the current application, primary particles are each assigned a random energy sampled from a given energy distribution. This is done to model the proton beam generated by the cyclotron as it arrives at the start of the beamline. Previous simulation of the iThemba beamline specified a Gaussian energy distribution with a mean energy of 201.36 MeV [77]. With the revised I-value of water amongst other updates to the beamline model, we tune the revised simulation to obtain range measurements that match our measured Bragg peaks. From this we can determine the apparent energy drift in the cyclotron as well as updating the general particle source for use in further simulation work.

Varying the energy of the source changes the range of the depth-dose curve, whilst modifying the standard deviation affects the width of the Bragg peak and therefore gradient of the distal edge. For a beam with a Gaussian energy distribution, the range in water at 80% of the maximum dose is approximately

$$R_{80}[mm] = 0.022E^{1.77}. \tag{6.1}$$

The exact values of the parameters vary between literature sources as they

are derived from a fit to ICRU data and are dependent on the limits used for the fit [82, 15, 7].

The distal falloff, defined as the range at which the dose falls to 20% of the maximum minus R_{80} may also be approximated. The following equation is provided by Gottschalk [7] and corresponds to the minimum expected peak width as a function of the energy spread of the beam and a range straggling factor, where the energy spectrum is broadened as a function of the range:

$$R_{20} - R_{80} = 1.3 \times (\sigma_{En}^2 + \sigma_{straggling}^2) \tag{6.2}$$

where σ_{En} is the standard deviation of the energy spectrum and $\sigma_{straggling}$ is a range straggling factor defines as approximately 0.0012 x Range.

These two equations are based on the assumption that R_{80} is independent of the energy spread, and that the spread is Gaussian at the point of delivery. However in the iThemba beamline, the combination of scatterers and the occluding ring introduce further range straggling so that the distribution at the final collimator is non-Gaussian. Furthermore an initial study into the accuracy of these equations using a Geant4 simulation of a Gaussian beam into water showed that R_{80} varied by around 1% for beams with energies around 80 MeV when varying the standard deviation from 1.0 to 5.0 MeV. Therefore, rather than relying on a single defined measurement point to validate the initial energy spread of the beam, we chose to validate our simulation against the whole distal edge of the Bragg peak.

6.3.2 Method

The energy spectrum of the general particle source is specified in a macro file that is used to drive the Monte Carlo simulation. Initially macro files were defined specifying Gaussian energy distributions with a mean energy of 201.20 MeV to 201.80 MeV in steps of 0.05 MeV, with standard deviations ranging from 0.2 MeV to 0.8 MeV in steps of 0.05 MeV. Each simulation was run with 10 million primary particles. These initial simulations were used to inform a region that could be looked at with higher precision.

Results from each simulation were compared against water tank measurement of a pristine Bragg peak with a nominal R_{50} of 240 mm by performing a chi-square test. The water tank measurements chosen for this were the first and second reference beams taken during an experiment at iThemba LABS in November 2016 and are shown in figure 6.2. As discussed previously, the measured range of these beams differed by 0.6 mm. Therefore, validating the input energy for each

Bragg peak allows us to estimate the energy drift of the beam at the entrance of the beamline.

In the chi-square method, the Bragg peak produced by the Monte Carlo simulation is treated as a model, and the fit of the data to the model is evaluated. The chi-square value was evaluated from the peak to the point at which the dose drops to 10% of the maximum value on the distal edge. This was done to avoid the choice of detector size and collimator influencing the result. A Savitzky-Golay filter was used to calculate uncertainties on the water tank data by subtracting the filtered data away from the raw data. Through this method, a heteroscedastic uncertainty could be applied, meaning each individual data point had its own uncertainty value associated with it. The depth-dose curves from the simulation and the water tanks were scaled such that their peak value was equal to 100, allowing a direct comparison between the curves. A chi-square statistic was then calculated for each data point using

$$\chi^2 = \sum_z \frac{D_{meas,z} - D_{sim,z}}{\alpha^2_{meas,z}}, \tag{6.3}$$

where $D_{meas,i}$ is the measurement of dose in the water tank at depth z in the water tank,$D_{sim,i}$ is the simulated dose at the same depth and $\alpha_{meas,z}$ is the uncertainty in the measured dose, calculated from residuals to the filtered dose measurement. The simulation corresponding to the minimum chi-square statistic is then treated as the correct result.

Providing that the model is a good fit, the uncertainties $\alpha_{meas,z}$ can be scaled based on the minimum chi-square statistic. If the model correctly describes the dataset, the chi-square value should be equal to the number of independent variables in the test. The number of independent variables in the test ν is the number of data points minus the number of variables in the model. If the reduced chi-square statistic χ^2/ν is close to 1, a scaling factor can be calculated for the uncertainty $\alpha_{meas,z}$ in order to set $\chi^2 = \nu$. This scaling factor is defined as $S = \sqrt{\frac{\chi^2}{\nu}}$. The uncertainty on the mean and standard deviation of the energy of the general particle source are then determined by calculating the standard deviation of the chi-square value, where $\sigma_{\chi^2} = \sqrt{2\nu}$.

6.3.3 Results

Results from the initial simulations found minimum chi-square values for inputs of 201.25 MeV with σ of 0.35 MeV for reference beam 1 and 201.55 MeV with a σ of 0.55 MeV for reference beam 2. The water tank data set and the simulated results

are shown in figure 6.5. These simulations were performed with coarse energy intervals and as such no neighbouring values had chi-square values within one standard deviation of the minimum chi-square values, so we can define the uncertainty on the energy and standard deviations as $+/-0.05MeV$. This uncertainty is insignificant compared to the apparent energy drift of the cyclotron. However, we continued to perform more simulations to look at the uncertainty on the input energy of the second reference beam in order to define the uncertainties there.

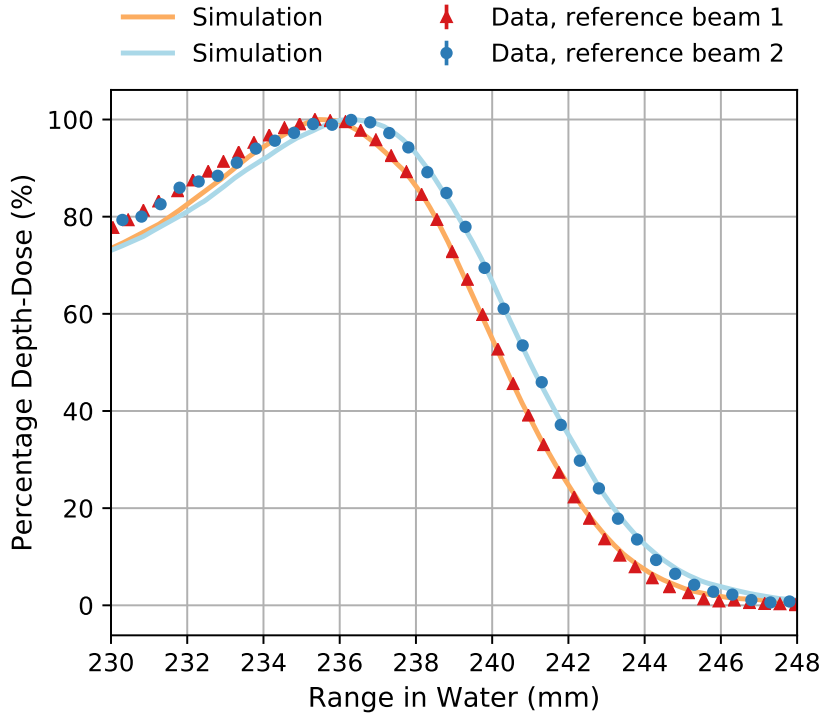

Figure 6.5: Data from the two reference Bragg peaks with simulations overlaid. The simulation results correspond to the datasets providing a minimum chi-square value. The gps energy spectrum of both beams was Gaussian. The mean energy of beam 1 was 201.25 MeV with a σ of 0.35 MeV and the mean energy for reference beam 2 was 201.55 MeV with a σ of 0.55 MeV.

The motivation for looking at the uncertainties on the energy input for the second reference measurement were so that a range uncertainty on the simulation could be established as a function of the input energy. This range uncertainty was to be used in to determine the I-value of polyethylene, with the aim of reducing the I-value uncertainties in the published literature [57]. A water tank measurement of the RSP of polyethylene was taken immediately prior to this reference beam measurement, so we can assume that the energy change between these two mea-

surements was negligible. To ensure that our calculated uncertainty in the I-value of polyethylene is lower than that offered by the literature, we want to ensure that we have accounted for the uncertainty in our general particle source.

Fine Tuning

Further simulations were then performed between 201.45 and 201.65 MeV with steps of 0.01 MeV with the standard deviation varying between 0.40 MeV and 0.60 MeV in steps of 0.02 MeV. Each was performed with 600 million primaries. By finding the maximum and minimum energies and standard deviations that provide a chi-square result within 1 standard deviation of the minimum value we can determine our uncertainties [60]. In this case, we determined that the mean and standard deviation of the Gaussian energy spread of the general particle source should be 201.53 $\pm$ 0.02 MeV and 0.48 MeV $\pm$ 0.08 MeV respectively. These results are shown in 6.6.

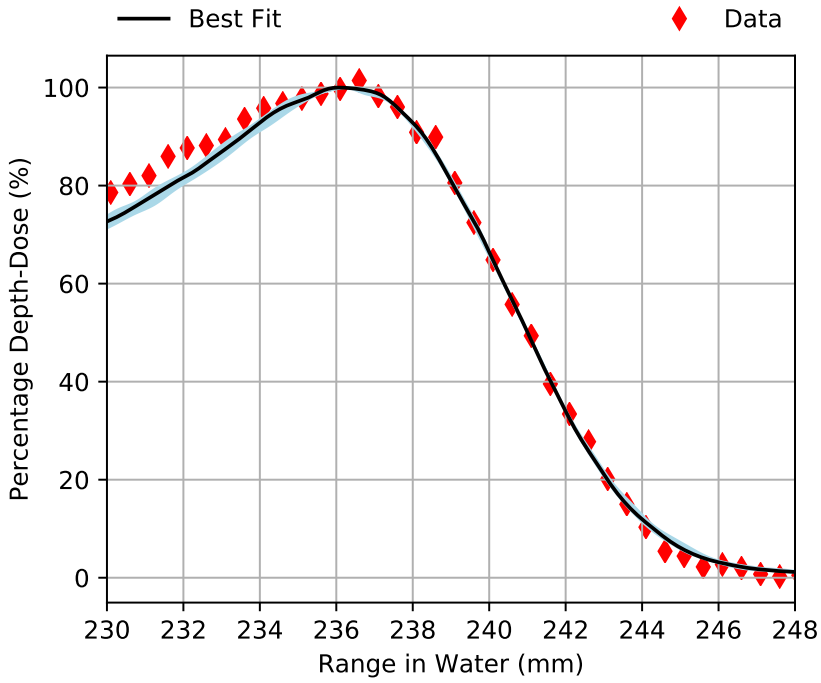

Figure 6.6: Optimal simulation result for reference beam 2 shown, with 1σ uncertainty highlighted

6.4 Validation of Material I-values

As discussed extensively in the literature [83, 15, 11], uncertainties in the I-values published in the literature are a major contributor to proton range uncertainty. The estimates of Paganetti [15] et al determined that on average, the uncertainty in published I-values contribute a range uncertainty of upto 1.5%. More recent work by has sought to reduce this uncertainty to between 0.3 and 0.5 % of the range of the beam [16] however the currently accepted

When the elements are combined into mixtures or compounds, their respective I-values are determined either through experimental measurement or through use of the Bragg additivity rule. One such method, also used to determine the I-value of water, is to perform range measurements experimentally and compare them against Monte Carlo simulation, where the I-value of the material of interest can be defined by the user [84]. By minimising the range difference between the simulation and measurement, as a function of the I-value, the I-value of the material can be found.

In the following work, we want to run a Monte Carlo simulation of a proton dose distribution inside a phantom, using geometries acquired from x-ray CT and proton CT imaging. In order to compare these simulations to experiment, we need to validate range of the incoming proton beam. This is done by simulating the experiment with the real geometry and comparing the simulated beam against the film measurement. The phantom used was constructed using high-density polyethylene (HDPE). The quoted I-value of HDPE in the literature is 57.4 ± 8 eV. This corresponds to an uncertainty in the relative stopping power of HDPE of about 3% for a 100 MeV proton beam. For a 15 mm sample, this corresponds to an uncertainty of over 0.4 mm in the range in water of the measurement, and in the following chapter would correspond to a range uncertainty of around 1.5 mm for a beam with an approximate range of 50 mm.

Using the energy and standard deviation that we calculated in the previous section, a new simulation was initiated. In the simulation, a cylindrical sample of polyethylene was inserted into 15 mm diameter aperture in the treatment collimator, so that the SuSi simulation replicated the experiment described in chapter 4. The polyethylene sample has a length of 14.88 mm and a mass density of 0.94 g/cm^3, and these values were used in the simulation.

A new user option was defined in the simulation so that the I-value of the polyethylene insert could be defined. The simulation was performed using 17 different I-value settings, from 49.4 eV to 64.4 eV in steps of 1 eV. Each simulation

was performed with 850 million primary protons, scoring the energy deposition in the whole water tank. A subset of the simulated depth-dose curves are shown in figure 6.7, alongside the experimental measurement. The range at 80% on the Bragg peak distal edge, R_{80} was used to determine the best fit to the data. The range error, calculated by subtracting the simulated R_{80} from R_{80} measured in the water tank was then fitted as a function of the I-value of polyethylene by rearranging the Bethe-Bloch equation:

$$\Delta R = A\rho_{e,rel} \times \frac{B - \ln I_{polyethylene}}{B - \ln I_{water}} \tag{6.4}$$

where $B = \ln \frac{2m_e c^2 \beta^2}{\beta^2} - \beta^2$ and is a coefficient accounting for the constants in the Bethe-Bloch equation and the energy of the proton beam.

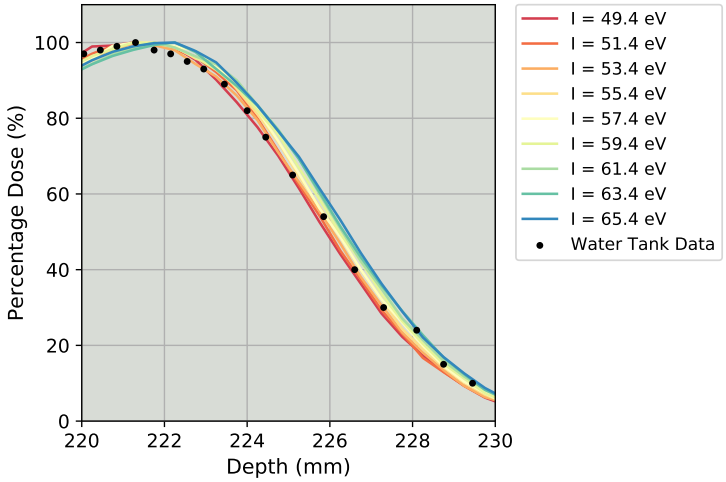

Figure 6.7: Simulated Bragg peaks incident on a sample of polyethylene. As the I-value reduces, the proton range increases. Error bars were too small to be visible on the water tank data.

The covariance of the fitted parameters was used to determine the 95% confidence limits, shown in figure 6.8. From the fit, we are able to determine the I-value of the HDPE sample used in this experiment as 50.8 ± 1 eV. This value is in agreement with the accepted value of 57.4 ± 8 eV however with significantly reduced uncertainties. It is noted that the uncertainties defined by the covariance matrix are lower than the random error in the data. We would expect to see a reduction in the random error by increasing the number of simulated protons however the process is already computationally demanding. We intend to apply this method to evaluate the I-values of tissue equivalent materials introduced in chapter 4. In future work,

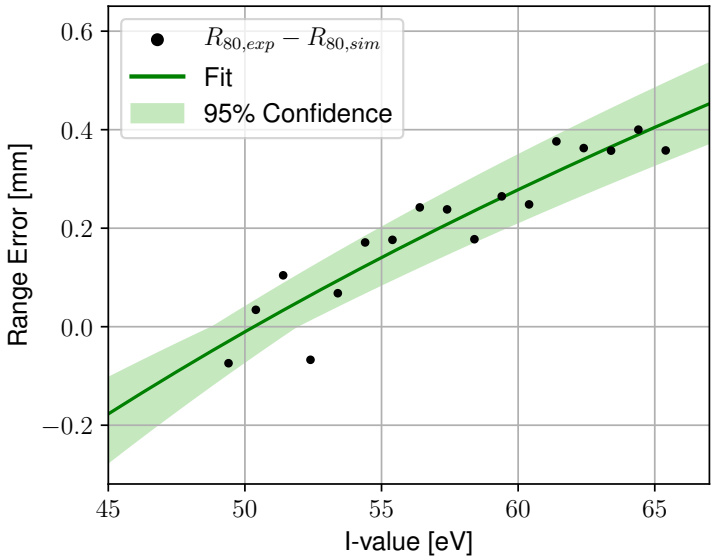

Figure 6.8: Results from a Monte Carlo simulation showing the range difference at R_{80} between a water tank measurement and a simulation of a nominal 240 mm range proton beam incident on a 15 mm sample of polyethylene. In the simulation, the I-value of the polyethylene sample was adjusted to tune the simulation in order to reduce the error and redefine the I-value of polyethylene.

it would be preferable to take water tank measurements using larger samples as this would increase the relative range error as a function of the I-value and thus reduce the need for such high-precision computation.

6.5 Conclusions

The performance of Monte Carlo simulation of the iThemba LABS proton beamline was validated against experimental measurement. The energy of the proton source in the simulation was tuned by performing a chi-square test and uncertainties on the input were defined. Following this work we used the simulation to calculate the I-value of polyethylene. This method provided a result with lower uncertainties than the current accepted value. We will use this simulation to calculate proton dose distributions on image data from proton and x-ray CT.

Chapter 7

Film Phantom CT: Comparison of x-ray CT and proton CT

7.1 Introduction

In this final experimental chapter, we introduce a dosimetric phantom designed to be imaged with the PRaVDA proton CT and measure the range of an incident proton beam. The motivation behind this design is to test the applicability of proton CT images in treatment planning. The phantom was also imaged with x-ray CT and by comparing dose distributions calculated using Monte Carlo on each image set, we can demonstrate the difference that the imaging modality can make to the calculated proton range for the same proton beam. The dosimetric phantom contains a portion of Gafchromic EBT-3 film oriented in the plane of the beam so that a 2D dose distribution could be recorded. This experiment combines elements of all the prior work in this thesis to demonstrate the potential use of proton CT in treatment planning.

7.2 Film phantom design

The film phantom was constructed by University Hospital Coventry and Warwickshire and comprises a cylinder measuring 75 mm in diameter manufactured from high-density polyethylene (HDPE). The phantom is constructed from two halves measuring 37.5 mm in height. In the lower half, there are two 15 mm diameter recesses designed to hold rods of tissue equivalent materials, as used in chapter 4 to measure the RSPs. Rods of LN10 (lung equivalent) and SB5 (cortical bone equivalent) were chosen to maximise the dynamic range of the dosimetric measurement.

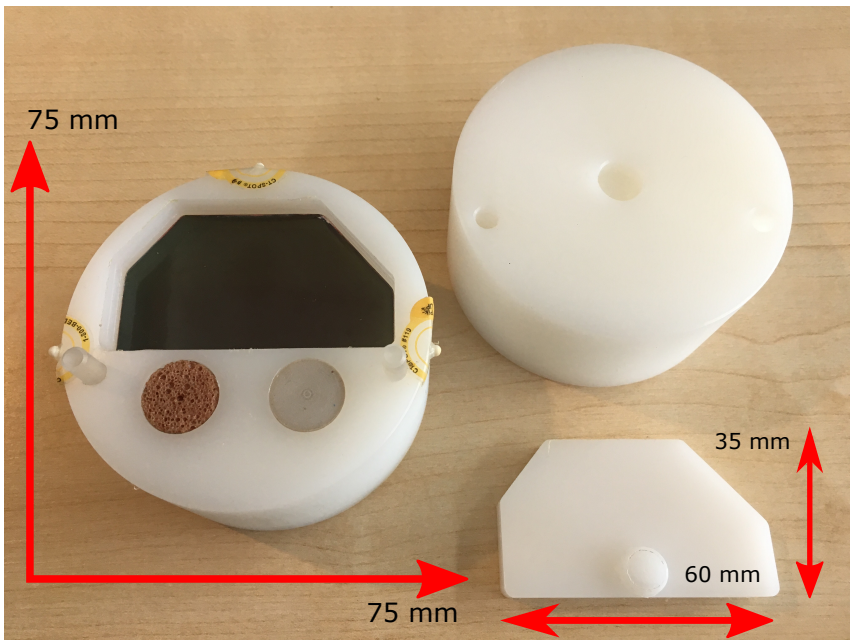

Figure 7.1: Photograph of the film phantom in three parts. The top and bottom halves are held together with locating pins and a plug holds the film in place.

The measurement was performed using a piece of Gafchromic EBT-3 film located in a recess behind the two inserts. A photograph of the phantom is shown in figure 7.1.

The film was arranged so that the beam axis is along the plane of the film. In this orientation, the Bragg peak can be seen along the film and a depth-dose curve can be extracted. A plug compresses the film to minimise air gaps around the outside. The EBT-3 film was cut using a computer-controlled vinyl cutter at the Queen Elizabeth Hospital, Birmingham. This allowed precise and highly reproducible cutting. The size of the film cutouts was optimised by cutting prototypes and adjusting the size in 50 µm steps in both directions so that the film sat flat in the cavity with no lateral movement. The shape was chosen to be asymmetric so that the film could only fit in one orientation, minimising the chances of a non-uniform film response based on the film orientation [85]. The film recess was tilted with a 1 degree angle to reduce the effect on the measurement of air gaps around the film [86].

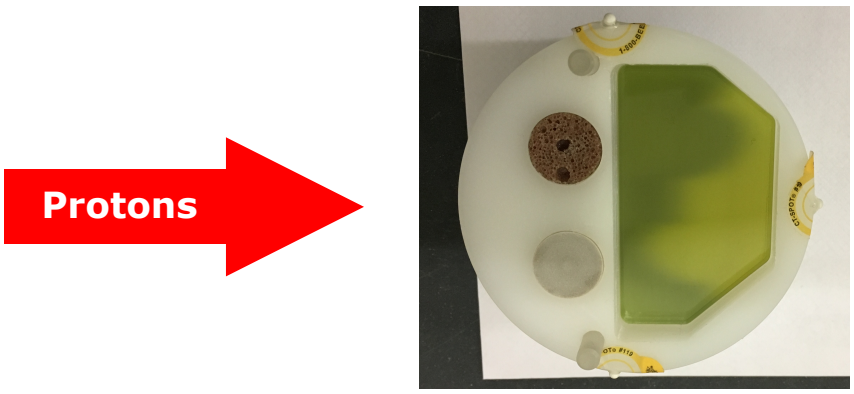

Figure 7.2: Photograph of the film phantom after irradiation with the 45 mm range beam.

7.3 Irradiation at iThemba LABS

Prior to the imaging and simulation work, the phantom was irradiated with a proton beam at iThemba LABS. The phantom was placed at the isocentre of the beamline at iThemba LABS, such that the beam was incident perpendicular to the front edge of the film. A collimator with an aperture of 85 mm was used. The beam current was of the order of 10 nA and the phantom was irradiated for 4 minutes, delivering approximately 4 Gy at the Bragg peak. Two irradiations were performed with the range degrader wedges adjusted inbetween the measurements, such that two proton beams with different ranges were measured. The film was replaced between the two measurements. The two beams had nominal ranges of 45 mm and 52 mm in water. These values were chosen so that we could ensure that the protons stopped inside the EBT-3 film at 3 measurement points: behind the LN10 inhomogeneity, behind the SB5 inhomogeneity and through the central portion of HDPE. The relatively broad range of stopping powers between the LN10 and SB5 samples meant that the two measurements with different ranges were needed. A photograph showing film phantom after irradiation with the 45 mm range beam is shown in figure 7.2.

7.3.1 Film Dose Response Calibration

Two calibrations were needed to determine the dose response of the film when measuring the proton Bragg peak. The first calibration provides the dose as a function of the optical density of the film. The second calibration corrects for underreponse when measuring proton Bragg peaks using radiochromic film.

EBT-3 film is a radiochromic film that changes its optical density in response to ionising radiation. The change in optical density arises from the polymerisation

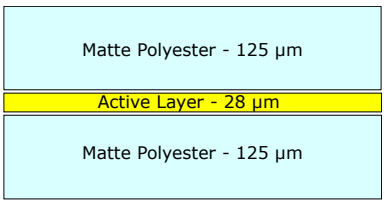

Figure 7.3: Schematic of Gafchromic EBT-3 film, redrawn from [85]

of dye monomers in an active layer of the film. A schematic of the layer structure is shown in figure 7.3. EBT-3 is approximately 270 µm thick and is designed to be water-equivalent. The optical absorption induced by polymerisation of the monomers generates a peak at 622 nm, showing the largest change in optical density in the red spectrum of visible light [85]. This induces a colour change to the naked eye and the film turns from yellow to blue in appearance. The under-response when measuring Bragg peaks occurs due to local polymerisation sites saturating in the presence of high LET protons [87, 88, 89].

Dose Response

The calibration of the dose response as a function of the optical density of the film was performed by irradiating pieces of EBT-3 film to known doses at the MC40 Cyclotron at the University of Birmingham. A 28 MeV proton beam was used. Pieces of EBT-3 film were arranged perpendicular to the beam axis and the dose delivered to the film was calculated from the charge measured in a Markus ionisation chamber located behind the film. The film samples for calibration were from the same sheet used in the irradiations at iThemba LABS. The calibration was performed from 0.2 Gy to 20 Gy, covering the dynamic range of EBT-3 film.

The film was scanned at Queen Elizabeth Hospital, Birmingham 14 days after irradiation using an Epson Perfection V700 scanner used for routine film dosimetry therefore we can assume that any non-uniformity in the scanner response is negligible. The image was scanned at 96 dpi and the red channel was extracted from the rgb image for use in the calibration. The pixel values were extracted using ImageJ and the net change in optical density was calculated for each dose point. This net change was then fitted against the dose using the function

$$\text{Dose [Gy]} = A \times \text{OD} + (B \times \text{OD}^C), \tag{7.1}$$

where OD is the optical density of the film. The resulting values for A, B and C were 8.13, 185.15 and 5.45 respectively. The conversion curve is shown in

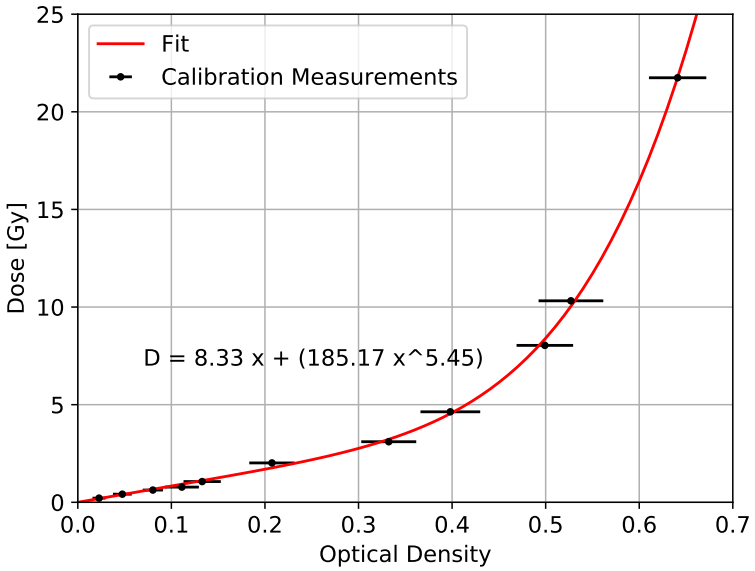

Figure 7.4: Conversion curve to obtain dose from measured optical density in EBT-3 film.

figure 7.4. The standard deviation on the optical density measurement is shown as an error bar.

Bragg Peak Correction

Correcting for the EBT-3 film under-response at the Bragg peak is a particular challenge for the following work. From the literature, two methods were considered. The first method, proposed by Zhao et al for EBT film in a film orientation parallel to the beam axis, involves multiplying the dose measured in the film with a third-order polynomial [86]. EBT is a different model of film to EBT-3 with a different layer structure. The polynomial coefficients are derived empirically by fitting the film measurements to those taken with an ionisation chamber. Zhao et al recommend applying the correction to EBT film measurements of the beam with an energy above 100 MeV.

The second method, described by Fiorini et al, proposes a known correction factor as a function of the mean proton energy at the Bragg peak [88]. The authors suggest that the correction factor can be extended to cover all proton energies and the factor is calculated for EBT-2 and EBT-3. To determine the mean energy of the proton at a given measurement point for the calibration, a Monte Carlo simulation is used. It was decided that whilst the Fiorini method may be more specific to EBT-3

film the inhomogeneities in the film phantom make this method impracticable to apply to our film phantom measurements.

In our calibration we calculate our own correction factors for the polynomial fit of Zhao et al for the two beams. This is done by fitting a measurement of the dose in film along the central axis of the film phantom to Monte Carlo model of the same film phantom in the PRaVDASuperSimulation (SuSi), using the beam parameters and polyethylene I-value found in the previous chapter. In the simulation, the wedges were set to provide a beam with nominally 45 mm range-in-water and 52 mm range-in-water, matching the experimental set up of the iThemba irradiations. Depth-dose curves are extracted for a central portion of the phantom, measuring 1 mm wide.

A 1mm wide region of the EBT-3 film is used to measure the Bragg peak experimentally. The film measurement is scaled to a percentage depth-dose curve and is normalised to the simulated Bragg peak in the plateau region, where the film does not under-respond, such that the first point in the film measurement corresponds to the same percentage dose as in the simulation. The peak height in the uncorrected EBT-3 film does not match that of the simulation. A least-squares fit of the film data to the simulated Bragg peak yields the 3rd order polynomial correction

$$\mathrm{PDD}_{corrected} = \alpha \mathrm{PDD}_{film} + \beta \mathrm{PDD}^2_{film} + \gamma \mathrm{PDD}^3_{film} + \delta \tag{7.2}$$

where $\alpha = 7.21 \times 10^{-3}, \beta = 1.17 \times 10^{-4}, \gamma = -8.64 \times 10^{-7}, \delta = 5.14 \times 10^{-3}$ for the 45 mm range beam and $\alpha = 6.11 \times 10^{-3}, \beta = 2.38 \times 10^{-5}, \gamma = 7.61 \times 10^{-7}, \delta = -1.38 \times 10^{-3}$ for the 52 mm range beam. The uncorrected and corrected film Bragg peaks are shown in figures 7.5 and 7.6 along with the simulated depth-dose curves.

Range measurements on each peak were then calculated, by considering the depth at which the dose falls to 80% and 50% of the dose maximum on each curve. The range measurements for the simulation, uncorrected film and corrected film profile are shown in table 7.1 . The relative stopping power of polyethylene is very close to 1 therefore we can expect to see R_{50} measurements close to 45 mm. The simulation performs as expected and we consider this our truth value to which we compare the film measurements. The corrected film measurement is more accurate at R_{80} than the uncorrected film measurement when compared to the simulation which is to be expected as we attempted to fit the data to the simulation result. We opted to continue to use the Zhao correction in our film analysis in the next section, however we would consider the Fiorini correction in further work.

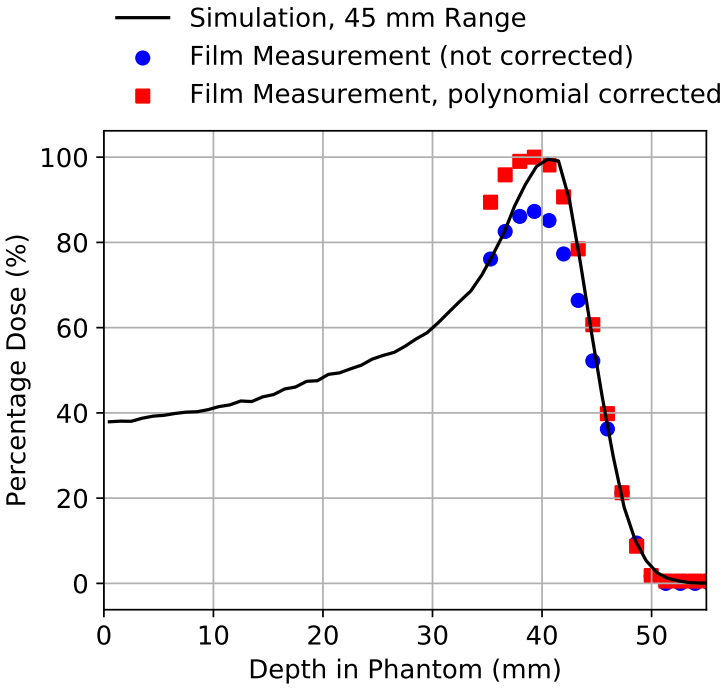

Figure 7.5: Uncorrected and corrected percentage depth-dose curves for the film phantom recorded in EBT-3 film, compared with Monte Carlo simulation. Nominal range is 45 mm.

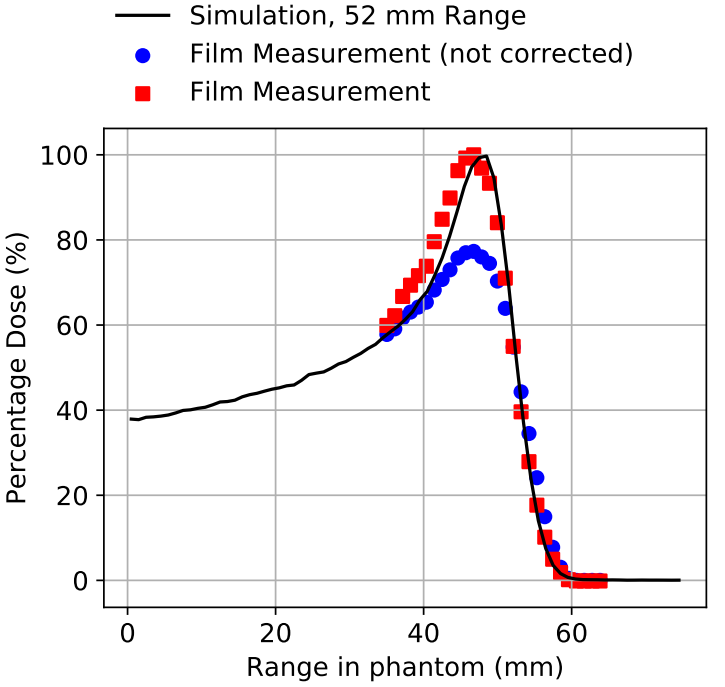

Figure 7.6: Uncorrected and corrected percentage depth-dose curves for the film phantom recorded in EBT-3 film, compared with Monte Carlo simulation. Nominal range is 52 mm.

		R_{80} **(mm)**	R_{50} **(mm)**
45 mm	**Simulation**	43.2	45.1
Nominal	**Uncorrected film**	42.8	45.4
Range	**Corrected film**	43.1	45.3
52mm	**Simulation**	50.7	52.7
Nominal	**Uncorrected film**	51.3	53.8
Range	**Corrected film**	50.3	52.4

Table 7.1: Measured ranges in the polyethylene phantom in EBT-3 film and simulated depth-dose curves. Note that the uncorrected R_{50} measurement in Gafchromic film was slightly higher than expected. The uncertainty on the nominal range of the beam is ± 0.5 mm due to tolerances on the wedge position. for this reason the simulation range was increased to nominally 52.5 mm to match the film. However we continue to refer to the beam as 52 mm in range as this is consistent with the nominal range in the experiment.

7.4 Proton CT and X-ray CT Image Comparison

Proton CT and X-ray CT images of the film phantom were acquired. A slice from each image is shown in figure 7.7. The proton CT scan of the film phantom was completed in November 2016 at iThemba LABS with the same set up as described in chapter 6. A cylindrical range compensator was used to ensure that protons stopped in the range telescope. Data was acquired from the phantom at 90 angles, using steps of 2 degrees and the image was reconstructed using approximately 2 million protons per angle using the non-linear path backproject-then-filter algorithm.

The x-ray CT scan was performed at University Hospitals Coventry and Warwickshire using a modified radical brain protocol. The phantom was scanned inside a 20 cm diameter cylindrical water chamber in order to reduce the effect of beam hardening artefacts on the quantitative accuracy of the Hounsfield Unit (HU) measurements. The HU measurements were converted to RSP using the conversion curve defined in chapter 4 and the water chamber was removed in post-processing by applying a binary mask to a 75 mm circular region centred on the phantom. As a result of the mask, aliasing artefacts occur at the edge of the phantom.

The proton CT image here appears to be affected by noise more significantly than the proton scan of the Bauble phantom shown in a previous chapter. This can be explained because the number of protons used here in the reconstruction is much lower. It is also noticeable there are no significant streak artefacts across the image, as seen in the Bauble phantom. That is because we do not expect any protons to escape the rear of the range telescope. 1D profiles of the x-ray CT derived stopping power map and the proton CT scan are shown in figure 7.8. These profiles were

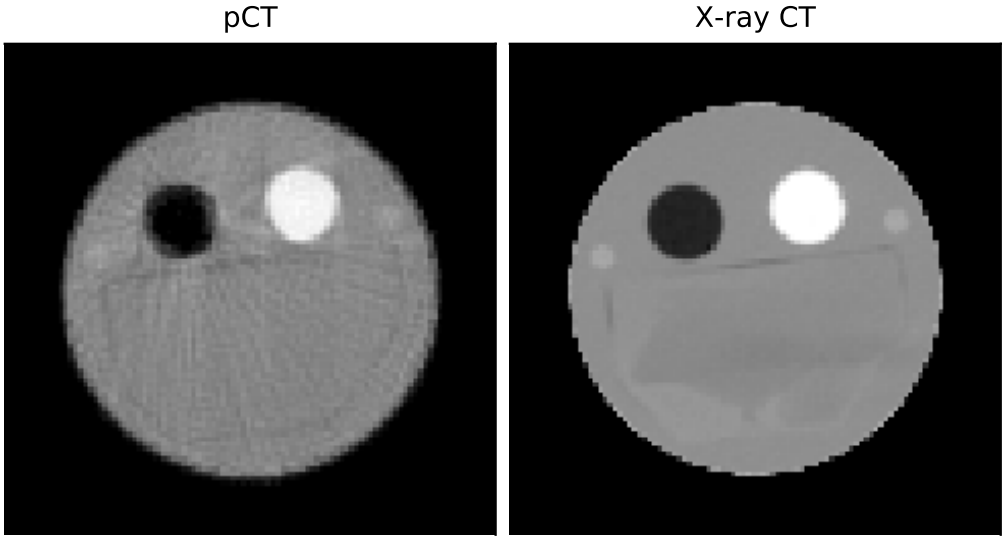

Figure 7.7: Proton CT and x-ray CT images from the film phantom. The aliased edges on the x-ray CT are from cropping the image to remove the background water chamber.

taken across the phantom through the two insert materials. The stopping powers of the materials as measured by the water tank are also overlaid.

The stopping power of the SB5 cortical bone insert is overestimated by x-ray CT. This is consistent with the result observed in the Bauble phantom and can be explained by the inability of the x-ray CT conversion curve to cope with the specific properties of the SB5 insert. Otherwise, the performance of the x-ray CT imaging is relatively good.

The proton CT scan reconstructs the stopping power of the SB5 insert accurately, however the quantitative RSP value of polyethylene is systematically underestimated consistently across the phantom by around 7.5%. The RSP of LN10 is also underestimated in this dataset. The reconstructed RSP of LN10 in this dataset is lower than that reported in the proton CT scan of the Bauble phantom, however this was not investigated further.

7.5 Simulated Dose Distributions

This final piece of work considers the use of proton CT imaging for dose calculation. The proton CT image and x-ray CT dataset for the film phantom were used to construct a voxelised phantom geometry in Geant4 for use with the SuSi. Two proton beams were simulated incident on the phantom geometries to replicate the

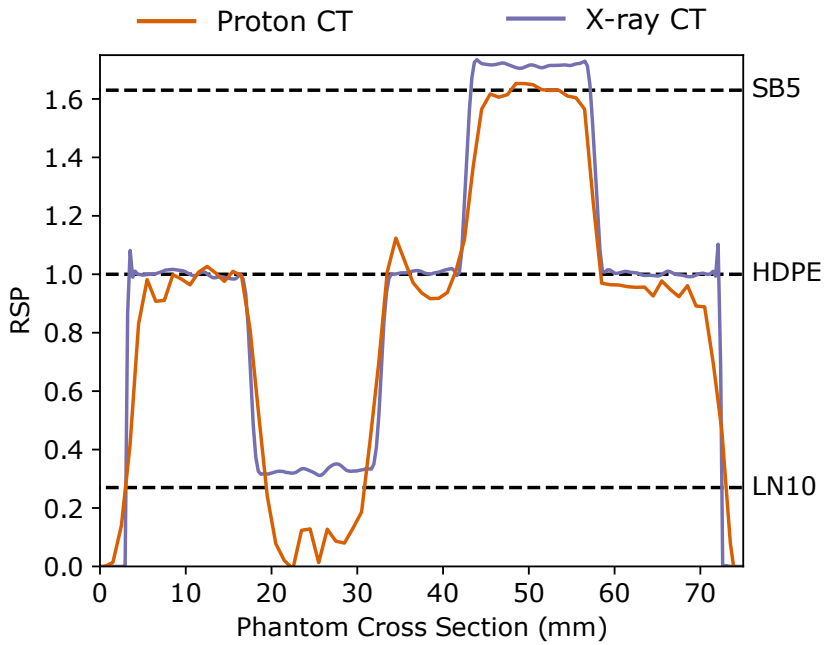

Figure 7.8: Cross sections taken through the two inhomogeneities of the phantom in the x-ray CT and proton CT images.

film irradiation experiment performed at iThemba. By using the EBT-3 film as a truth measurement, the accuracy of the dose calculations based on x-ray CT and proton CT can be evaluated by considering simulated proton ranges and comparing them against the film.

7.5.1 Geant4 DICOM import

In order to construct the voxelised phantom geometry in Geant4, modifications were made to the SuSi code to incorporate new functions based on classes included in the Geant4 DICOM example. The DICOM file format is a standard file format for medical imaging, allowing standardized transfer of information between medical computer systems. The DICOM file contains a header, with tags specific to the imaging modality used and the image is then stored as a binary array of integer values. The tags in the DICOM header provide specific information about the image including the pixel size, slice size and the relative location of each slice [90]. With this information, a voxelised geometry can be constructed.

Each CT scan was converted into a series of text files, each text file containing the pixel information in one slice. Two 2D arrays in the file correspond to a map assigning a material to each pixel and a second map containing the mass density of

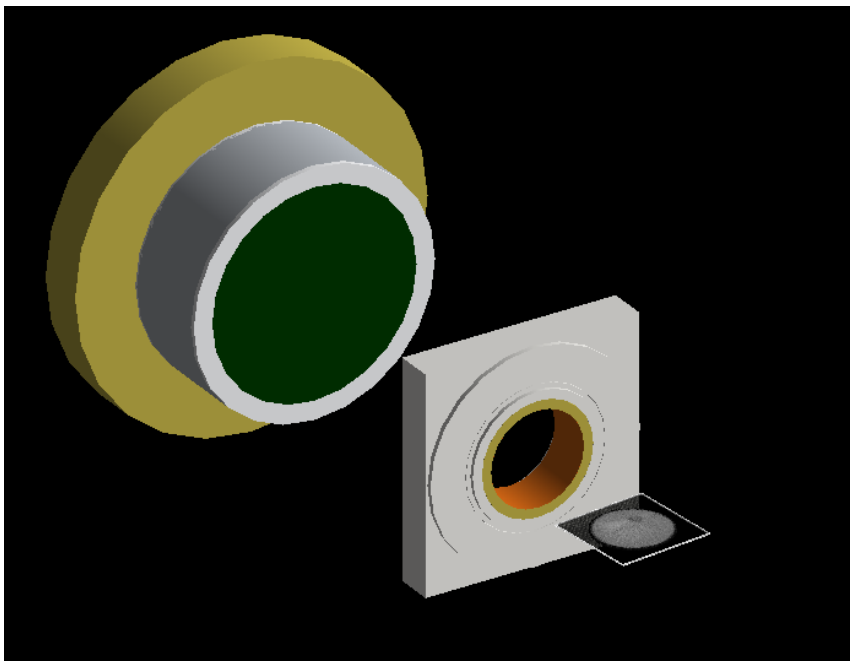

Figure 7.9: Visualisation of a single slice of the proton CT scan phantom geometry shown at the beam isocentre in SuSi. Also visible are the treatment collimator assembly and reference ionisation chamber.

the material each pixel. The Geant4 function reads in the information in the text file and produces voxels with the assigned material type and sets the mass density of each voxel based on the text file.

Using the proton CT and x-ray CT data sets, RSP maps of the phantom were produced for each slice. The proton CT image directly corresponds to the RSP of each voxel, whilst the HU measurements of the x-ray CT image required conversion to RSP. For both data sets, a binary mask measuring 75 mm in diameter was used to segment the phantom geometry from the background air. To perform the most direct import of RSP information into SuSi, each voxel comprising the phantom geometry had its material set as water. The mass density of each pixel was then equal to the RSP. The location of the imported phantom geometry was set as the proton beam isocentre, corresponding to the position used in the experiment. An image showing a single slice of the proton CT-based geometry in the SuSi simulation is shown in figure 7.9.

7.5.2 Scoring

Energy deposition in the phantom was scored in 0.1 mm x 0.1 mm bins in the plane of the phantom in 10 slices containing the inhomogeneities. To reduce aliasing

artefacts related to the particle step length in the simulation, the dose for each proton was deposited at a random point along the step length. Aliasing occurs when the radiation length of the interaction processes is larger than the voxel size. For efficiency Geant4 calculates a compounded proton path through the step length corresponding to the radiation length of the material that the proton is in. However, Geant4 also requires that the step finishes at a geometric boundary. If post-step or pre-step energy deposition is recorded, then voxel boundaries become apparent on the measured dose distribution. By depositing the dose at random points, the dose recording is more evenly distributed. For consistency between the proton CT scan and x-ray CT scan, where the voxel sizes are 1 mm and 0.3 mm respectively, a maximum step length of 0.1 mm was set in the DICOM volume so that the voxel sizes did not influence the simulated dose distributions.

7.5.3 Results

Two simulations were performed using each imaging dataset. In the first simulation the wedges were set in the simulation to deliver a range of 45 mm range in water, and in the second simulation the range was set to 52 mm range in water. The dose distributions in the phantoms for each simulation are shown in figure 7.10. Figures 7.11 and 7.12 illustrate the difference in the proton distributions calculated based on the x-ray CT and proton CT image. In these figures, absolute dose difference was calculated between the dose distributions calculated on the x-ray CT and proton CT image sets and normalised so that the regions with the largest dose difference are equal to 1. This difference map for the 45 mm and 52 mm range beam is overlaid on to the proton CT image and highlights the regions affected the most by range error between the x-ray CT and proton CT images.

Bragg peaks in three regions of the phantom are shown in the following figures. The locations of these profiles is shown in figure 7.13. We did not include LN10 using a 52 mm range beam in this analysis because the range of the proton beam ended outside the EBT-3 film window, therefore we could not resolve the Bragg peak. In these figures, the Bragg peak was taken along in a 1 mm cross-section through the centre of the phantom and the centre of the both of the inhomogeneities. The range is reported as the depth in the phantom as measured along a central profile, neglecting the circular structure of the phantom. The Bragg peaks are taken from measurement using EBT-3 film and the two simulations. Each curve is normalised to the maximum value at its peak to give a depth-dose curve. From these depth-dose curves, the proton range (R_{80}) was calculated and compared amongst the measurements and an absolute range error and a percentage range error were

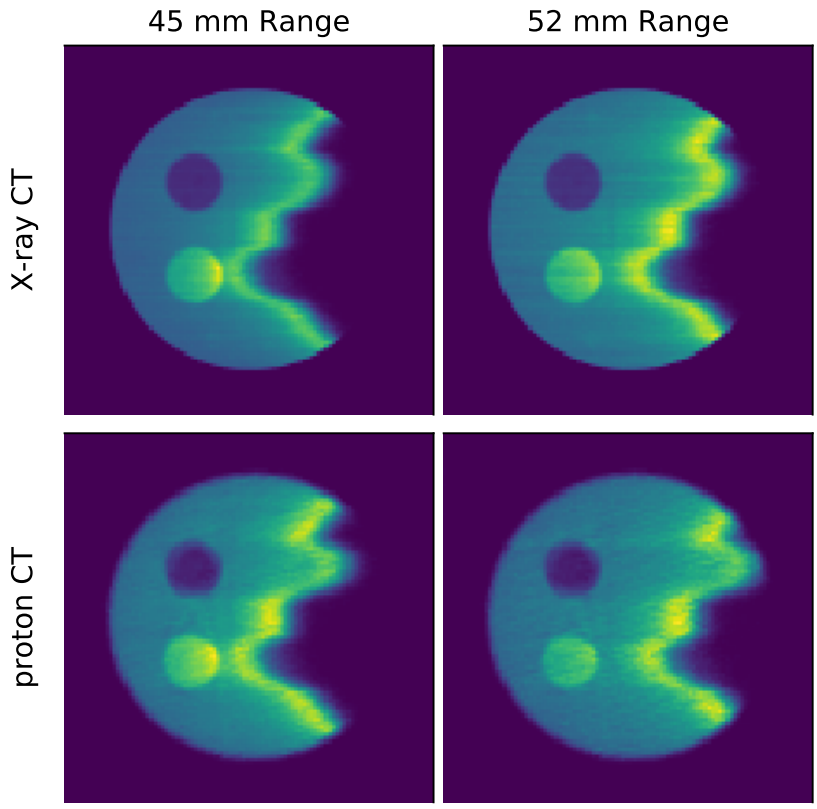

Figure 7.10: Image showing the 2D dose distributions from two different proton beams in phantom geometries generated from x-ray CT and proton CT images.

calculated. These are shown in table 7.2.

The range error based on the Monte Carlo dose calculations is considerably higher when using the proton CT image compared to x-ray CT. This is expected because of the proton CT dataset reconstructed the RSP of polyethylene inaccurately. However, the percentage range error reduced for proton CT when LN10 and SB5 inhomogeneities are introduced, despite the RSP of LN10 being significantly underestimated in the proton CT data set. This is because the amount of polyethylene that the beam travels through is reduced. The consistent nature of the range errors demonstrates that the image modality is relatively robust for dose calculations in the presence of inhomogeneities, despite a systematic error in the RSP of polyethylene. To put these results into a clinical context, typically a margin of the order of $3.5\% + 1\text{mm}$ is used when planning a proton therapy treatment, therefore range errors of 2.2 mm and 2.4 mm would be acceptable for a 45 mm and 52 mm range beam respectively.

The simulation based on the x-ray CT image shows good performance when

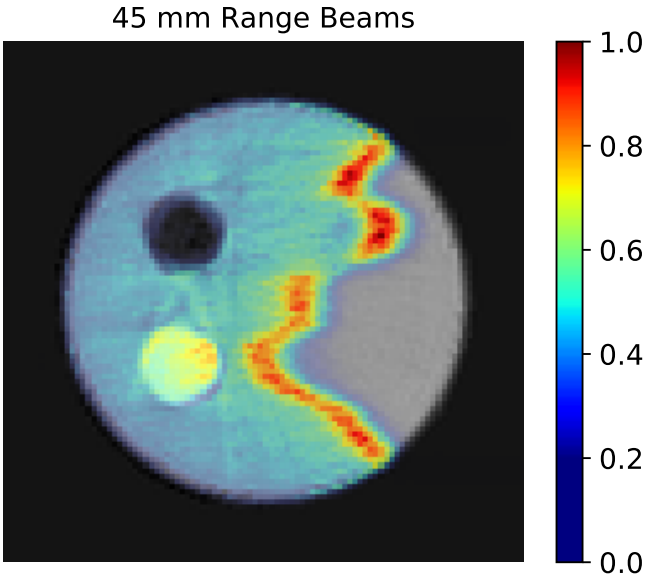

Figure 7.11: Relative dose differences between dose maps calculated on proton CT and x-ray CT images for a beam with nominally 45 mm range in water.

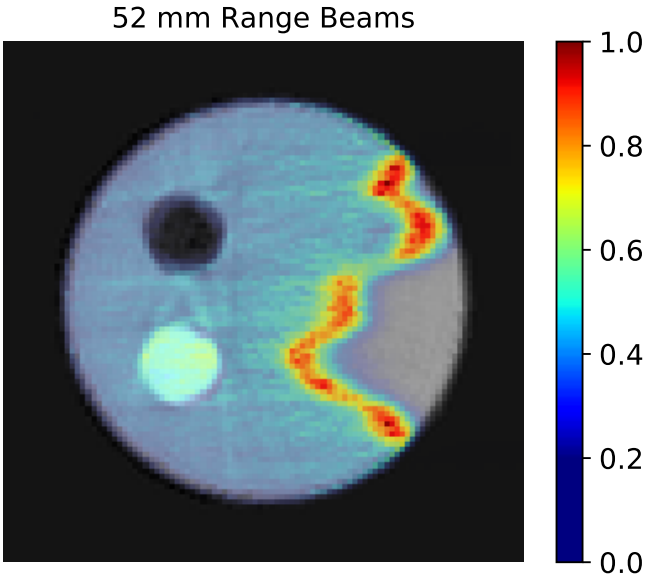

Figure 7.12: Relative dose differences between dose maps calculated on proton CT and x-ray CT images for a beam with nominally 52 mm range in water.

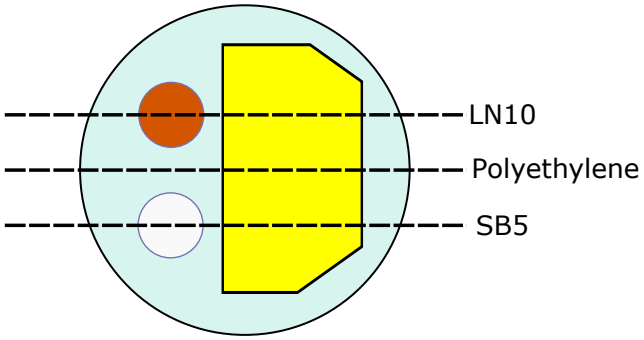

Figure 7.13: Schematic illustrating the location of the Bragg peaks analysed in this section.

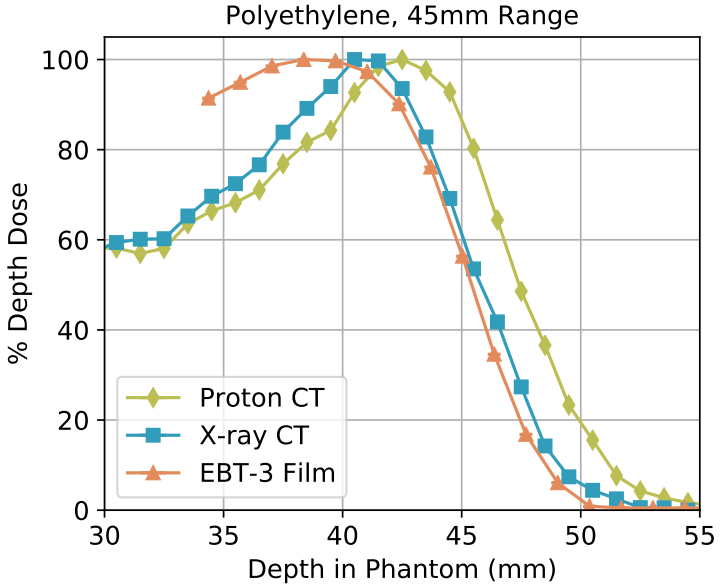

Figure 7.14: Depth-dose curves from simulations of a 45 mm range beam into the phantom based on x-ray CT and proton CT images compared with film measurement, through the centre of the phantom.

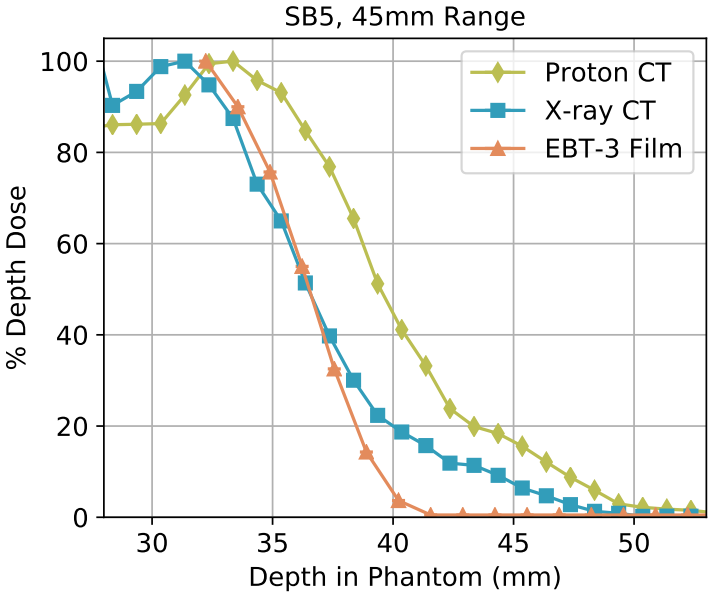

Figure 7.15: Depth-dose curves from simulations of a 45 mm range beam into the phantom based on x-ray CT and proton CT images compared with film measurement, through the SB5 inhomogeneity.

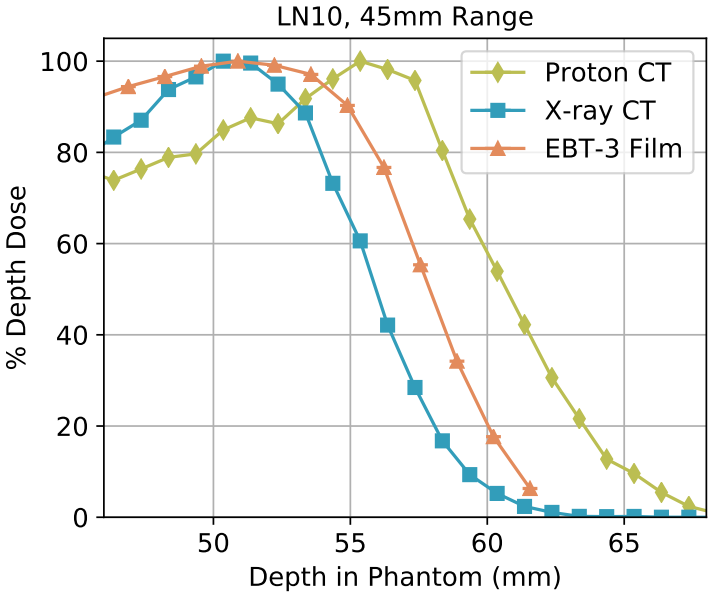

Figure 7.16: Depth-dose curves from simulations of a 45 mm range beam into the phantom based on x-ray CT and proton CT images compared with film measurement, through the LN10 inhomogeneity.

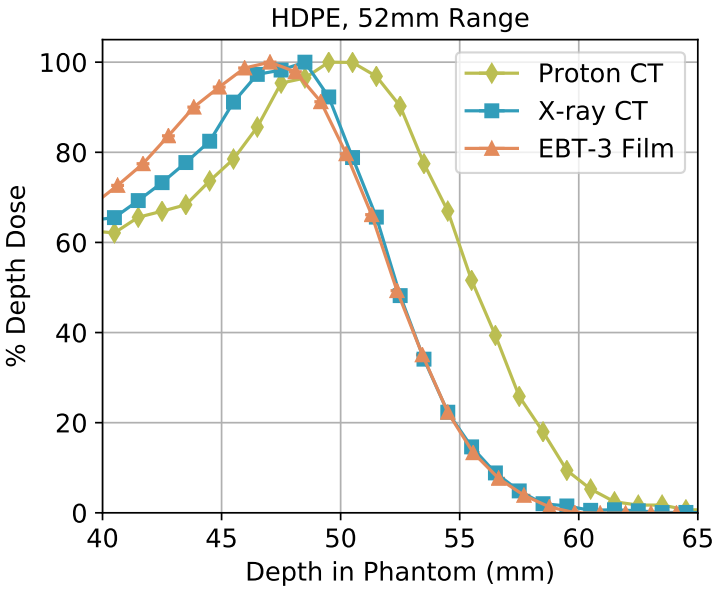

Figure 7.17: Depth-dose curves from simulations of a 52 mm range beam into the phantom based on x-ray CT and proton CT images compared with film measurement, through the centre of the phantom.

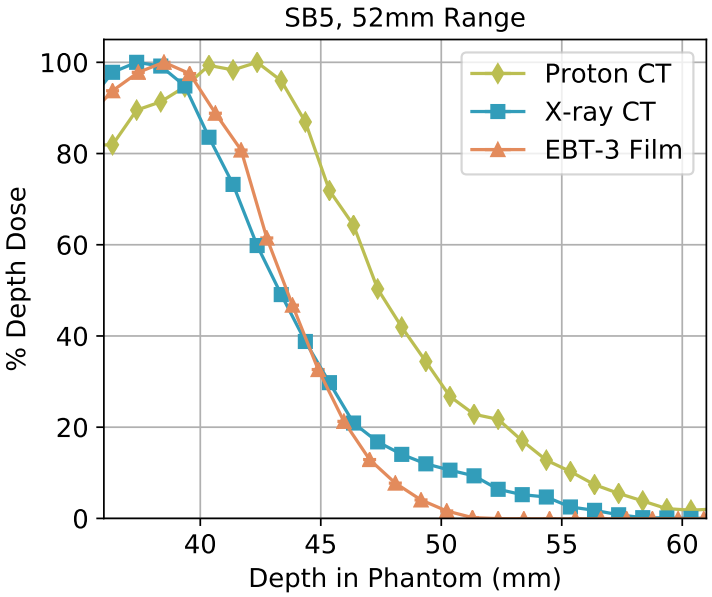

Figure 7.18: Depth-dose curves from simulations of a 52 mm range beam into the phantom based on x-ray CT and proton CT images compared with film measurement, through the SB5 inhomogeneity.

	Film	Simulation - proton CT			Simulation - x-ray CT		
Bragg Peak	Range (mm)	Range (mm)	Error (mm)	Error (%)	Range (mm)	Error (mm)	Error (%)
HDPE, 45mm Beam	43.3	45.0	1.7	3.9 %	43.7	0.4	0.9 %
SB5, 45mm Beam	34.5	36.8	2.3	6.6 %	33.9	0.6	-1.7 %
LN10, 45mm Beam	55.9	58.2	2.3	4.1 %	53.4	-2.5	-4.5 %
HDPE, 52mm Beam	49.6	52.9	3.3	6.6 %	50.0	0.4	-0.8 %
SB5, 52mm Beam	41.7	44.8	2.1	5.0 %	40.7	-1.0	-2.4 %

Table 7.2: Proton ranges in the phantom determined from Bragg peaks located in the cente of the phantom and behind the LN10 and SB5 inserts. The range referes fo the R_{80} measurement determined from the Bragg peak. Range errors are calculated for the two simulations by subtracting the range as recorded in EBT-3 film, and a percentage range error is calculated. HDPE is an abbreviation of high-density polyethylene.

calculating proton range in polyethylene however the accuracy is worse when calculating the range of protons that have propagated through SB5 and LN10. The magnitude of the errors for beams that have propagated through the LN10 inhomogeneity is similar to the magnitude of the error seen in proton CT simulation, albeit in an opposite direction. This is because the x-ray CT image overestimated the stopping powers of LN10. The range error behind SB5 is slightly lower. The large variation in the range errors suggests that, despite the reduction in absolute errors in soft tissue, there may be more range uncertainty associated with the use of x-ray CT when compared with proton CT over a broader range of tissues. These errors are all within the 1 sigma uncertainty on RSP estimation calculated by Yang et al for lung, soft tissue and bone [2].

The mean percentage range error based on the proton CT dose calculation is 5.24%, with a standard deviation of 1.2%. The mean percentage range error based on the x-ray CT calculation is -1.7% with a standard deviation of 1.7%. Considering the results of the range uncertainty analysis done in the previous chapter and reported by Bär et al [63], we can begin to realise the potential for proton CT to reduce range uncertainties. Whilst we see a systematic error, caused primarily by the RSP error in polyethylene, the standard deviation in the proton CT range error results is lower than that in x-ray CT. This suggests that the proton CT system behaves in a more predictable manner when faced with different types of materials than x-ray CT, albeit with some systematic error. There is a likelihood that the systematic error was caused by experimental error, therefore we conclude that further study is needed to investigate the source of this error.

7.6 Discussion

Presented in this chapter is a framework for evaluation of the PRaVDA proton CT system. Despite the poor performance of the proton CT system in this instance, to the author's best knowledge this is the only direct comparison of range calculations on experimental results from proton CT and x-ray CT images, validated against a direct measurement. The performance of the proton CT system in this instance clearly suffers from some systematic error, and therefore attention should be focused on the methodology. The PRaVDA proton CT system is a prototype system in its first stage of development and therefore we would expect improved results with further work.

The evaluation framework chosen in this chapter was decided upon to treat x-ray CT and proton CT fairly and without bias by using experimental measurement to validate the performance of the two imaging modalities. The framework may be improved in a number of ways as an evaluation framework for a clinical proton CT system. For example, the user may choose to use a clinical treatment planning system in the place of Monte Carlo simulation. For example, it was originally intended to plan nominally the same "treatment" on x-ray CT and proton CT images of the phantom, and then deliver them to see the range difference on film. However the nature of data acquisition, processing and reconstruction with PRaVDA meant that this was impossible during the experimental time we had available.

In a further evaluation framework, the user may choose to use a more clinically relevant phantom featuring anatomical geometries or even biological tissue. For example, a study to evaluate the use of dual-energy x-ray CT for proton therapy was performed using isolated range extinction measurements of animal tissue [91]. The range extinction method described in the literature highlights a shortfall in EBT-3 film used in this experiment. In order to accurately characterise the response of Gafchromic EBT-3 film, even for relative dosimetry, one needs to know the exact energy of the protons at the end of their range. We can determine this energy through the use of Monte Carlo simulation [88] however validating this becomes quite complicated.

The development nature of the PRaVDA proton CT system is evident throughout the results; the presence of image artefacts that can be explained by experimental error, limitations in the dynamic range of the detectors and experimental anomalies such as the range telescope calibration curve not accurately measuring residual proton range. The reconstruction method is also novel and relatively untested. The system in particular appeared to reconstruct the RSPs of cylindrical phantoms

around 5% lower than expected, corresponding to a WET difference of around 4 mm. This was also observed in a cylindrical animal tissue phantom, containing a lamb chop, that is not shown in this thesis. No explanation has yet been offered as to why this is, but it could be linked to the range telescope calibration or the compensator correction. The range telescope calibration (see chapter 2) deviates from the expected values as the water equivalent thickness of the object decreases. The two cylindrical phantoms were constructed mainly from polyethylene and agar gel respectively, thus meaning they had a lower WET than the spherical Bauble phantom. Secondly, the use of a compensator made from PMMA with a higher RSP than the two phantoms means that the phantom and compensator would have a non-uniform WET distribution across the phantom body. An assumption in the reconstruction code when applying the compensator correction could therefore be causing a systematic error.

7.7 Conclusion

In this chapter, a dosimetric phantom was imaged using x-ray CT and proton CT and irradiated using the beam at iThemba LABS. A measurement of the Bragg peaks inside the dosimetric phantom, taken using EBT-3 film was compared against simulated Bragg peaks calculated in phantom geometries generated using the proton CT and x-ray CT data sets. By doing this, we demonstrate that the accuracy of proton CT and x-ray CT for use in treatment planning could be evaluated. However, the developmental nature of the PRaVDA proton CT system does not provide relevant results.

X-ray CT performed robustly when used to evaluate proton range in polyethylene however underestimated the range of the protons propagating through SB5 and LN10, with a mean range error -1.7% and a standard deviation of 1.8%. Despite increased accuracy in determining the RSP of SB5, in the film phantom the RSP of polyethylene and LN10 was vastly underestimated leading to overestimation of proton range with a mean range error of 5.8% and standard deviation of 1.2%.

Range error in the proton CT image is due to issues reconstructing the quantitative RSP value of HDPE accurately. Further work needs to be done in this area before considering the impact of these results. The improved accuracy of RSP reconstruction shown in the Bauble phantom shows that proton CT would be a valid candidate for dose calculation, however the advantage of the film phantom is the ability to perform dosimetric measurements in order to compare the calculation to experimental measurement.

Chapter 8

Conclusions

In this thesis, a prototype proton computed tomography system is introduced, designed to accurately reconstruct proton stopping powers for use in proton therapy. An experimental demonstration of the accuracy of proton CT is performed, and we report the relative stopping powers of tissue equivalent materials measured by proton CT with an accuracy of better than 1.3% in plastic materials mimicking soft tissue and bone, when compared to stopping power measurements taken using a water tank. The effect of stopping power accuracy on range uncertainty is tested by modelling the range error introduced in a 1D Bragg peak due to the distribution of stopping powers errors in the proton CT measurement. The range error is compared against calculations performed for dual-energy x-ray CT reported in the literature [63]. The results from this test show that if artefacts in the proton CT image of the Bauble image are corrected for then the proton CT system may perform marginally better than dual energy x-ray CT in terms of reducing proton therapy range uncertainty when compared to single energy x-ray CT. Sources of the image artefacts were investigated and an explanation as so their sources are offered. The presence of the streak artefacts appears to be caused by the effective WEPL measurement of high energy proton being clipped by the dynamic range of the calorimeter. A second ring artefact is present due to misalignment of the compensator during experimental measurement. A correction can be applied to the latter artefact. The former artefact would require an improved proton range measurement system capable of resolving protons with a higher range or energy.

In terms of RSP accuracy demonstrated with the Bauble phantom, the results from the PRaVDA proton CT system are slightly poorer than those from the LLU/SCSC phase-II proton CT scanner, who have so far provided the best experimental proton CT results [29] demonstrating accuracy of better than 1%. However,

LLU/SSC obtained their best results after many stages of optimisation to the calibration of their range measurement as well as improvements in the reconstruction algorithm [55]. With further optimisation, we would expect PRaVDA to similarly improve the RSP accuracy. A limitation to the optization of PRaVDA has been the availability of experimental time, however with a validated Monte Carlo beamline model there is a possibility to perform and optimise simulated CT scan performance prior to designing a new system.

One result that requires immediate further study is the proton CT scan of the film phantom shown in chapter 7. With the film phantom, we demonstrate Monte Carlo dose calculation on a proton CT image. The calculated proton range is compared against a calculation on an x-ray CT image and an experimental measurement performed with EBT-3 film. It was determined prior to the comparison that the RSP of polyethylene in the film phantom was reconstructed incorrectly and this with significantly influence the range calculation. As such, we see range errors upto 6.6% in Bragg peaks calculated on the proton CT image in a homogeneous medium. However the result does not get worse when inhomogeneities are introduced. It is possible that a systematic error in the data exists and this requires further investigation. However, we demonstrate that we can calculate dose distributions on proton CT data. In the literature, there are reports of dose distributions being calculated on simulated proton CT data as well as x-ray CT data [92], however to our knowledge this is the first report of dose calulcations performed on experimental proton CT data. We note that the LLU/SSC report an intention to do dose calculations on validated simulated proton CT data using a clinical treatment planning system however no results have yet been published [44].

Further development of the PRaVDA system should focus on improving the range telescope. The artefacts arising in the Bauble phantom proton CT scans have their origins in the lack of dynamic range in the current range telescope. We note that the LLU/SCSC "hybrid" range-energy detector, using scintillator technology, meets the demands for WET resolution in a proton CT detector and has suitable dynamic range to resolve the range of individual protons in a beam with a nominal energy of 200 MeV [93]. In contrast, the current PRaVDA range telescope cannot resolve protons above an energy 80 MeV. A possible approach could be to use CMOS active pixel sensors, an approach originally considered by PRaVDA [51]. Obtaining proton signal sizes from the CMOS sensor would allow a solid-state "hybrid" approach to be taken, where the energy of individual protons may be determined from the size of the measured signal in the CMOS sensor. A proton CT project based at the University of Bergen demonstrate the use of CMOS active pixel sensors with a 2

kHz frame rate in a range detector [48], with the design comprising 41 layers separated by aluminium absorbers with a higher WET than the PMMA absorbers used in the PRaVDA system allowing them to resolve proton energies of up to 230 MeV. With their tracking algorithm they demonstrate that they are capable of resolving close to 10^6 protons per second, approaching the rate required for a clinically usable proton CT system. However this tracking rate requires a proton beam with a sparse spatial distribution. Improved proton tracking may be required for modern proton therapy systems with a spot-scanning design, where a high intensity proton pencil beam is magnetically scanned across the patient.

To conclude, we demonstrate a prototype proton therapy system with initial results comparable to another research proton CT scanner. Simple range uncertainty calculations suggest a possible advantage for proton CT over dual energy x-ray CT, however we do not yet have a robust system and we see systematic errors in the reconstruction of the film that need further investigation. All of the images acquired with the PRaVDA system have been performed at relatively low energies on simple phantoms that do not replicate patient geometries. Further development of the range telescope would be required in order to improve the system, however there are still a number of technical and practical challenges to overcome before the technology becomes applicable in a clinical setting.

Bibliography

[1] R. R. Wilson. Radiological use of fast protons. *Radiology*, 47(5):487–91, 1946. doi:10.1148/47.5.487.

[2] M. Yang, X. R. Zhu, P. C. Park, U. Titt, R. Mohan, G. Virshup, J. E. Clayton, and L. Dong. Comprehensive analysis of proton range uncertainties related to patient stopping-power-ratio estimation using the stoichiometric calibration. *Phys Med Biol.*, 57(13):4095–115, 2012. doi:10.1088/0031-9155/57/13/4095.

[3] S. S. Ahmad, S. Duke, R. Jena, M. V. Williams, and N. G. Burnet. Advances in radiotherapy. *BMJ*, 345, 2012. doi:10.1136/bmj.e7765.

[4] P. Symonds, C. Deehan, J. A. Mills, and C. Meredith, editors. *Walter and Miller's Textbook of Radiotherapy.* Churchill Livingstone, 7th edition, 2012.

[5] C-M. Ma and T. Lomax. *Proton and Carbon Ion Therapy.* CRC Press, 1st edition, 2012.

[6] Particle Therapy Co-Operative Group. Facilities in Operation, 2018. URL `https://www.ptcog.ch/index.php/facilities-in-operation`.

[7] B. Gottschalk. Physics of proton interactions in matter. In H. Paganetti, editor, *Proton Therapy Physics.* CRC Press, 1st edition, 2012.

[8] International Commission on Radiation Units and Measurement. ICRU Report 49: Stopping Powers and Ranges for Protons and Alpha Particles. Technical Report 49, International Commission on Radiation Units and Measurement, 1993.

[9] H. Owen, A. Lomax, and S. Jolly. Current and future accelerator technologies for charged particle therapy. *Nucl. Instrum. Meth. Phys. Res. Sect. A Accel. Spectrometers, Detect. Assoc. Equip.*, 809:96–104, 2015. doi:10.1016/j.nima.2015.08.038.

[10] R. Zhang, R. M. Howell, A. Giebeler, P. J. Taddei, A. Mahajan, and W. D. Newhauser. Comparison of risk of radiogenic second cancer following photon and proton craniospinal irradiation for a pediatric medulloblastoma patient. *Phys Med Biol.*, 58(4):807–23, 2013. doi:10.1088/0031-9155/58/4/807.

[11] P. J. Doolan, C. A. Collins-Fekete, M. F. Dias, T. A. Ruggieri, D. D'Souza, and J. Seco. Inter-comparison of relative stopping power estimation models for proton therapy. *Phys Med Biol.*, 61(22):8085–8104, 2016. doi:10.1088/0031-9155/61/22/8085.

[12] U. Schneider, E. Pedroni, and A. Lomax. The calibration of CT Hounsfield units for radiotherapy treatment planning. *Phys Med Biol.*, 41(1):111–24, 1996. doi:10.1088/0031-9155/41/1/009.

[13] International Commission on Radiation Units and Measurement. ICRU Report 37: Stopping Powers for Electrons and Positrons. Technical report, International Commission on Radiation Units and Measurement, 1984.

[14] J. Ödén, J. Zimmerman, R. Bujila, P. Nowik, and G. Poludniowski. Technical Note: On the calculation of stopping-power ratio for stoichiometric calibration in proton therapy. *Med Phys.*, 42(9):5252–5257, 2015. doi:10.1118/1.4928399.

[15] Harald Paganetti. Range uncertainties in proton therapy and the role of Monte Carlo simulations. *Phys Med Biol.*, 57:R99–117, 2012. doi:10.1088/0031-9155/57/11/R99.

[16] E. Bär, P. Andreo, A. Lalonde, G. Royle, and H. Bouchard. Optimized I-values for use with the Bragg additivity rule and their impact on proton stopping power and range uncertainty. *Phys Med Biol.*, 63(16):165007, 2018. doi:10.1088/1361-6560/aad312.

[17] B. Gottschalk. On the scattering power of radiotherapy protons. *Med. Phys.*, 37(1):352–367, 2010. doi:10.1118/1.3264177.

[18] A. M. Koehler, R. J. Schneider, and J. M. Sisterson. Flattening of proton dose distributions for large-field radiotherapy. *Med Phys.*, 4(4):297, 1977. doi:10.1118/1.594317.

[19] R. W. Schulte, S. N. Penfold, J. T. Tafas, and K. E. Schubert. A maximum likelihood proton path formalism for application in proton computed tomography. *Med. Phys.*, 35(11):4849–4856, 2008. doi:10.1118/1.2986139.

[20] C. T. Quiñones, J. M. Létang, and S. Rit. Filtered back-projection reconstruction for attenuation proton CT along most likely paths. *Phys Med Biol.*, 61(9): 3258–3278, 2016. doi:10.1088/0031-9155/61/9/3258.

[21] C.-A. Collins-Fekete, S. Brousmiche, S. K. N. Portillo, L. Beaulieu, and J. Seco. A maximum likelihood method for high resolution proton radiography/proton CT. *Phys Med Biol.*, 61(23):8232–8248, 2016. doi:10.1088/0031-9155/61/23/8232.

[22] G. Poludniowski, N. M. Allinson, and P. M. Evans. Proton radiography and tomography with application to proton therapy. *Brit J Radiol.*, 88(1053): 20150134, 2015. doi:10.1259/bjr.20150134.

[23] C. Bopp, R. Rescigno, M. Rousseau, and D. Brasse. Quantitative proton imaging from multiple physics processes: a proof of concept. *Phys Med Biol.*, 60 (13):5325–5341, 2015. doi:10.1088/0031-9155/60/13/5325.

[24] J. T. Taylor, G. Poludniowski, T. Price, C. Waltham, P. P. Allport, G. L. Casse, M. Esposito, P. M. Evans, S. Green, S. Manger, S. Manolopoulos, J. Nieto-Camero, D. J. Parker, J. Symons, and N. M. Allinson. An experimental demonstration of a new type of proton computed tomography using a novel silicon tracking detector. *Med. Phys.*, 43(11):6129, 2016. doi:10.1118/1.4965809.

[25] W. D. Newhauser and R. Zhang. The physics of proton therapy. *Phys Med Biol.*, 60(8):R155–R209, 2015. doi:10.1088/0031-9155/60/8/R155.

[26] A. C. Knopf and A. Lomax. In vivo proton range verification: a review. *Phys Med Biol.*, 58(15):R131–60, 2013. doi:10.1088/0031-9155/58/15/R131.

[27] J. Seco and M. F. Spadea. Imaging in particle therapy: State of the art and future perspective. *Acta Oncol. (Madr).*, 54(9):1254–1258, 2015. doi:10.3109/0284186X.2015.1075665.

[28] A. M. Cormack. Representation of a Function by Its Line Integrals, with Some Radiological Applications. *J. Appl. Phys.*, 34(9):2722–2727, 1963. doi:10.1063/1.1729798.

[29] R. P. Johnson. Review of medical radiography and tomography with proton beams. *Reports Prog. Phys.*, 81(1), 2018. doi:10.1088/1361-6633/aa8b1d.

[30] A. M. Cormack and A. M. Koehler. Quantitative proton tomography: preliminary experiments. *Phys Med Biol.*, 21(4):007, 1976. doi:10.1088/0031-9155/21/4/007.

[31] K. M. Hanson, J. N. Bradbury, T. M. Cannon, R. L. Hutson, D. B. Laubacher, R. J. Macek, M. A. Paciotti, and C. A. Taylor. Computed tomography using proton energy loss. *Phys Med Biol.*, 26(6):965–983, 1981. doi:10.1088/0031-9155/26/6/001.

[32] M. F. Moyers, D. W. Miller, D. A. Bush, and J. D. Slater. Methodologies and tools for proton beam design for lung tumors. *Int. J. Radiat. Oncol. Biol. Phys.*, 49(5):1429–1438, 2001. doi:10.1016/S0360-3016(00)01555-8.

[33] R. W. Schulte, V. Bashkirov, M. C. Klock, T. Li, A. J. Wroe, I. Evseev, D. C. Williams, and T. Satogata. Density resolution of proton computed tomography. *Med Phys.*, 32(4):1035–1046, 2005. doi:10.1118/1.1884906.

[34] A. M. Koehler. Proton Radiography. *Science.*, 160(3825):303–304, 1968. doi:10.1126/science.160.3825.303.

[35] K. M. Hanson. Proton Computed Tomography. *IEEE Trans. Nucl. Sci.*, 26(1): 1635–1640, 1979. doi:10.1109/TNS.1979.4330455.

[36] S. L. Kramer, D. R. Moffett, R. L. Martin, E. P. Colton, and V. W. Steward. Proton imaging for medical applications. *Radiology*, 135(2):485–494, 1980. doi:10.1148/radiology.135.2.6245430.

[37] K. M. Hanson, J. N. Bradbury, R. A. Koeppe, R. J. MacEk, D. R. MacHen, R. Morgado, M. A. Paciotti, S. A. Sandford, and V. W. Steward. Proton computed tomography of human specimens. *Phys Med Biol.*, 27(1):25–36, 1982. doi:10.1088/0031-9155/27/1/003.

[38] B. Schultze, P. Karbasi, V. Giacometti, T. E. Plautz, K. E. Schubert, and R. W. Schulte. Reconstructing highly accurate relative stopping powers in proton computed tomography. *2015 IEEE Nucl. Sci. Symp. Med. Imaging Conf.*, 2015. doi:10.1109/NSSMIC.2015.7582218.

[39] U. Schneider, J. Besserer, P. Pemler, M. Dellert, M. Moosburger, E. Pedroni, and B. Kaser-Hotz. First proton radiography of an animal patient. *Med Phys.*, 31(5):1046, 2004. doi:10.1118/1.1690713.

[40] U. Schneider, P. Pemler, J. Besserer, E. Pedroni, A. Lomax, and B. Kaser-Hotz. Patient specific optimization of the relation between CT-Hounsfield units and proton stopping power with proton radiography. *Med. Phys.*, 32(1):195–199, 2005. doi:10.1118/1.1833041.

[41] H. F.W. Sadrozinski, R. P. Johnson, S. MacAfee, A. Plumb, D. Steinberg, A. Zatserklyaniy, V. A. Bashkirov, R. F. Hurley, and R. W. Schulte. Development of a head scanner for proton CT. *Nucl. Instrum. Meth. Phys. Res. Sect. A Accel. Spectrometers, Detect. Assoc. Equip.*, 699:205–210, 2013. doi:10.1016/j.nima.2012.04.029.

[42] R. P. Johnson, V. Bashkirov, L. Dewitt, V. Giacometti, R. F. Hurley, P. Piersimoni, T. E. Plautz, H. F. W. Sadrozinski, K. Schubert, R. Schulte, B. Schultze, and A. Zatserklyaniy. A Fast Experimental Scanner for Proton CT: Technical Performance and First Experience with Phantom Scans. *IEEE Trans. Nucl. Sci.*, 63(1):52–60, 2016. doi:10.1109/TNS.2015.2491918.

[43] T. E. Plautz. *An Evaluation of a Prototype Proton Computed Tomography Scanner*. PhD thesis, University of Santa Cruz, 2016.

[44] V. Giacometti, S. Guatelli, M. Bazalova-Carter, A. B. Rosenfeld, and R. W. Schulte. Development of a high resolution voxelised head phantom for medical physics applications. *Phys. Medica*, 33:182–188, 2017. doi:10.1016/j.ejmp.2017.01.007.

[45] M. Scaringella, M. Bruzzi, M. Bucciolini, M. Carpinelli, G. A P Cirrone, C. Civinini, G. Cuttone, D. Lo Presti, S. Pallotta, C. Pugliatti, N. Randazzo, F. Romano, V. Sipala, C. Stancampiano, C. Talamonti, E. Vanzi, and M. Zani. A proton Computed Tomography based medical imaging system. *J. Instrum.*, 9(12), 2014. doi:10.1088/1748-0221/9/12/C12009.

[46] M. Bucciantonio, U. Amaldi, R. Kieffer, F. Sauli, and D. Watts. Development of a fast proton range radiography system for quality assurance in hadrontherapy. *Nucl. Instrum. Meth. Phys. Res. Sect. A Accel. Spectrometers, Detect. Assoc. Equip.*, 732:564–567, 2013. doi:10.1016/j.nima.2013.05.110.

[47] M. Naimuddin, G. Coutrakon, G. Blazey, S. Boi, A. Dyshkant, B. Erdelyi, D. Hedin, E. Johnson, J. Krider, V. Rukalin, S. A. Uzunyan, V. Zutshi, R. Fordt, G. Sellberg, J. E. Rauch, M. Roman, P. Rubinov, and P. Wilson. Development of a proton Computed Tomography detector system. *J. Instrum.*, 11(2), 2016. doi:10.1088/1748-0221/11/02/C02012.

[48] H.E.S. Pettersen, J. Alme, A. Biegun, A. van den Brink, M. Chaar, D. Fehlker, I. Meric, O.H. Odland, T. Peitzmann, E. Rocco, K. Ullaland, H. Wang, S. Yang, C. Zhang, and D. Röhrich. Proton tracking in a high-granularity Digital Tracking Calorimeter for proton CT purposes. *Nucl. Instrum. Meth. Phys.*

Res. Sect. A Accel. Spectrometers, Detect. Assoc. Equip., 860:51–61, 2017. doi:10.1016/j.nima.2017.02.007.

[49] J. T. Taylor, P. P. Allport, G. L. Casse, N. A. Smith, I. Tsurin, N. M. Allinson, M. Esposito, A. Kacperek, J. Nieto-Camero, T. Price, and C. Waltham. Proton tracking for medical imaging and dosimetry. *J. Instrum.*, 10(02):C02015–C02015, 2015. doi:10.1088/1748-0221/10/02/C02015.

[50] J. T. Taylor, C. Waltham, T. Price, N. M. Allinson, P. P. Allport, G. L. Casse, A. Kacperek, S. Manger, N. A. Smith, and I. Tsurin. A new silicon tracker for proton imaging and dosimetry. *Nucl. Instrum. Meth. Phys. Res. Sect. A Accel. Spectrometers, Detect. Assoc. Equip.*, 831:362–366, 2016. doi:10.1016/j.nima.2016.02.013.

[51] M. Esposito, T. Anaxagoras, P. M. Evans, S. Green, S. Manolopoulos, J. Nieto-Camero, D. J. Parker, G. Poludniowski, T. Price, C. Waltham, and N. M. Allinson. CMOS Active Pixel Sensors as energy-range detectors for proton Computed Tomography. *J. Instrum.*, 10(06):C06001–C06001, 2015. doi:10.1088/1748-0221/10/06/C06001.

[52] M. Eposito, T. Price, S. Manger, C. Waltham, T. Anaxagoras, D.J. Parker, J. Nieto-Camero, and N. M. Allinson. A large area CMOS active pixel sensor for imaging in proton therapy. *J Instrum.*, 13, 2018. doi:10.1088/1748-0221/13/11/P11017.

[53] G. Poludniowski, N. M. Allinson, and P. M. Evans. Proton Computed Tomography reconstruction using a backprojection-then-filtering approach. *Phys Med Biol.*, 59(24):7905, 2014. doi:10.1088/0031-9155/59/24/7905.

[54] A. C. Kak and M. Slaney. *Principles of Computerized Tomographic Imaging*. Society for Industrial and Applied Mathematics, 2001. ISBN 978-0-89871-494-4. doi:10.1137/1.9780898719277.

[55] C. E. Ordoez, N. Karonis, K. Duffin, G. Coutrakon, R. Schulte, R. Johnson, and M. Pankuch. A Real-time Image Reconstruction System for Particle Treatment Planning Using Proton Computed Tomography (pCT)". *Physics Procedia*, 90: 193 – 199, 2017. doi:https://doi.org/10.1016/j.phpro.2017.09.058.

[56] J. L. Conradie and P. O. Box. The Accelerator Facilities of the National Research Foundation in South Africa. *Proceedings of RuPAC 2008*, 2008.

[57] International Commission on Radiation Units and Measurement. Report 44: Tissue Substitutes in Radiation Dosimetry and Measurement. Technical Report 2, International Commission on Radiation Units and Measurement, 1988.

[58] Leeds Test Objects. Elemental Composition of Tissue Equivalent Materials, 2014.

[59] R. Zhang and W. D. Newhauser. Calculation of water equivalent thickness of materials of arbitrary density, elemental composition and thickness in proton beam irradiation. *Phys Med Biol.*, 54(6):1383–1395, 2009.

[60] I. G. Hughes and T. P. A. Hase. Least-squares fitting of complex functions. In *Measurements and their Uncertainties*, pages 67–83. OUP, 2010.

[61] M. J. Berger, J.S. Coursey, M.A Zucker, and J. Chang. ESTAR, PSTAR, and ASTAR: Computer Programs for Calculating Stopping-Power and Range Tables for Electrons, Protons, and Helium Ions (version 2.0.1), 2017. URL `http://physics.nist.gov/Star`.

[62] E. De Kock. Program CT CALIBRATE CT calibration curves for proton radiotherapy planning. Technical report, iThemba LABS, 2003.

[63] E. Bär, A. Lalonde, G. Royle, H. M. Lu, and H. Bouchard. The potential of dual-energy CT to reduce proton beam range uncertainties. *Med. Phys.*, 2017. doi:10.1002/mp.12215.

[64] International Commission on Radiation Units and Measurement. ICRU Report 46: Photon, electron, proton and neutron interaction data for body tissues. Technical report, International Commission on Radiation Units and Measurement, 1992.

[65] D. F. Jackson and D. J. Hawkes. X-ray attenuation coefficients of elements and mixtures. *Phys. Rep.*, 70(3):169–233, 1981. doi:10.1016/0370-1573(81)90014-4.

[66] H. Q. Woodard and D. R. White. Bone models for use in radiotherapy dosimetry. *Brit J Radiol.*, 55(652):277–282, 1982. doi:10.1259/0007-1285-55-652-277.

[67] H. Q. Woodard and D. R. White. The composition of body tissues. *Brit J Radiol*, 59(708):1209–1218, 1986. doi:10.1259/0007-1285-59-708-1209.

[68] J. Hsieh. *Computed Tomography: Principles, Design, Artifacts, and Recent Advances*. SPIE PRESS, 2015. ISBN 9781628418255. doi:10.1117/3.2197756.

[69] C. Jekel. pwlf: Python Library, 2018.

[70] M. Yang, G. Virshup, J. Clayton, X. R. Zhu, R. Mohan, and L. Dong. Theoretical variance analysis of single- and dual-energy computed tomography methods for calculating proton stopping power ratios of biological tissues. *Phys Med Biol.*, 55(5):1343–1362, 2010. doi:10.1088/0031-9155/55/5/006.

[71] D. C. Hansen, J. Seco, T. S. Sørensen, J. B. B. Petersen, J. E. Wildberger, F. Verhaegen, and G. Landry. A simulation study on proton computed tomography (CT) stopping power accuracy using dual energy CT scans as benchmark. *Acta Oncol.*, 54(9):1–5, 2015. doi:10.3109/0284186X.2015.1061212.

[72] D. Young. Hough transform for circles. https://uk.mathworks.com/matlabcentral/fileexchange/26978-hough-transform-for-circles.

[73] A. Lalonde and H. Bouchard. A general method to derive tissue parameters for Monte Carlo dose calculation with multi-energy CT. *Phys Med Biol.*, 61(22): 8044–8069, 2016. doi:10.1088/0031-9155/61/22/8044.

[74] R. F. Hurley, R. W. Schulte, V. A. Bashkirov, A. J. Wroe, A. Ghebremedhin, H. F. W. Sadrozinski, V. Rykalin, G. Coutrakon, P. Koss, and B. Patyal. Water-equivalent path length calibration of a prototype proton CT scanner. *Med. Phys.*, 39(5):2438–46, 2012. doi:10.1118/1.3700173.

[75] P. J. Doolan, M. Testa, G. Sharp, E. H. Bentefour, G. Royle, and H-M. Lu. Patient-specific stopping power calibration for proton therapy planning based on single-detector proton radiography. *Phys Med Biol.*, 60(5):1901–1917, 2015. doi:10.1088/0031-9155/60/5/1901.

[76] S. Agostinelli, J. Allison, K. Amako, J. Apostolakis, H. Araujo, P. Arce, M. Asai, D. Axen, S. Banerjee, G. Barrand, F. Behner, L. Bellagamba, J. Boudreau, L. Broglia, A. Brunengo, H. Burkhardt, S. Chauvie, J. Chuma, R. Chytracek, G. Cooperman, G. Cosmo, P. Degtyarenko, A. Dell'Acqua, G. Depaola, D. Dietrich, R. Enami, A. Feliciello, C. Ferguson, H. Fesefeldt, G. Folger, F. Foppiano, A. Forti, S. Garelli, S. Giani, R. Giannitrapani, D. Gibin, J.J. Gómez Cadenas, I. González, G. Gracia Abril, G. Greeniaus, W. Greiner, V. Grichine, A. Grossheim, S. Guatelli, P. Gumplinger, R. Hamatsu, K. Hashimoto, H. Hasui, A. Heikkinen, A. Howard, V. Ivanchenko, A. Johnson, F.W. Jones, J. Kallenbach, N. Kanaya, M. Kawabata, Y. Kawabata, M. Kawaguti, S. Kelner, P. Kent, A. Kimura, T. Kodama, R. Kokoulin,

M. Kossov, H. Kurashige, E. Lamanna, T. Lampén, V. Lara, V. Lefebure, F. Lei, M. Liendl, W. Lockman, F. Longo, S. Magni, M. Maire, E. Medernach, K. Minamimoto, P. Mora de Freitas, Y. Morita, K. Murakami, M. Nagamatu, R. Nartallo, P. Nieminen, T. Nishimura, K. Ohtsubo, M. Okamura, S. O'Neale, Y. Oohata, K. Paech, J. Perl, A. Pfeiffer, M.G. Pia, F. Ranjard, A. Rybin, S. Sadilov, E. Di Salvo, G. Santin, T. Sasaki, N. Savvas, Y. Sawada, S. Scherer, S. Sei, V. Sirotenko, D. Smith, N. Starkov, H. Stoecker, J. Sulkimo, M. Takahata, S. Tanaka, E. Tcherniaev, E. Safai Tehrani, M. Tropeano, P. Truscott, H. Uno, L. Urban, P. Urban, M. Verderi, A. Walkden, W. Wander, H. Weber, J.P. Wellisch, T. Wenaus, D.C. Williams, D. Wright, T. Yamada, H. Yoshida, and D. Zschiesche. Geant4a simulation toolkit. *Nucl. Instrum. Meth. Phys. Res. Sect. A Accel. Spectrometers, Detect. Assoc. Equip.*, 506(3):250–303, 2003.

[77] J. Jeyasugiththan, S. Peterson, J. Nieto-Camero, and J. Symons. Validation of a passive beam Monte Carlo model for measuring prompt gamma rays during proton radiotherapy. In *Proceedings, 58th Annual Conference of the South African Institute of Physics (SAIP 2013)*, Zululand, South Africa, 2013.

[78] T. Price, M. Esposito, G. Poludniowski, J. Taylor, C. Waltham, D.J. Parker, S. Green, S. Manolopoulos, N.M. Allinson, T. Anaxagoras, P. Evans, and J. Nieto-Camero. Expected proton signal sizes in the PRaVDA Range Telescope for proton Computed Tomography. *J. Instrum.*, 10(05):P05013–P05013, 2015. doi:10.1088/1748-0221/10/05/P05013.

[79] International Commission on Radiation Units and Measurement. ICRU Report 73: Stopping of Ions Heavier Than Helium. Technical Report 1, International Commission on Radiation Units and Measurement, 2005.

[80] G. A. P. Cirrone, G. Cuttone, F. Di Rosa, S. E. Mazzaglia, F. Romano, A. Attili, F. Bourhaleb, G. Russo, P. Kataniemi, A. Heikkinen, F. Marchetto, and S. Jungwook. Hadrontherapy: An open source, Geant4-based application for proton-ion therapy studies. *IEEE Nucl. Sci. Symp. Conf. Rec.*, pages 4186–4189, 2009. doi:10.1109/NSSMIC.2009.5402279.

[81] Geant4. Use Cases - Reference Physics Lists, 2018. URL `https://geant4.web.cern.ch/node/302`.

[82] T. Bortfeld. An analytical approximation of the Bragg curve for therapeutic proton beams. *Med. Phys.*, 24(12):2024, 1997. doi:10.1118/1.598116.

[83] P. Andreo. On the clinical spatial resolution achievable with protons and heavier charged particle radiotherapy beams. *Phys. Med. Biol*, 54:205–215, 2009. doi:10.1088/0031-9155/54/11/N01.

[84] D. Schardt, P. Steidl, M. Krämer, U. Weber, K. Parodi, and S. Brons. Precision Bragg-curve measurements for light-ion beams in water. *GSI Scientific Report 2007*, 1(2008-1):373, 2008.

[85] S. Devic, N. Tomic, and D. Lewis. Reference radiochromic film dosimetry: Review of technical aspects. *Phys Medica.*, 32(4):541–556, 2016. doi:10.1016/j.ejmp.2016.02.008.

[86] L. Zhao and I. J. Das. Gafchromic EBT film dosimetry in proton beams. *Phys Med Biol.*, 55(10):291–301, 2010. doi:10.1088/0031-9155/55/10/N04.

[87] D. Kirby, S. Green, H. Palmans, R. Hugtenburg, C. Wojnecki, and D. Parker. LET dependence of GafChromic films and an ion chamber in low-energy proton dosimetry. *Phys Med Biol.*, 55(2):417–433, 2010. doi:10.1088/0031-9155/55/2/006.

[88] F. Fiorini, D. Kirby, J. Thompson, S. Green, D. J. Parker, B. Jones, and M. A. Hill. Under-response correction for EBT3 films in the presence of proton spread out Bragg peaks. *Phys. Medica*, 30(4):454–461, 2014. doi:10.1016/j.ejmp.2013.12.006.

[89] R. Castriconi, M. Ciocca, A. Mirandola, C. Sini, S. Broggi, M. Schwarz, F. Fracchiolla, M. Martišíková, G. Aricò, G. Mettivier, and P. Russo. Doseresponse of EBT3 radiochromic films to proton and carbon ion clinical beams. *Phys Med Biol.*, 62(2):377–393, 2017. doi:10.1088/1361-6560/aa5078.

[90] O. S. Pianykh. *Digital Imaging and Communications in Medicine (DICOM)*. Springer Berlin Heidelberg, 2nd edition, 2012. doi:10.1007/978-3-540-74571-6.

[91] E. Bär, A. Lalonde, R. Zhang, K. W. Jee, K. Yang, G. Sharp, B. Liu, G. Royle, H. Bouchard, and H. M. Lu. Experimental validation of two dual-energy CT methods for proton therapy using heterogeneous tissue samples. *Med. Phys.*, 45(1):48–59, 2018. doi:10.1002/mp.12666.

[92] N. Arbor, D. Dauvergne, G. Dedes, J. M. Létang, K. Parodi, C. T. Quiñones, E. Testa, and S. Rit. Monte Carlo comparison of x-ray and proton CT for range calculations of proton therapy beams. *Phys Med Biol.*, 60(19):7585, 2015. doi:10.1088/0031-9155/60/19/7585.

[93] V. Bashkirov, R. Johnson, H. Sadrozinski, and R. Schulte. Development of proton computed tomography for applications in hadron therapy. *Nucl. Instrum. Meth. Phys. Res. Sect. A Accel. Spectrometers, Detect. Assoc. Equip.*, 809:120–129, 2016. doi:10.1063/1.3120073.